Constraints on short-range modified gravity with self-gravitating Bose-Einstein condensates

Dissertation

submitted to the
Combined Faculty of Physics and Electrical Engineering
of the University of Bremen, Germany

for the degree of
Doctor of Natural Sciences (Dr. rer. nat.)

By
Dipl.-Phys. Sandro Gödtel
born in Kaiserslautern

conducted at:
Center of Applied Space Technology and Microgravity (ZARM), University of Bremen

1. referee: Prof. Dr. Claus Lämmerzahl
2. referee: PD Dr. Axel Pelster

submitted: 6th April 2023
date of the colloqium: 14th July 2023

July 2023

Abstract

A central topic of modern research is the question of how to unify quantum mechanics and gravitational theory. Numerous theories introduce additional dimensions or exotic particles that result in a modification of Newton's law of gravity at small distances. Mostly these modifications are parametrized in the form of a Yukawa potential. Also from the experimental side innumerable tests were accomplished in the past decades in order to track down deviations to the Newtonian theory. This has covered distances of over thirty orders of magnitude from experiments in particle accelerators to observations on astronomical scales. The results so far show no deviations from Newton's law of universal gravitation and thus provide clear constraints on the parameters of the Yukawa potential.

In this thesis, we introduce a novel theoretical concept to test these constraints. Our model differs from previous tests, which mostly refer to external gravitational fields. We consider a quantum mechanical many-particle system, a so-called self-gravitating Bose-Einstein condensate, in which the individual particles interact additionally via a gravitational potential. To ensure experimental testability, we study collective frequencies of such a condensate, which are known to depend on the intrinsic interaction.

Using a variational method, we analytically determine step by step the contributions to the collective frequencies due to the contact interaction, a Newtonian and a Yukawa-like interaction. Furthermore, we also consider spherical and axially symmetric condensates, where the latter can be realized in cigar-shaped or disk-shaped form. Finally, we discuss hypothetical rational, logarithmic, and exponential modifications, which exhibit different types of singularities, thus testing our method presented here.

Zusammenfassung

Ein zentrales Thema moderner Forschung ist die Frage, wie man Quantenmechanik und Gravitationstheorie vereinheitlichen kann. Zahlreiche Theorien führen zusätzliche Dimensionen oder exotische Teilchen ein, die bei geringen Distanzen eine Modifikation des Newtonschen Gravitationsgesetzes zur Folge haben. Meist werden diese Modifikationen in Form eines Yukawa-Potentials parametrisiert. Auch von experimenteller Seite wurden in den vergangenen Jahrzehnten unzählige Tests durchgeführt, um Abweichungen zur Newtonschen Theorie aufzuspüren. Dabei wurden von Experimenten in Teilchenbeschleuniger bis zu Beobachtungen auf astronomischen Skalen Distanzen von über dreißig Größenordnungen abgedeckt. Die Ergebnisse zeigen bislang keine Abweichungen von dem Newtonschen Gravitationsgesetz und liefern damit deutliche Einschränkungen für die Parameter des Yukawa-Potentials.

In dieser Arbeit stellen wir ein neuartiges theoretisches Konzept vor, um diese Einschränkungen zu testen. Unser Modell unterscheidet sich von bisherigen Tests, die sich meist auf externe Gravitationsfelder beziehen. Wir betrachten ein quantenmechanisches Vielteilchensystem, ein sogenanntes selbst gravitierendes Bose-Einstein Kondensat, in welchem die einzelnen Teilchen zusätzlich über ein Gravitationspotential miteinander wechselwirken. Um eine experimentelle Überprüfbarkeit zu gewährleisten, untersuchen wir kollektive Frequenzen eines solchen Kondensates, die bekanntlich von der intrinsischen Wechselwirkung abhängen.

Über eine Variationsmethode bestimmen wir analytisch Schritt für Schritt die Beiträge zu den kollektiven Frequenzen aufgrund der Kontaktwechselwirkung, einer Newtonschen sowie einer Yukawa-Wechselwirkung. Weiterhin betrachten wir auch sphärische und axialsymmetrische Kondensate, wobei letztere in Zigarren- oder Scheibenform realisiert werden können. Zum Schluss diskutieren wir noch rationale, logarithmische und exponentielle Modifikationen, die unterschiedliche Arten von Singularitäten aufweisen, und testen damit unsere hier vorgestellte Methode.

Contents

1. Introduction

1.1. Bose-Einstein condensates

In 1924, Bose showed that the thermal distribution of photons follows a Planck distribution [1]. This idea was carried on by Einstein in 1925 and extended the work to non-interacting massive bosonic particles [2], marking the prediction of a new state of matter. This state will then become known as the Bose-Einstein condensate (BEC).

Seven decades later, and with the aid of numerous advancements in cooling and trapping technologies [3, 4, 5], the first condensates were experimentally realized in 1995. Within a few months three groups reported a success: Cornell and Wieman condensed a cloud of atomic ^{87}Rb [6], Ketterle realized a condensate of ^{23}Na [7] and Hulet of ^{7}Li [8, 9]. This breakthrough was honored by the Nobel Prize in 1997 for Chu, Cohen-Tannoudji and Phillips for the trapping methods and the Nobel Prize in 2001 for Cornell, Wieman and Ketterle for the first realization of Bose-Einstein condensates.

The method used in the laboratories consists of two key techniques: The first one is a magneto-optical trap in which the atoms are magnetically trapped by the Zeeman shift. Counter-propagating laser beams in all three spatial directions then provide a cooling temperature of 10 μK by spontaneous emission. The second technique is called evaporative cooling. Here, the trap depth is reduced, allowing faster atoms to escape the condensate cloud. This consequently results in a lower average temperature for the remaining condensate. With this it is possible to cool ^{87}Rb down to 170 nK [6]. To verify the condensed state so-called time-of-flight measurements are performed. These are measurements of the velocity distribution after the trap is switched off and the condensate cloud has been expanded for a certain period. Fig. 1.1 shows the time-of-flight measurements of the first realized condensate. The left plot shows the velocity distribution of an atom cloud above the critical temperature of condensation, which resembles a Maxwell-Boltzmann distribution as expected for a classical ideal gas. In the

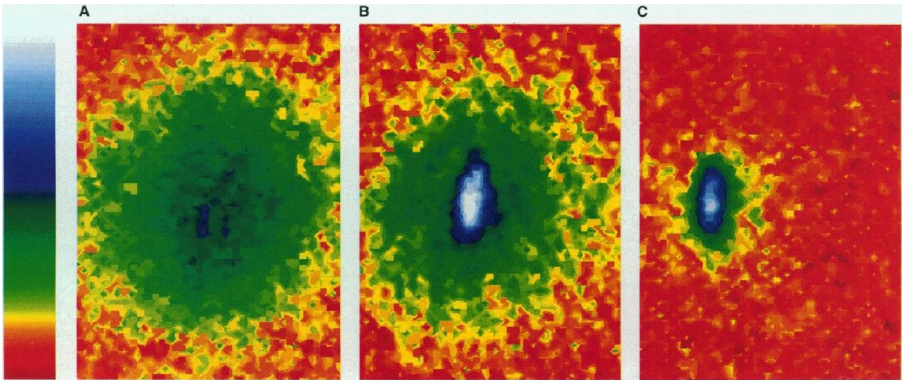

Figure 1.1.: Velocity distribution as a false color image taken from Ref. [6]: before the condensation (left), right after the moment of condensation (middle), and after further evaporation (right). The color indicates the number of atoms at a certain velocity ranging from fewest (red) to greatest (white) number. The white and blue fraction is a macroscopically occupied state representing the condensate. The green and yellow portion indicates a thermal cloud.

middle the critical temperature is reached and a small fraction of atoms is in a condensed state, while in the right plot below the critical temperature a large fraction of the cloud has zero velocity and occupies the ground state thus forming a BEC.

The experimental success led to the establishment and rapid growth of the field of ultracold atoms. Nowadays, the process of condensation is a well known routine and performed by hundreds of research groups around the world. Consequently, both experimental and theoretical advances are numerous. Besides the already mentioned condensates of ^{87}Rb, ^{23}Na and ^{7}Li, the list of created BECs ever expanded now including H [10], ^{4}He [11], ^{40}Ca [12], ^{41}K [13], ^{84}Sr [14, 15] but also heavier elements like ^{133}Cs [16] and ^{174}Yb [17], as well as isotopes of the aforementioned ones. Other elements with significantly different particle interactions, namely the strong dipole-dipole interaction, also have been successfully condensed, for example ^{52}Cr [18], the lanthanoids ^{164}Dy [19], ^{168}Er [20], ^{169}Tm [21] and quite recently in 2022 ^{151}Eu [22]. It is also possible to use dimers of fermionic atoms [23], molecules like a pair of two fermionic ^{6}Li [24]. Further, mixtures of two different bosonic atoms [25] as well as bosonic and fermionic atoms [26] have been studied.

In the last decade, more exotic and non-equilibrium condensates have become of particular interest, since the process of condensation also applies to photons [27] and quasiparticles such as phonons [28], magnons [29], excitons and polaritons [30] due to having

integer spins.

Some of the above mentioned condensates can only be achieved by the use of Feshbach resonances [31, 32]. These allow the interatomic interaction strength to be tuned by an external magnetic field. In combination with a very precise external laser potential, atomic systems are highly controllable and create a playground for both studies of fundamental physics and new applications. As a few examples, the creation of BECs in microgravity is used to improve the precision of atom interferometry, which led to the first creation of a condensate in space [33] and the world record of the coldest realized temperature of around 38 pK [34]. It is also part of two experiments at the Cold Atom Laboratory on the International Space Station [35]. Another important application is the simulation of quantum mechanical systems which are generally difficult to access. As an example, BECs in optical lattices [36, 37] mimic the behavior of electron pairs in solids [38] and supersonic condensates show an event horizon like in black-hole physics [39].

From a theoretical point of view, a bosonic gas forms a Bose-Einstein condensate when the temperature of its particles falls below a critical temperature [38, 40]. This critical point is derived with the thermal de-Broglie wavelength

$$\lambda_{\mathrm{dB}} = \hbar\sqrt{\frac{2\pi}{mk_{\mathrm{B}}T}}. \tag{1.1}$$

Once the de-Borglie wavelength coincides with the average distance between two particles the matter waves overlap and the condensation occurs. At a temperature of absolute zero all bosons occupy the same state and thus the Bose-Einstein condensate forms a giant matter wave, which makes the theoretical analysis significantly easier. Instead of a full many-body theory the system is described by one single wave function. Additionally, the particle interaction is described by a Lennard-Jones potential usually given by

$$V_{\mathrm{LJ}}(r) = 4\epsilon\left[\left(\frac{\sigma}{r}\right)^{12} - \left(\frac{\sigma}{r}\right)^{6}\right], \tag{1.2}$$

where ϵ denotes the depth of the potential well and σ is the distance, where the potential vanishes. The attractive part proportional to r^{-6} originates from the van der Waals interaction. In dilute gases, i.e. when the particle distance is greater than the scattering length, the Lennard-Jones potential is commonly approximated by a pseudopotential

known as the contact interaction

$$V_{\text{con}}(r - r') = g\ \delta(r - r'). \tag{1.3}$$

The single wave function and the pseudopotential are used in a mean-field approach leading to the Gross-Pitaevskii equation (GPE)

$$i\hbar\ \partial_t \Psi = -\frac{\hbar^2}{2m}\Delta\Psi + V_{\text{ext}}\Psi + g|\Psi|^2\Psi. \tag{1.4}$$

This is the central equation of ultracold atoms. It consists of a Schrödinger equation with an external potential V_{ext} and additionally includes a nonlinear interaction between the particles. Further, it accurately describes many static and dynamical properties of BECs such as superfluidity and the formation of vortices [40, 41]. However, the GPE is only valid for a temperature of 0 K, as the equation does not take into account any temperature dependence. Since the critical temperature for condensates of photons, excitons and magnons is of the order of the room temperature [27, 30, 29], the GPE is not applicable to these cases, because the coupling to the thermal cloud or bath is not negligible.

As a short remark, in addition to the contact interaction other potentials have also been considered. Dipolar BECs like ^{52}Cr interact via an anisotropic dipole-dipole interaction proportional to r^{-3} [18] and in Ref. [42] an experimental setup is proposed to mimic an effective r^{-1} Coulomb potential, see also the comment in Ref. [43]. Both potentials are long-range interactions in contrast to the local contact interaction.

For the purpose of this thesis, we mention here another interesting aspect of BECs. By modulating the external trapping potential, the bosonic particles in the condensed state can be excited in collective oscillations [45, 46], where examples are shown in Fig. 1.2. The theoretical predictions and the experimental results of the frequencies are in excellent agreement [47], and the frequencies can be measured with a relative precision of 10^{-3} [48, 49]. Furthermore, it turns out that some of these frequencies, in particular those we are interested in, are sensitive to the interatomic interaction. Consequently, the frequencies are used to study both type and strength of the interaction. A very important tool for this is the Feshbach resonance, as it allows to change the scattering length over seven orders of magnitude [50]. Even the sign of the interaction is accessible, which corresponds to attractive or repulsive interactions.

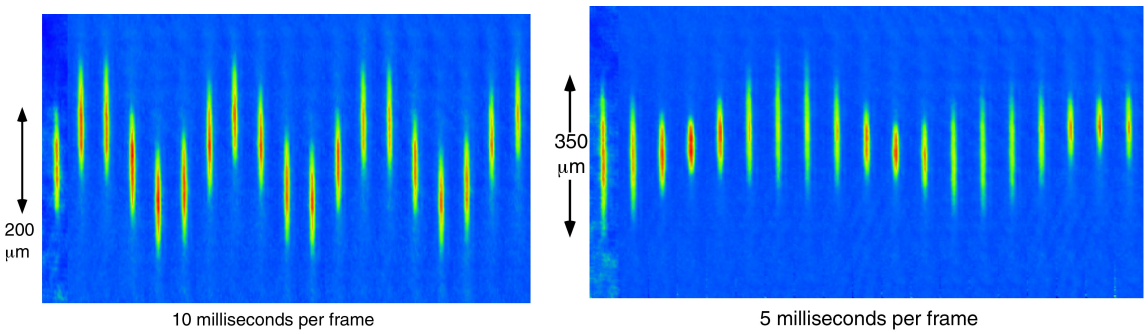

Figure 1.2.: Measurements of two collective modes taken from Ref. [44]. (Left) The dipole oscillation shows a back and forth movement of the entire cloud. (Right) In the quadrupole mode, the radial and axial widths oscillate out of phase visible by the color-coded density change.

1.2. Gravitational theory and its modifications

The basis of the gravitational theory is an inverse square law for the gravitational force between two masses at a certain distance proposed by Newton in the *Principia* [51]. It became later known as Newton's law of universal gravitation

$$F_{\mathrm{N}} = G\frac{Mm}{r^2} \tag{1.5}$$

or in form of a potential energy

$$V_{\mathrm{N}}(r) = -G\frac{Mm}{r}. \tag{1.6}$$

Despite being one of the oldest fundamental laws of modern physics it is also one of the least precisely known due to the relative uncertainty of the gravitational constant of around 10^{-5} [52]. However, for most practical uses in daily life the law is sufficient but fails to explain some observations like the exact perihelion shift or at strong gravitational fields. These problems were solved by General Relativity (GR), a theory approaching gravity very differently and opening a new perspective on how to think about space and time. In its theory, however, Newtonian physics can be derived as a limiting case. Experimental tests demonstrate precise agreement with the theoretically predicted perihelion shift of Mercury [53] and quite recently the existence of gravitational waves [54] and black holes [55].

Despite astonishing accuracy, there are still unsolved problems. Gravity does not

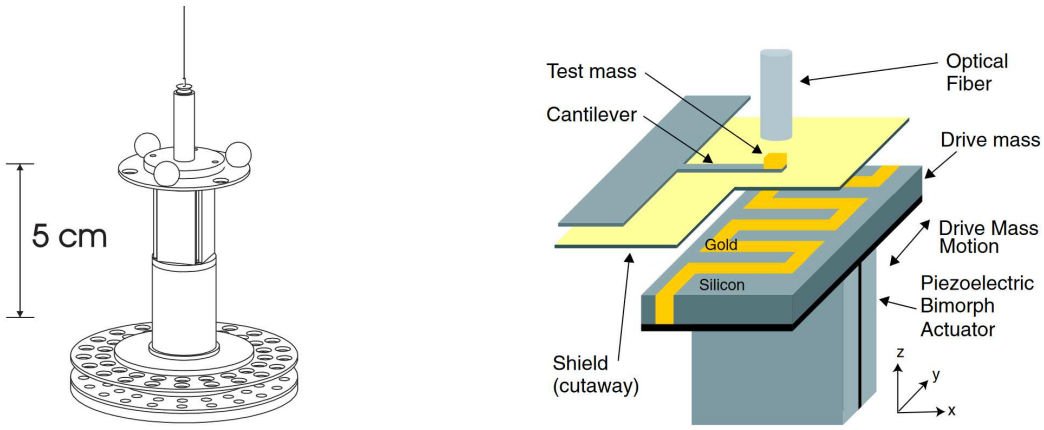

Figure 1.3.: Experimental setups to test non-Newtonian gravity: (left) a torsion balance experiment, picture taken from Ref. [67] and (right) a cantilever experiment described in Ref. [68].

fit into the Standard Model, which encompasses the other three fundamental forces of nature, namely electromagnetism, the weak and the strong force. Due to the lack of a quantum description of gravity and the relative weakness of gravity compared to the other forces, the so-called hierarchy problem, no grand unification was found so far [56].

As an important topic of current research many theories and experimental claims emerged in recent decades concerning gravity, especially at short ranges in the sub-millimeter regime. In 1971, Fujii considered a new dilaton field with a finite range of interaction, resulting in a slightly different potential than the Newtonian potential [57]. Other ideas include the gravitational constant to depend on the distance [58] or to be a composition of two different contributions by gravity and a fifth force [59, 60, 61, 62, 63]. Also the existence of extra dimensions were considered by Arkani-Hamed, Dimopoulos and Dvali in 1998 known as the ADD model [64, 65].

In many cases, the modifications to Newtonian gravity can be parametrized in form of a Yukawa-type potential [66]

$$V_{\mathrm{Yuk}} = -G\frac{Mm}{r}\left(1 + \alpha \exp\left\{-\frac{r}{\lambda}\right\}\right). \tag{1.7}$$

The effective range of the modification may be the Compton wavelength in case of exotic particles or the radius of the compactification of extra dimensions.

The amount of publications predicting deviations from Newtonian gravity lead to many experimental tests of the inverse-square law. Comprehensive collections can be

found i.e. in Refs. [66, 69, 70, 71]. The tests range from the subnanometer regime to astronomical scales. For the smallest length scales, data from proton-proton collisions have been collected and compared to the predictions of the Standard Model [72, 73, 74], while the constraints at larger lengths come from astronomical observations such as the secular motion of the perihelia of planets in the solar system [75]. In the millimeter regime deviations from the inverse-square law can be tested via torsion balance experiments, where a rotating attractor induces a varying torque due to an inhomogeneous mass distribution to a detector [76, 67]. Another setup consists of a cantilever holding a test mass above a moving alternating pattern of silicon and gold stripes to measure forces at an Attonewton magnitude induced by the different masses of the pattern at distances of 20 μm [68, 77], see Fig. 1.3. Also the Casimir effect can be used to obtain bounds to the Yukawa parameters [78, 79, 80].

So far no deviations to Newton's inverse square law were observed, thus the results are commonly given as exclusion plots for both Yukawa parameter as shown in Fig. 1.4. In order to improve the constraints on the Yukawa parameters or observe hints of non-Newtonian physics, it is still an ongoing topic in current research in both experimental and theoretical physics. In addition to the improvement of existing experiments, new ideas are also proposed, including a new interpretation of geodesy data [81], the existence of quark stars in relation to the gravitational-wave event GW170817 [82], neutron scattering [83] and neutron interferometry [84] as well as optomechanical quantum sensors [85] and the satellite mission MICROSCOPE [86].

1.3. Selfgravitating BECs

A combination of both research areas BECs and gravity are discussed mainly in an astrophysical context. Ruffini and Bonazzola introduced the concept of self-gravitating bosons which satisfy the relativistic Einstein-Klein-Gordon equation [87]. There, the bosons are trapped in their own gravitational potential, which is suggested to lead to a formation of hypothetical astrophysical objects known as boson stars [88]. Furthermore, self-gravitating bosons serve as dark matter candidates [89].

In 1996, Penrose proposed a self-gravitating quantum system described by the Schrödinger-Newton equation [90]. It was shown that this equation can be obtained as the nonrelativistic limit of the Einstein-Klein-Cordon equation [91, 92]. A many-particle

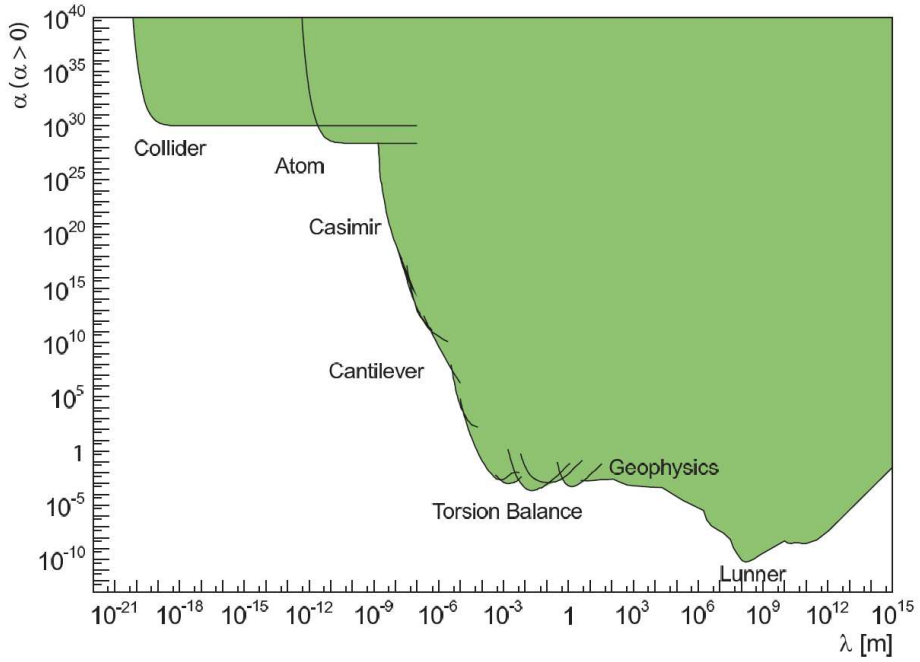

Figure 1.4.: Exclusion plot for the Yukawa parameters α and λ taken from Ref. [69]. The colored region is excluded with a confidence level of 95%.

equivalent is known as the Gross-Pitaevskii-Poisson or Gross-Pitaevskii-Newton (GPN) system [93]

$$i\hbar\,\partial_t\Psi = -\frac{\hbar^2}{2m}\Delta\Psi + V_{\text{ext}}\Psi + g|\Psi|^2\Psi + m\Phi\Psi, \tag{1.8a}$$

$$\Delta\Phi = 4\pi G|\Psi|^2, \tag{1.8b}$$

where G denotes the gravitational constant and Φ is an additional interaction potential which fulfills the Poisson equation (1.8b). It should be noted that the Schrödinger-Newton equation is not a limiting case of the GPN system, since in the GPN system the gravitational contribution originates from neighboring particles. The GPN system is used to model boson stars and was also applied to dipolar Bose-Einstein condensates [94] and ultracold plasma [95]. In the context of Bose-Einstein condensates it has been shown that there are stable solutions for such condensates [96], although in the Thomas-Fermi approximation the solutions become unstable due to a positive total energy [97]. For dark matter galactic halos in the form of self-gravitating condensates, see e.g. Ref. [89], numerical programs were developed to solve the GPN system via the Crank-Nicholson

method [98].

1.4. Outline of the thesis

In this thesis we aim to improve the constraints on the Yukawa parameters α and λ with the model of a non-relativistic self-gravitating Bose-Einstein condensate. The gravitational interaction is therefore assumed to be described by a Yukawa potential. We decided to focus on the calculation of the frequencies of low-lying collective modes, as these quantities are experimentally accessible.

In Chapter 2 we begin with an introduction to the variational method used to derive the collective frequencies. We follow the instructions given in Refs. [99, 100]. Further details can be found in Ref. [101]. In this chapter we restrict ourselves to a formulation of the method for an arbitrary two-particle interaction, which leads to general expressions.

These expressions are then specified in Ch. 3, where we assume a spherically symmetric condensate as the simplest case. After reviewing known results for the contact interaction, we add a Newtonian gravitational potential and determine how this affects the collective frequencies. Since the Newtonian potential is by its nature a long-range interaction and divergent at its origin, we have to move the problem from position space to the Fourier space. In the last part we replace the Newtonian potential with the Yukawa potential, which leads to a dependence of the collective frequencies on the Yukawa parameters. This allows us to create contour plots, which we then compare to the experimentally verified results shown in Fig 1.4.

Afterwards, we generalize our calculations to axial symmetry in Ch. 4. Firstly, this is closer to experimental setups generally used. Secondly, we hope to amplify the gravitational interaction by a dimensional reduction. Again, we derive the collective frequencies for condensates interacting via the common contact interaction, the Newtonian gravity and finally the Yukawa-like potential step by step.

As a further application of the method described in this thesis, we investigate the influence of other plausible modifications to the Newtonian potential in Chapter 5.

Finally, in Chapter 6 we summarize the results and conclude with an outlook on further perspectives.

Publications

Parts of this thesis have been published:

S. Gödtel, C. Lämmerzahl (2023). *Constraints on short-range gravity with self-gravitating Bose-Einstein condensates*, arXiv.2304.01310

2. Variational method and collective modes

In this chapter, we review some fundamental basics of Bose-Einstein condensation. As shown in the introduction Sec. 1.1, the central equation describing the physics of a Bose-Einstein condensed state is a partial differential equation called the Gross-Pitaevskii equation, see Eq. (1.4). We first discuss the limiting case of a non-interacting condensate and present some simple results. Following Refs. [99, 101], we introduce a variational approach to approximate solutions to the time-dependent GPE including small but non-vanishing interactions. This method is widely used to determine the equilibrium width as well as low-lying collective modes and frequencies of the condensate. For the variational method, we assume arbitrary two-particle interactions and give formal expressions that will be used later on. The type of the interaction and the symmetry of the system will then be specified in the following chapters.

2.1. Gross-Pitaevskii equation

We consider a Bose-Einstein condensate, which is commonly described by the three-dimensional GPE

$$i\hbar\,\partial_t\Psi = -\frac{\hbar^2}{2m}\Delta\Psi + V_{\text{ext}}\Psi + g|\Psi|^2\Psi, \tag{2.1}$$

where the wavefunction $\Psi := \Psi(\mathbf{x}, t)$ in general depends on spatial and temporal coordinates and is usually normalized with respect to the particle number N

$$\int \mathrm{d}x^3|\Psi|^2 = N. \tag{2.2}$$

The first term of the right-hand side of Eq. (2.1) describes the kinetic energy including

the mass m of the atomic species and the second term contains an external trap potential V_{ext}, which is often chosen to be a harmonic potential

$$V_{\text{ext}}(\mathbf{r}) = \frac{m}{2}(\omega_x^2 x^2 + \omega_y^2 y^2 + \omega_z^2 z^2) \tag{2.3}$$

with the respective trap frequencies ω_j in each spatial direction. The last part of Eq. (2.1) is of nonlinear nature and describes the contact interaction between two particles, where $g = 4\pi\hbar^2 a_{\text{s}}/m$ is the interaction strength with a_{s} denoting the s-wave scattering length. Interactions between three or more particles as well as higher order scattering terms are neglected in most cases due to the dilute nature of the gas. More details can be found in the literature, e.g. Refs. [38, 102].

Due to the nonlinear character, the GPE (2.1) is generally not solvable with an exact analytic term. However, in the following we discuss the case of a non-interacting condensate, which is exactly solvable for a harmonic potential. For this, we simply neglect the interaction term by setting $g = 0$. As a consequence, the nonlinearity in the GPE (2.1) vanishes and the equation thus reduces to an ordinary Schrödinger equation

$$i\hbar\, \partial_t \Psi = -\frac{\hbar^2}{2m}\Delta\Psi + V_{\text{ext}}\Psi. \tag{2.4}$$

Assuming the harmonic trap given by Eq. (2.3) the wave function is then simply given as a Gaussian function

$$\Psi_{\text{Gauss}} = \frac{\sqrt{N}}{\sqrt[4]{\pi^3}\sqrt{l_x l_y l_z}} \exp\left\{-\left(\frac{x^2}{2l_x^2} + \frac{y^2}{2l_y^2} + \frac{z^2}{2l_z^2}\right)\right\}, \tag{2.5}$$

where we define the oscillator lengths $l_j = \sqrt{\hbar/(m\omega_j)}$, respectively. This wave function fulfills the normalization condition (2.2).

2.2. Variational ansatz

For the purpose of this work, we have to find a way to include weak interactions, as we expect this to be the case for gravitational interactions at smaller scales. A widely known method to do so is the variational approach, which is based on the results of the non-interacting case discussed in the previous section. It is clear that including a small interaction between the particles will influence the shape of the condensate.

Depending on the sign of the interaction strength g or alternatively the sign of the s-wave scattering length a_s, the interaction is attractive or repulsive, leading to a contraction or an extension of the BEC cloud. In order to derive the equilibrium width of the cloud as well as the frequencies of the low-lying excitations, we follow a publication by Pérez-Garcia *et al.* [99]. As mentioned in the beginning of this chapter we assume an arbitrary two-particle interaction.

We start by defining the action

$$\mathcal{A}[\Psi^\star, \Psi] = \int \mathrm{d}t \int \mathrm{d}^3x \; \mathcal{L}[\Psi^\star, \Psi, \nabla\Psi^\star, \nabla\Psi, \partial_t\Psi^\star, \partial_t\Psi], \tag{2.6}$$

where the Lagrange density $\mathcal{L}$ is given by

$$\begin{aligned}\mathcal{L} = {} & i\hbar\Psi^\star(\mathbf{x},t)\partial_t\Psi(\mathbf{x},t) - \frac{\hbar^2}{2m}\nabla\Psi^\star(\mathbf{x},t)\nabla\Psi(\mathbf{x},t) \\ & - V_\mathrm{ext}(\mathbf{x})|\Psi(\mathbf{x},t)|^2 - \frac{1}{2}|\Psi(\mathbf{x},t)|^2 \int \mathrm{d}^3x' \; V_\mathrm{int}(\mathbf{x},\mathbf{x}')|\Psi(\mathbf{x}',t)|^2\end{aligned} \tag{2.7}$$

and the wave function $\Psi = \Psi(\mathbf{x},t)$ depends on spatial and temporal coordinates. Following Hamilton's principle $\delta\mathcal{A} = 0$, we have to extremize the action with respect to the variational parameters. In our case, these are the wave function Ψ and its complex conjugate $\Psi^\star$. This leads to the Euler-Lagrange equations

$$\frac{\delta\mathcal{A}}{\delta\Psi(\mathbf{x},t)} = \frac{\partial\mathcal{L}}{\partial\Psi(\mathbf{x},t)} - \nabla\frac{\partial\mathcal{L}}{\partial\nabla\Psi(\mathbf{x},t)} - \frac{\partial}{\partial t}\frac{\partial\mathcal{L}}{\partial\dot{\Psi}(\mathbf{x},t)} = 0, \tag{2.8}$$

$$\frac{\delta\mathcal{A}}{\delta\Psi^\star(\mathbf{x},t)} = \frac{\partial\mathcal{L}}{\partial\Psi^\star(\mathbf{x},t)} - \nabla\frac{\partial\mathcal{L}}{\partial\nabla\Psi^\star(\mathbf{x},t)} - \frac{\partial}{\partial t}\frac{\partial\mathcal{L}}{\partial\dot{\Psi}^\star(\mathbf{x},t)} = 0, \tag{2.9}$$

which represent a set of two differential equations for Ψ and $\Psi^\star$, namely the time-dependent GPE for both the wave function and its complex conjugate describing the system.

It is convenient to assume a harmonic oscillator potential as given by Eq. (2.3). For the wave function, we extend the Gauß solution of the non-interacting case (2.5) to a generalized Gauß ansatz, see Ref. [99]

$$\Psi(\mathbf{x},t) = \alpha(t)\prod_{j=1}^{3}\exp\left\{-\frac{(x_j - x_{0j}(t))^2}{2A_j^2(t)} + ix_jv_j(t) + ix_j^2B_j(t)\right\}. \tag{2.10}$$

Here we introduced as parameters the amplitude $\alpha(t)$, the center $x_{0j}(t)$, and the width $A_j(t)$ of the wave function. Furthermore, we have $v_j(t)$, the velocity at which the center moves, and $B_j(t)$, describing the expansion or contraction velocity of an oscillation around the center.

The general ansatz (2.10) is widely used to derive various oscillation modes of the condensate. In addition to the low-lying collective modes that we are mainly focusing on in this work, there is also a very special mode called the Kohn mode. This mode was originally investigated in terms of the cyclotron resonance of an interacting electron gas [103] but was further extended to a harmonically trapped gas [104, 105]. For condensates this mode is interpreted as the oscillation of the center of mass within the trapping potential. It turns out that the corresponding frequency is identical to the trap frequency. Additionally, it was shown that the frequency of the Kohn mode is independent of the particle interaction and unaffected by the temperature [38]. As a consequence, this mode is of particular interest in the experiment, as one can reliably determine the trap frequency. However, there are also predictions that the Kohn theorem breaks down in the vicinity of a Feshbach resonance [106] and for dissipative systems [107].

In this thesis we restrict ourselves to a cloud at the center of the trap, hence $x_{j0}(t) = 0$. Furthermore, we set the velocity $v_j(t)$ to zero, as we do not want the condensate to move inside the trap as a whole. With that, we simplify the general expression in Eq. (2.10), thus we choose in the following the ansatz for the wave function as

$$\Psi_{\text{ansatz}}(\mathbf{x}, t) = \frac{\sqrt{N}}{\sqrt[4]{\pi^3}\sqrt{A_1(t)A_2(t)A_3(t)}} \exp\left\{-\sum_{j=1}^{3}\left(\frac{1}{2A_j(t)^2} + iB_j(t)\right)x_j^2\right\}. \tag{2.11}$$

This function serves as a test function in the approximation method. The amplitude can be derived explicitly by the normalization condition (2.2), which leads to the prefactor given in Eq. (2.11). The parameters $A_j(t)$ describe the widths of the Gaussian, while the $B_j(t)$ correspond to the expansion or contraction velocities of the wave function. Later on we will see that the $B_j(t)$ are essential for the correct dynamical behavior. In the following, both sets of parameters $A_j(t)$ and $B_j(t)$ will be the variational variables.

Inserting our ansatz (2.11) into the action (2.6), we can rewrite the spatial integral of the Lagrange density as Lagrange function. The action now depends on the parameters

$A_j(t)$ and $B_j(t)$ and their temporal derivatives, thus

$$\mathcal{A} = \int \mathrm{d}t \; L\big(A(t), \partial_t A(t), B(t), \partial_t B(t)\big). \tag{2.12}$$

According to the Lagrange density (2.7), the Lagrange function consists of four individual parts

$$L = L_{\mathrm{time}} + L_{\mathrm{kin}} + L_{\mathrm{pot}} + L_{\mathrm{int}}, \tag{2.13}$$

which we calculate separately now. For better readability, we omit the time dependence in the notation of A_i and B_i.

The first contribution includes the temporal derivative

$$L_{\mathrm{time}} = i\hbar \int \mathrm{d}^3x \; \Psi^\star \partial_t \Psi. \tag{2.14}$$

We insert the Gaussian ansatz and calculate the derivatives

$$L_{\mathrm{time}} = i\hbar \frac{N}{\sqrt{\pi}} \sum_{j=1}^{3} \left[\frac{1}{A_j} \int_{-\infty}^{\infty} \mathrm{d}x_j \; \left(-\frac{\dot{A}_j}{2A_j} + \frac{\dot{A}_j}{A_j^3} x_j^2 - i\dot{B}_j x_j^2 \right) \exp\left\{ -\frac{x_j^2}{A_j^2} \right\} \right]. \tag{2.15}$$

With the two Gauss integrals, see Ref. [108]

$$\int_{-\infty}^{\infty} \mathrm{d}x_j \; \exp\left\{ -\frac{x_j^2}{A_j^2} \right\} = \sqrt{\pi} A_j, \tag{2.16}$$

$$\int_{-\infty}^{\infty} \mathrm{d}x_j \; x_j^2 \exp\left\{ -\frac{x_j^2}{A_j^2} \right\} = \frac{\sqrt{\pi}}{2} A_j^3, \tag{2.17}$$

we then obtain an expression, where both terms including the first temporal derivative with respect to A_j cancel each other. The result is the first contribution of the Lagrangian in (2.13)

$$L_{\mathrm{time}} = \frac{\hbar}{2} N \sum_{j=1}^{3} A_j^2 \dot{B}_j. \tag{2.18}$$

The second term corresponds to the kinetic part of the Lagrange function

$$L_{\text{kin}} = -\frac{\hbar^2}{2m}\int \mathrm{d}^3x\ \nabla\Psi^\star\nabla\Psi. \tag{2.19}$$

It is treated in the same way as the first term. We insert the Gauss ansatz and calculate the derivatives

$$L_{\text{kin}} = -\frac{\hbar^2}{2m}\frac{N}{\sqrt{\pi}}\sum_{j=1}^{3}\frac{1}{A_j}\left(\frac{1}{A_j^4}+4B_j^2\right)\int_{-\infty}^{\infty}\mathrm{d}x_j\ x_j^2\exp\left\{-\frac{x_j^2}{A_j^2}\right\}. \tag{2.20}$$

After that we integrate and obtain

$$L_{\text{kin}} = -\frac{\hbar^2}{m}N\sum_{j=1}^{3}\left(\frac{1}{4A_j^2}+A_j^2B_j^2\right). \tag{2.21}$$

The third term is the potential term given by

$$L_{\text{pot}} = -\int \mathrm{d}^3x\ V_{\text{ext}}(\mathbf{x})|\Psi|^2. \tag{2.22}$$

We can easily calculate this term using the harmonic potential (2.3), thus

$$L_{\text{pot}} = -\frac{m}{2}\frac{N}{\sqrt{\pi}}\sum_{j=1}^{3}\frac{1}{A_j}\omega_j^2\int_{-\infty}^{\infty}\mathrm{d}x_j\ x_j^2\exp\left\{-\frac{x_j^2}{A_j^2}\right\}. \tag{2.23}$$

Now we integrate to get

$$L_{\text{pot}} = -\frac{m}{4}N\sum_{j=1}^{3}\omega_j^2A_j^2. \tag{2.24}$$

With the contributions (2.18), (2.21), and (2.24) the Lagrange function now reads

$$L = \sum_{j=1}^{3}\left[\frac{\hbar}{2}NA_j^2\dot{B}_j - \frac{\hbar^2}{m}N\left(\frac{1}{4A_j^2}+A_j^2B_j^2\right) - \frac{m}{4}N\omega_j^2A_j^2\right] + L_{\text{int}}. \tag{2.25}$$

Note that the contribution of the two-particle interaction L_{int} is given in general by

$$L_{\text{int}} = -\frac{1}{2}\int \mathrm{d}^3x \int \mathrm{d}^3x' \; |\Psi(\mathbf{x},t)|^2 V_{\text{int}}(\mathbf{x}-\mathbf{x}')|\Psi(\mathbf{x}',t)|^2. \tag{2.26}$$

When we insert the Gauss ansatz (2.11), we obtain

$$L_{\text{int}} = -\frac{1}{2}\frac{N^2}{\pi^3}\frac{1}{A_1^2A_2^2A_3^2}\int \mathrm{d}^3x \int \mathrm{d}^3x' \; V_{\text{int}}(\mathbf{x}-\mathbf{x}') \exp\left\{-\sum_{j=1}^{3}\frac{x_j^2 - x_j'^2}{A_j^2}\right\}. \tag{2.27}$$

This expression now depends only on the parameters A_j, but not on the parameters B_j, because the imaginary argument of the exponential cancels out when calculating the absolute square, so $L_{\text{int}} = L_{\text{int}}(A_x, A_y, A_z)$.

As mentioned above, we extremize now the action $\mathcal{A}$ with respect to the variational parameters $A_j(t)$ and $B_j(t)$, which can be written in form of the Euler-Lagrange equations

$$\frac{\delta\mathcal{A}}{\delta A_j(t)} = \frac{\partial L}{\partial A_j(t)} - \frac{d}{dt}\frac{\partial L}{\partial \dot{A}_j(t)} = 0, \tag{2.28}$$

$$\frac{\delta\mathcal{A}}{\delta B_j(t)} = \frac{\partial L}{\partial B_j(t)} - \frac{d}{dt}\frac{\partial L}{\partial \dot{B}_j(t)} = 0. \tag{2.29}$$

With the Lagrangian (2.25) the first equation yields

$$-\hbar A_j\dot{B}_j + 2\frac{\hbar^2}{m}A_jB_j^2 + \frac{m}{2}\omega_j^2A_j = \frac{\hbar^2}{2m}\frac{1}{A_j^3} + \frac{1}{N}\partial_{A_j}L_{\text{int}}. \tag{2.30}$$

Extremizing with respect to $B_j(t)$ leads to the expression

$$B_j = -\frac{m}{2\hbar}\frac{\dot{A}_j}{A_j}. \tag{2.31}$$

This we insert into (2.30) and use the product rule for $\dot{B}_j$ such that the first order time derivatives cancel each other. The remaining expression is then simplified to the following set of ordinary differential equations (ODE) of second order

$$\ddot{A}_j + \omega_j^2A_j = \frac{\hbar^2}{m^2}\frac{1}{A_j^3} + \frac{1}{N}\frac{2}{m}\partial_{A_j}L_{\text{int}}(A_x, A_y, A_z), \tag{2.32}$$

describing the change of the cloud width $A_j(t)$ over the time t. Note that if we choose $B_j(t) = 0$ at the beginning of our ansatz (2.11), the resulting equations (2.30) no longer depend on time. By this, we receive a stationary solution. As a consequence, in order to analyze the dynamical behavior of a condensate, it is essential to assume $B(t) \neq 0$.

Now we want to write down the equations in a more compact way. For this purpose, we introduce dimensionless variables

$$\nu_j = \frac{\omega_j}{\omega} \ , \quad \tau = \omega t \ , \quad \gamma_j = \sqrt{\frac{m\omega}{\hbar}} A_j, \tag{2.33}$$

where the parameter ω can be defined by the geometric mean of the frequencies ω_j to fix a frequency scale. This transformation leads to a set of dimensionless differential equations

$$\ddot{\gamma}_j = -\nu_j^2 \gamma_j + \frac{1}{\gamma_j^3} + \frac{1}{N} \frac{2}{\hbar\omega} \partial_{\gamma_j} L_{\text{int}} \left(\sqrt{\frac{\hbar}{m\omega}} \gamma_x, \sqrt{\frac{\hbar}{m\omega}} \gamma_y, \sqrt{\frac{\hbar}{m\omega}} \gamma_z \right). \tag{2.34}$$

The first term on the right-hand side is the contribution of the external trap, while the second part is derived from the kinetic energy. Due to the sign difference they have opposite effects: the potential ensures a contraction of the cloud width, while the kinetic energy provides a widening. The last part represents a contribution by the two-particle interaction.

2.3. Equilibrium cloud width and collective modes

In the last section we solved the time-dependent GPE with a variational ansatz. As a result we received a set of time-dependent ODEs (2.34), which describe a harmonic oscillation of the condensate cloud with a dispersive part due to the kinetic energy of a single particle and an attractive part because of the trapping potential. Now, in this section we further investigate the equations. We are mainly interested in two results: the first being the equilibrium width around which the cloud oscillates and the second being the modes and the frequencies of these oscillations.

The equilibrium cloud width γ_{j0} is determined by setting $\ddot{\gamma}_j = 0$ in Eq. (2.34), so

$$-\nu_j^2\gamma_{j0} + \frac{1}{\gamma_{j0}^3} + \frac{1}{N}\frac{2}{\hbar\omega}\partial_{\gamma_j}L_{\text{int}}\left(\sqrt{\frac{\hbar}{m\omega}}\gamma_{x0}, \sqrt{\frac{\hbar}{m\omega}}\gamma_{y0}, \sqrt{\frac{\hbar}{m\omega}}\gamma_{z0}\right) = 0. \tag{2.35}$$

To analyze now the dynamics of the system we rewrite the equation of motion (2.34) as a motion of a point particle in an effective potential

$$\ddot{\gamma}_j = -\partial_{\gamma_j}V_{\text{eff}}(\gamma_x, \gamma_y, \gamma_z), \tag{2.36}$$

where the effective potential is given by

$$V_{\text{eff}}(\gamma_x, \gamma_y, \gamma_z) = \sum_j\left(\frac{\nu_j^2}{2}\gamma_j^2 + \frac{1}{2\gamma_j^2}\right) - \frac{1}{N}\frac{2}{\hbar\omega}L_{\text{int}}\left(\sqrt{\frac{\hbar}{m\omega}}\gamma_x, \sqrt{\frac{\hbar}{m\omega}}\gamma_y, \sqrt{\frac{\hbar}{m\omega}}\gamma_z\right). \tag{2.37}$$

This can easily be verified by evaluating the derivative of that potential to retrieve Eq. (2.34).

Next, for the oscillation we assume a small perturbation around the equilibrium such that $\gamma_j(\tau) = \gamma_{j0}(\tau) + \delta\gamma_j(\tau)$. For better readability we omit the time dependence in the following. Inserting the perturbation into the effective potential (2.37) and performing a Taylor expansion for small perturbations $\delta\gamma_j$ up to second order leads to

$$\begin{aligned} V_{\text{eff}}(\gamma_{x0} + \delta\gamma_x, &\gamma_{y0} + \delta\gamma_y, \gamma_{z0} + \delta\gamma_z) = \\ &V_{\text{eff}}(\gamma_{x0}, \gamma_{y0}, \gamma_{z0}) + \nabla V_{\text{eff}}(\gamma_{x0}, \gamma_{y0}, \gamma_{z0}) \cdot \boldsymbol{\delta\gamma} + \frac{1}{2}\boldsymbol{\delta\gamma}^{\mathrm{T}} M \boldsymbol{\delta\gamma} \end{aligned} \tag{2.38}$$

with the vector $\boldsymbol{\delta\gamma} = (\delta\gamma_x, \delta\gamma_y, \delta\gamma_z)$. The gradient of the effective potential at the equilibrium point $\nabla V_{\text{eff}}(\gamma_{x0}, \gamma_{y0}, \gamma_{z0})$ is per construction by Eq. (2.36) and the condition $\ddot{\gamma}_j = 0$ for the steady state equal to zero. As a consequence, in Eq. (2.38) the linear part in the perturbation $\boldsymbol{\delta\gamma}$ simply vanishes. The matrix M is given by the Hessian matrix of the effective potential at the equilibrium

$$M = \left(\partial_{\gamma_j}\partial_{\gamma_k}V_{\text{eff}}(\gamma_x, \gamma_y, \gamma_z)\big|_{\gamma=\gamma_0}\right)_{j,k}. \tag{2.39}$$

It can be written as the sum

$$M = M_1 + M_{\text{int}}, \tag{2.40}$$

where with the explicit effective potential in Eq. (2.37)

$$M_1 = \begin{pmatrix} \nu_x^2 + \frac{3}{\gamma_{x0}^4} & 0 & 0 \\ 0 & \nu_y^2 + \frac{3}{\gamma_{y0}^4} & 0 \\ 0 & 0 & \nu_z^2 + \frac{3}{\gamma_{z0}^4} \end{pmatrix} \tag{2.41}$$

represents the single particle contribution including the kinetic as well as potential part and formally

$$M_{\text{int}} = -\frac{1}{N}\frac{2}{\hbar\omega}\left(\partial_{\gamma_j}\partial_{\gamma_k} L_{\text{int}}\left(\sqrt{\frac{\hbar}{m\omega}}\gamma_x, \sqrt{\frac{\hbar}{m\omega}}\gamma_y, \sqrt{\frac{\hbar}{m\omega}}\gamma_z\right)\Big|_{\boldsymbol{\gamma}=\boldsymbol{\gamma}_0}\right)_{j,k}, \tag{2.42}$$

which consists of the two-particle interaction and is in general responsible for diagonal as well as off-diagonal entries in the Hessian M.

The resulting equation

$$V_{\text{eff}}(\gamma_{x0} + \delta\gamma_x, \gamma_{y0} + \delta\gamma_y, \gamma_{z0} + \delta\gamma_z) = V_{\text{eff}}(\gamma_{x0}, \gamma_{y0}, \gamma_{z0}) + \frac{1}{2}\boldsymbol{\delta\gamma}^{\mathrm{T}} M \boldsymbol{\delta\gamma} \tag{2.43}$$

describes a coupled oscillation around the equilibrium width γ_{j0} with the associated amplitude $\delta\gamma_j$. The oscillation modes and their frequencies are determined by the eigenvectors and eigenvalues of the Hessian matrix M given in Eq. (2.40). However, for an explicit evaluation we have to specify the type of the two-particle interaction. This will be done in the following chapters.

3. Collective modes in spherical condensates

After the general introduction to the variational method in the previous chapter, we specify now the type of the two-particle interaction and investigate the low-lying collective oscillations with the general expressions given in Sec. 2.3. We begin this chapter with the commonly used contact interaction and derive already known results, see Refs. [99, 101]. In the second part we consider the long-range Newtonian potential as a new type of interaction between two particles. Since the real gravitational interaction is expected to be negligible due to the small masses of the atoms, such an interaction is usually discussed in terms of artificial potentials, see Refs. [42, 43]. As mentioned in the introduction in Sec. 1.1, an experimental setup to induce an effective r^{-1} interaction with a significantly larger interaction strength is proposed in Ref. [42]. Nevertheless, we present here the detailed calculations and results for a real gravitational interaction as a preparation to the last part of this chapter. There we look into the most prominent example of modified Newtonian interaction, i.e. a Yukawa-like interaction, which introduces two additional parameters: the interaction strength α and the effective range λ. In particular, α can be chosen in such a way that it compensates the relative weakness of the Newtonian interaction compared to the contact interaction. Consequently, this would lead to measurable gravitational effects, as we demonstrate in this chapter. For simplicity, throughout this chapter we will assume a spherically symmetric condensate. The more complicated case of axial symmetry will be discussed in Ch. 4.

3.1. Contact interaction

First of all, we start with the contact interaction and reproduce already known results, as given e.g. in Ref. [99, 101]. In the previous chapter we already derived general

expressions for the differential equations of motion Eq. (2.34), for the equilibrium cloud width γ_{j0} in Eq. (2.35) and for the Hessian matrix given by Eqs. (2.40), (2.41) and (2.42). In these equations we have used the Lagrangian for the two-particle interaction L_{int}, formally defined in Eq. (2.26) as a placeholder. In the following, we apply the potential energy for the contact interaction

$$V_{\text{con}}(\mathbf{x} - \mathbf{x}') = g\delta(\mathbf{x} - \mathbf{x}') \tag{3.1}$$

to explicitly determine the equilibrium cloud width γ_{j0} and the Hessian matrix M.

3.1.1. Lagrangian of the contact interaction

Due to the δ-function in the contact interaction (3.1) we obtain from the definition of the Lagrangian (2.26) describing the contribution of the interaction

$$L_{\text{con}} = -\frac{g}{2}\int \mathrm{d}^3x\ |\Psi|^4. \tag{3.2}$$

Note that we have to add a factor 1/2 here to avoid a double counting of the interaction terms as the particles are identical. For distinguishable particles this factor does not occur. Now inserting the Gauss ansatz for the wave function (2.11) and solving the Gaussian integrals results in

$$L_{\text{con}}(A_x, A_y, A_z) = -\frac{gN^2}{2\sqrt{(2\pi)^3}}\frac{1}{A_x A_y A_z}. \tag{3.3}$$

With the dimensionless Gauss width defined in (2.33), it reads

$$L_{\text{con}}\left(\sqrt{\frac{\hbar}{m\omega}}\gamma_x, \sqrt{\frac{\hbar}{m\omega}}\gamma_y, \sqrt{\frac{\hbar}{m\omega}}\gamma_z\right) = -\frac{gN^2}{2\sqrt{(2\pi)^3}}\left(\sqrt{\frac{m\omega}{\hbar}}\right)^3\frac{1}{\gamma_x\gamma_y\gamma_z}. \tag{3.4}$$

This Lagrangian is valid in any symmetry due to the local nature of the contact interaction.

3.1.2. Equilibrium and collective frequencies

With the Lagrangian of the contact interaction (3.4) we now derive the corrections to both the differential equations and the Hessian matrix due to the contact interaction.

In the ODE (2.34) the interaction term with the Lagrangian (3.4) is

$$\frac{2}{N\hbar\omega}\partial_{\gamma_j} L_{\mathrm{con}} = \frac{P}{\gamma_x\gamma_y\gamma_z}\frac{1}{\gamma_j}, \tag{3.5}$$

with the definition of the dimensionless contact interaction strength

$$P = \frac{gN}{\sqrt{(2\pi)^3}}\frac{m}{\hbar^2}\sqrt{\frac{m\omega}{\hbar}} = \sqrt{\frac{2}{\pi}}N\frac{a_{\mathrm{s}}}{l}. \tag{3.6}$$

In the last step we used the relation $g = 4\pi\hbar^2 a_{\mathrm{s}}/m$ and introduce the oscillator length $l = \sqrt{\hbar/(m\omega)}$ to shorten the expression. This leads us to an ODE for the dimensionless cloud width γ_j

$$\ddot{\gamma}_j = -\nu_j^2\gamma_j + \frac{1}{\gamma_j^3} + \frac{P}{\gamma_x\gamma_y\gamma_z}\frac{1}{\gamma_j}. \tag{3.7}$$

The contribution of the particle interaction in the last part depends on the sign of the s-wave scattering length a_{s}. In most cases, the scattering length is positive, resulting in another dispersive part in addition to the kinetic contribution.

The equilibrium width γ_{j0} is again defined by setting $\ddot{\gamma}_j = 0$ in Eq. (3.7), thus

$$-\nu_j^2\gamma_{j0} + \frac{1}{\gamma_{j0}^3} + \frac{P}{\gamma_{x0}\gamma_{y0}\gamma_{z0}}\frac{1}{\gamma_{j0}} = 0. \tag{3.8}$$

This is a set of algebraic equations where the last term represents a coupling of the three equations introduced by the two-particle interaction.

For the Hessian matrix M we need to determine the elements $M_{\mathrm{con}}^{(jk)}$ (2.42), which are proportional to the second derivative of L_{con} (3.4). This leads to the diagonal and

off-diagonal entries

$$M_{\mathrm{con}}^{(jj)} = \frac{P}{\gamma_{x0}\gamma_{y0}\gamma_{z0}} \frac{2}{\gamma_{j0}^2}, \tag{3.9a}$$

$$M_{\mathrm{con}}^{(jk)} = \frac{P}{\gamma_{x0}\gamma_{y0}\gamma_{z0}} \frac{1}{\gamma_{j0}\gamma_{k0}} \tag{3.9b}$$

with $j \neq k$.

Finally, the Hessian for the contact interaction in general reads

$$M = \begin{pmatrix} \nu_x^2 + \frac{3}{\gamma_{x0}^4} + \frac{2P}{\gamma_{x0}^3\gamma_{y0}\gamma_{z0}} & \frac{P}{\gamma_{x0}^2\gamma_{y0}^2\gamma_{z0}} & \frac{P}{\gamma_{x0}^2\gamma_{y0}\gamma_{z0}^2} \\ \frac{P}{\gamma_{x0}^2\gamma_{y0}^2\gamma_{z0}} & \nu_y^2 + \frac{3}{\gamma_{y0}^4} + \frac{2P}{\gamma_{x0}\gamma_{y0}^3\gamma_{z0}} & \frac{P}{\gamma_{x0}\gamma_{y0}^2\gamma_{z0}^2} \\ \frac{P}{\gamma_{x0}^2\gamma_{y0}\gamma_{z0}^2} & \frac{P}{\gamma_{x0}\gamma_{y0}^2\gamma_{z0}^2} & \nu_z^2 + \frac{3}{\gamma_{z0}^4} + \frac{2P}{\gamma_{x0}\gamma_{y0}\gamma_{z0}^3} \end{pmatrix}. \tag{3.10}$$

So far we have not assumed any symmetry of our system. Thus, the results are valid in general for the contact interaction. Nevertheless, we dedicate this chapter to spherically symmetric condensates, so we briefly mention this special case. The symmetry can be realized by assuming

$$\nu_x = \nu_y = \nu_z = \nu, \quad \gamma_{x0} = \gamma_{y0} = \gamma_{z0} = \gamma_0. \tag{3.11}$$

Hence, the important equations simplify, i.e. for the equilibrium width we have to solve only one equation

$$-\nu^2\gamma_0 + \frac{1}{\gamma_0^3} + \frac{P}{\gamma_0^4} = 0, \tag{3.12}$$

and for the collective frequencies we have to calculate the eigenvalues of the matrix

$$M = \begin{pmatrix} \nu^2 + \frac{3}{\gamma_0^4} + \frac{2P}{\gamma_0^5} & \frac{P}{\gamma_0^5} & \frac{P}{\gamma_0^5} \\ \frac{P}{\gamma_0^5} & \nu^2 + \frac{3}{\gamma_0^4} + \frac{2P}{\gamma_0^5} & \frac{P}{\gamma_0^5} \\ \frac{P}{\gamma_0^5} & \frac{P}{\gamma_0^5} & \nu^2 + \frac{3}{\gamma_0^4} + \frac{2P}{\gamma_0^5} \end{pmatrix}. \tag{3.13}$$

The first eigenvalue leads to the collective frequency

$$\frac{\Omega_{\mathrm{br}}^{(\mathrm{con})}}{\omega} = \sqrt{\nu^2 + \frac{3}{\gamma_0^4} + \frac{4P}{\gamma_0^5}}. \tag{3.14}$$

Its corresponding eigenvector describes a radial oscillation, which is therefore also called breathing mode.

In addition, we get one degenerate collective frequency

$$\frac{\Omega_{\mathrm{qu}}^{(\mathrm{con})}}{\omega} = \sqrt{\nu^2 + \frac{3}{\gamma_0^4} + \frac{P}{\gamma_0^5}}, \tag{3.15}$$

associated to two quadrupole modes. In the next section we discuss these results in detail.

3.1.3. Discussion

Here, we show the results for the equilibrium cloud width and the collective frequencies for the simple case of a spherical condensate with a contact interaction between two particles.

First, we have to find the equilibrium cloud width. For this we evaluate Eq. (3.12). Without loss of generality, we set $\nu = 1$ and rewrite the equation as

$$\gamma_0^5 - \gamma_0 - P = 0 \tag{3.16}$$

In that form, we now search numerically for the roots of the function on the left hand-side. From a mathematical point of view since the function being of fifth order, there exists in total five roots in the complex plane. However, from a physical perspective we are only interested in real positive solutions, as it should depict a positive width of the condensate. In fact, using Descartes' rule of sign [109], we can show that only one such real positive root exists for the function on the left hand-side in Eq. (3.16). For this rule we simply have to check the sign changes of the coefficients of a polynomial. For $P > 0$, implying a repulsive contact interaction, we have only one change of sign, hence there exist only one positive root.

Assuming $P < 0$ leads to two sign changes such that according to Descartes' sign rule we can have two positive real solutions or none. In fact, we can interpret Eq. (3.16) as a function $P(\gamma)$ with $P(\gamma) = \gamma^5 - \gamma$. Searching for the minimum of this function leads to $P_{\mathrm{min}} = -0.535$. For $P < P_{\mathrm{min}}$ we have no solution for the equilibrium cloud width, thus the cloud is instable for large attractive contact interaction. If $P_{\mathrm{min}} < P < 0$ there exists a stable and an unstable solution. More details can be found in [100].

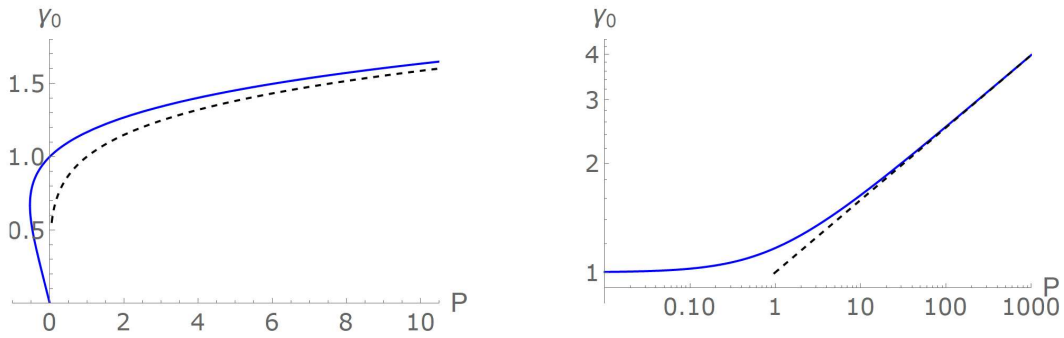

Figure 3.1.: Equilibrium cloud width γ_0 depending on the contact interaction strength P for a spherical BEC. The figure on the right hand-side scales double-logarithmically. The black dashed line represents the Thomas-Fermi limit given in Eq. (3.17).

In Fig. 3.1 we show the equilibrium width γ_0 depending on the interaction strength P. The width increases with larger interaction strength. As expected, for higher interaction strengths P, the repulsion between the particles in the condensate is greater, thus the cloud is expanded. For the purpose of this work, we are only interested in a repulsive contact interaction, meaning we only allow positive values for P for the rest of this thesis.

In the second part, we are interested in the collective frequencies given by the equations (3.14) and (3.15). Again $\nu = 1$ and for each value of P we have to insert the corresponding cloud width γ_0 determined in the previous calculation.

The results are shown in Fig. 3.2. Both frequencies are identical for $P = 0$ and for larger interaction strength the frequencies split into two branches. The collective frequency of the breathing mode is slightly increased, while the frequency corresponding to the quadrupole modes drastically decreases. Approaching higher values of P, the curves for both frequencies asymptotically converge towards a corresponding constant. This regime of strong interaction is known as the Thomas-Fermi limit. According to [38], if the interaction is strong enough, we can neglect the kinetic part in Eq. (3.16), which is linear in γ_0. As a result, we simply get

$$\gamma_0^5 = P. \tag{3.17}$$

We now apply the same approximation of neglecting the kinetic part for the collective

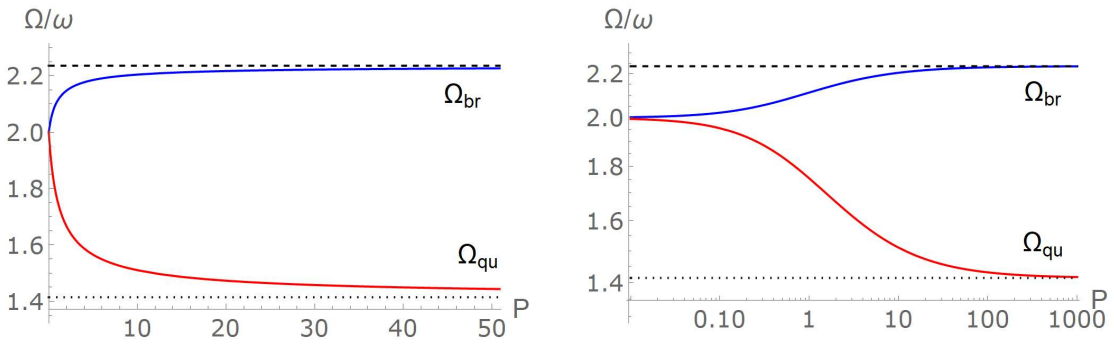

Figure 3.2.: Collective frequencies $\Omega_{\mathrm{br}}/\omega$ and $\Omega_{\mathrm{qu}}/\omega$ depending on the contact interaction strength P for a spherical BEC. The figure on the right hand-side scales double-logarithmically. The black dashed and black dotted lines represent the Thomas-Fermi limits for each frequency.

frequencies given by Eqs. (3.14) and (3.15). So in the Thomas-Fermi limit the frequencies are given by

$$\frac{\Omega_{\mathrm{con}}^{(\mathrm{br})}}{\omega} = \sqrt{1+\frac{4P}{\gamma_0^5}}, \quad \frac{\Omega_{\mathrm{con}}^{(\mathrm{qu})}}{\omega} = \sqrt{1+\frac{P}{\gamma_0^5}}, \tag{3.18}$$

which simplifies with the equilibrium cloud width of Eq. (3.17) to $\Omega_{\mathrm{con}}^{(\mathrm{br})}/\omega = \sqrt{5} \approx 2.236$ and $\Omega_{\mathrm{con}}^{(\mathrm{qu})}/\omega = \sqrt{2} \approx 1.414$. This result coincides with the asymptotic behaviours in Fig. 3.2 as well as the literature [110].

In the end of this section we give a typical experimental value for the contact interaction strength P. As an example, for the commonly used ^{87}Rb, the atomic mass m and the s-wave scattering length a_{s} are given by

$$m = 87 \cdot 1.66 \cdot 10^{-27}\ \mathrm{kg}, \tag{3.19a}$$

$$a_{\mathrm{s}} = 90 a_0 \tag{3.19b}$$

with the Bohr radius a_0.

The value for the s-wave scattering length a_{s} is taken from Ref. [38]. Furthermore, for a realistic experiment, we assume the external trap frequency ω and the particle number

N to be

$$\omega = 1 \text{ kHz}, \tag{3.20a}$$

$$N = 10^5. \tag{3.20b}$$

Note that we are using the angular frequency ω, which in an experiment is related to the frequency ν by $\omega = 2\pi\nu$. Inserting these values into the definition of the interaction strength P given in Eq. (3.6) leads to $P \approx 446$, which is clearly in the Thomas-Fermi regime, as shown in Fig. 3.2. With this, we calculate the equilibrium cloud width $\gamma_0 \approx 3.39$ and the collective frequencies $\Omega_{\text{br}}^{(\text{con})}/\omega \approx 2.234$ and $\Omega_{\text{qu}}^{(\text{con})}/\omega \approx 1.420$, which are very close to the Thomas-Fermi limit mentioned previously. In physical units using Eq. (2.33) we then obtain $A_0 \approx 2.89\ \mu$m, $\Omega_{\text{br}}^{(\text{con})} \approx 2.234$ kHz, and $\Omega_{\text{qu}}^{(\text{con})} \approx 1.420$ kHz as the typical values for our example.

3.2. Newtonian interaction

Now it is time to take a look into a gravitational interaction. In order to analyze the influence of an attractive Newtonian two-particle interaction, we follow the steps of the previous section. However, instead of using a contact interaction potential given in (3.1), we insert the Newtonian potential (1.6) into the Lagrangian of the interaction (2.26). Therefore, in general we have

$$L_{\text{N}} = \frac{1}{2} \int \mathrm{d}^3 r \int \mathrm{d}^3 r' \ |\Psi(\mathbf{r}, t)|^2 \frac{u}{|\mathbf{r} - \mathbf{r}'|} |\Psi(\mathbf{r}', t)|^2, \tag{3.21}$$

where we use the short notation $u = Gm^2$ with G as the gravitational constant. Furthermore, we assume a condensate of a single atomic species, thus the masses are equal. Thus u is always positive. Note that we again have to include a factor $1/2$ as the particles are indistinguishable.

The integral in Eq. (3.21) diverges due to the singularity of the Newtonian potential (1.6) at $|\mathbf{r} - \mathbf{r}'| \to 0$. More precisely, it is a UV divergence, since the potential diverges at shorter distances. One possibility to handle this problem is using the Schwinger parametrization from quantum field theory to rewrite all spatial integrals into Gaussian integrals. This was already done in a diploma thesis [111] and we show the detailed calculation in the Appendix A.

Despite this approach, a mathematically more convenient one will be used here as well. To do this, we transform the spatial integrals in the Lagrangian (3.21) into the Fourier space and solve the integrals there. This technique was used by Muruganandam *et al.* to reduce the dipolar interaction to lower dimensions in Ref. [112]. Inspired by this publication, we present in the following the evaluation of the Lagrangian (3.21) with a Newtonian interaction potential for a spherically symmetric condensate.

3.2.1. Lagrangian in Fourier space

Starting point of the calculation is the energy contribution

$$L_{\mathrm{N}} = -\frac{1}{2}\int \mathrm{d}^3r \int \mathrm{d}^3r'\; n(\mathbf{r})\; V_{\mathrm{N}}(\mathbf{r}-\mathbf{r}')\; n(\mathbf{r}') \tag{3.22}$$

with the density $n(\mathbf{r}) = |\Psi(\mathbf{r})|^2$. A Fourier transformation of each component, e.g.

$$n(\mathbf{r}) = \frac{1}{(2\pi)^3}\int \mathrm{d}^3k\; \tilde{n}(\mathbf{k})\mathrm{e}^{i\mathbf{k}\cdot\mathbf{r}} \tag{3.23}$$

gives an expression with the integrals over r, r', k, k', and k''. Further details are given in the Appendix B.1. Rearranging and solving the integrals over both position spaces leads to two delta distributions in the remaining momentum coordinates. This then results in

$$L_{\mathrm{N}} = -\frac{1}{2}\frac{1}{(2\pi)^3}\int \mathrm{d}^3k\; \tilde{n}(\mathbf{k})\; \tilde{V}_{\mathrm{N}}(\mathbf{k})\; \tilde{n}(-\mathbf{k}). \tag{3.24}$$

To evaluate this integral we need the Fourier transform of both the density $\tilde{n}(\mathbf{k})$ and the Newtonian potential $\tilde{V}_{\mathrm{N}}(\mathbf{k})$.

In order to determine the Fourier transform of the density $\tilde{n}(\mathbf{k})$, we use the Gauss ansatz (2.11) of the previous chapter with different widths A_x, A_y, and A_z as the wave function. The density as the absolute square of the wave function is then given by

$$n(\mathbf{r}) = |\Psi|^2 = \frac{N}{\sqrt{\pi^3}A_xA_yA_z}\exp\left\{-\left(\frac{x^2}{A_x^2}+\frac{y^2}{A_y^2}+\frac{z^2}{A_z^2}\right)\right\}. \tag{3.25}$$

The parameters B_j used in the ansatz (2.11) vanish in the density due to the complex conjugation. This is true for all density-density interactions. Now we derive the Fourier

transform of the density. By definition according to (3.23) we have

$$\tilde{n}(\mathbf{k}) = \int \mathrm{d}^3 r \; n(\mathbf{r}) \mathrm{e}^{-i\mathbf{k}\cdot\mathbf{r}}. \tag{3.26}$$

Inserting the ansatz and solving each integral separately, results in

$$\tilde{n}(\mathbf{k}) = N \exp\left\{-\frac{1}{4}(A_x^2 k_x^2 + A_y^2 k_y^2 + A_z^2 k_z^2)\right\}. \tag{3.27}$$

Next, we derive the Fourier transform of the gravitational potential (1.6). Starting with the definition of the Fourier transformation

$$\tilde{V}_{\mathrm{N}}(\mathbf{k}) = -u \int \mathrm{d}^3 r \; \frac{1}{r} \mathrm{e}^{-i\mathbf{k}\cdot\mathbf{r}}, \tag{3.28}$$

we use spherical coordinates and immediately evaluate the integral over the angle φ

$$\tilde{V}_{\mathrm{N}}(\mathbf{k}) = -2\pi u \int_0^\infty \mathrm{d}r \int_0^\pi \mathrm{d}\vartheta \; r^2 \sin\vartheta \; \frac{1}{r} \exp\{-ikr\cos\vartheta\}, \tag{3.29}$$

where $k^2 = k_x^2 + k_y^2 + k_z^2$. Next, we use the substitution $v = \cos\vartheta$, $dv = -\sin\vartheta d\vartheta$ such that

$$\tilde{V}_{\mathrm{N}}(\mathbf{k}) = -2\pi u \int_0^\infty \mathrm{d}r \int_{-1}^1 \mathrm{d}v \; r^2 \frac{1}{r} \exp\{-ikrv\}. \tag{3.30}$$

For the integration over r, we have to add a factor $\mathrm{e}^{-\mu r}$ which guarantees the convergence of the integral accompanied by the limit $\mu \to 0^+$

$$\tilde{V}_{\mathrm{N}}(\mathbf{k}) = -2\pi u \lim_{\mu\to 0^+} \int_0^\infty \mathrm{d}r \; r \; \frac{2\sin(kr)}{kr} \mathrm{e}^{-\mu r}, \tag{3.31}$$

which then gives

$$\tilde{V}_{\mathrm{N}}(\mathbf{k}) = -4\pi u \lim_{\mu\to 0^+} \frac{1}{k^2 + \mu^2}. \tag{3.32}$$

The final result is obtained by taking the limit $\mu \to 0^+$

$$\tilde{V}_{\mathrm{N}}(\mathbf{k}) = -u \frac{4\pi}{k^2}. \tag{3.33}$$

Finally, we insert the Fourier transforms of the density (3.27) and of the potential (3.33) into the Lagrangian given by Eq. (3.24), which leads to the expression

$$L_{\mathrm{N}} = \frac{uN^2}{(2\pi)^2} \int \mathrm{d}^3k \, \frac{1}{k^2} \exp\left\{-\frac{1}{2}(A_x^2 k_x^2 + A_y^2 k_y^2 + A_z^2 k_z^2)\right\}. \tag{3.34}$$

For convenience, we use the dimensionless units given in (2.33) and additionally we define a dimensionless momentum by

$$k = \sqrt{\frac{m\omega}{\hbar}}\kappa. \tag{3.35}$$

With this we obtain the Lagrangian

$$L_{\mathrm{N}} = \frac{uN^2}{(2\pi)^2}\sqrt{\frac{m\omega}{\hbar}} \int \mathrm{d}^3\kappa \, \frac{1}{\kappa^2} \exp\left\{-\frac{1}{2}(\gamma_x^2\kappa_x^2 + \gamma_y^2\kappa_y^2 + \gamma_z^2\kappa_z^2)\right\}, \tag{3.36}$$

where $\kappa^2 = \kappa_x^2 + \kappa_y^2 + \kappa_z^2$. Since we are interested in the ODE (2.34), the equilibrium cloud width γ_{j0} in Eq. (2.35), and the interaction part of the Hessian matrix given by Eq. (2.42), it is sufficient to evaluate the first and second derivatives $\partial_{\gamma_j} L_{\mathrm{N}}$ and $\partial_{\gamma_j}\partial_{\gamma_k} L_{\mathrm{N}}$, which we address in the following section for the simplest case of spherical symmetry.

3.2.2. Equilibrium and collective frequencies

As a short-hand notation, we define the integral in (3.36) as

$$I_{\mathrm{N}} = \int \mathrm{d}^3\kappa \, \frac{1}{\kappa^2} \exp\left\{-\frac{1}{2}(\gamma_x^2\kappa_x^2 + \gamma_y^2\kappa_y^2 + \gamma_z^2\kappa_z^2)\right\}. \tag{3.37}$$

According to the ODE (2.34) we have to determine the first derivative of the integral I_{N} with respect to the dimensionless Gauss width γ_j. Here, we interchange the order of the integral over κ_j and the derivative with respect to γ_j as both are independent of each other. Now we perform the derivative of the exponential function first, thus

$$\partial_{\gamma_j} I_{\mathrm{N}} = -\gamma_j \int \mathrm{d}^3\kappa \, \frac{\kappa_j^2}{\kappa^2} \exp\left\{-\frac{1}{2}(\gamma_x^2\kappa_x^2 + \gamma_y^2\kappa_y^2 + \gamma_z^2\kappa_z^2)\right\}. \tag{3.38}$$

We follow the same procedure for the second derivatives of I_{N}, which will later on be used to determine the Hessian matrix via Eq. (2.42). This yields for the diagonal and

off-diagonal elements

$$\partial_{\gamma_j}^2 I_{\mathrm{N}} = \int \mathrm{d}^3\kappa \; \frac{\gamma_j^2\kappa_j^4 - \kappa_j^2}{\kappa^2} \exp\left\{-\frac{1}{2}(\gamma_x^2\kappa_x^2 + \gamma_y^2\kappa_y^2 + \gamma_z^2\kappa_z^2)\right\}, \tag{3.39a}$$

$$\partial_{\gamma_j}\partial_{\gamma_k} I_{\mathrm{N}} = \gamma_j\gamma_k \int \mathrm{d}^3\kappa \; \frac{\kappa_j^2\kappa_k^2}{\kappa^2} \exp\left\{-\frac{1}{2}(\gamma_x^2\kappa_x^2 + \gamma_y^2\kappa_y^2 + \gamma_z^2\kappa_z^2)\right\} \tag{3.39b}$$

for $j \neq k$. According to the Taylor expansion (2.38), the second derivatives have to be evaluated at the equilibrium width $\boldsymbol{\gamma}_0$.

So far, these expressions are generally valid, but to explicitly solve the integrals we have to specify the symmetry of the system. As mentioned at the beginning in this chapter, we focus on spherically symmetric condensates. We assume the Gauss widths γ_j to be equal, analogue to Eq. (3.11), and insert this into (3.38). Using spherical coordinates for the integration, we define the right-hand side of (3.38) as the function

$$J_{\mathrm{N}} = -\gamma \int_0^\infty \mathrm{d}\kappa \int_0^{2\pi} \mathrm{d}\varphi \int_0^\pi \mathrm{d}\vartheta \; \kappa^2 \sin\vartheta \; \frac{1}{\kappa^2} \; \kappa_j^2 \exp\left\{-\frac{1}{2}\gamma^2\kappa^2\right\}. \tag{3.40}$$

According to spherical coordinates, the κ_j are given by

$$\kappa_x = \kappa\cos\varphi \; \sin\vartheta, \quad \kappa_y = \kappa\sin\varphi \; \sin\vartheta, \quad \kappa_z = \kappa\cos\vartheta. \tag{3.41}$$

The integrals are derived in detail in the Appendix B.2. For the angular parts, this results in

$$\int_0^{2\pi} \mathrm{d}\varphi \int_0^\pi \mathrm{d}\vartheta \; \sin\vartheta \; \kappa_j^2 = \frac{4\pi}{3}\kappa^2 \tag{3.42}$$

for all j. The remaining radial integral

$$J_{\mathrm{N}} = -\gamma\frac{4\pi}{3} \int_0^\infty \mathrm{d}\kappa \; \kappa^2 \exp\left\{-\frac{1}{2}\gamma^2\kappa^2\right\} \tag{3.43}$$

is then solved by

$$J_{\mathrm{N}} = -\frac{4\pi}{3} \sqrt{\frac{\pi}{2}} \frac{1}{\gamma^2}. \tag{3.44}$$

Finally, with the prefactors in (3.36) the additional term in the ODE (2.34) becomes

$$\frac{1}{N}\frac{2}{\hbar\omega}\partial_{\gamma_j} L_{\mathrm{N}} = -\frac{Q}{\gamma^2} \tag{3.45}$$

where we define the gravitational interaction strength analogue to the contact interaction strength in (3.6) as

$$Q = \frac{1}{3}\sqrt{\frac{2}{\pi}}\frac{uN}{\hbar\omega}\sqrt{\frac{m\omega}{\hbar}} = \frac{1}{3}\sqrt{\frac{2}{\pi}}N\frac{a_{\mathrm{g}}}{l}. \tag{3.46}$$

Here we introduce a gravitational scattering length $a_{\mathrm{g}} = u/(\hbar\omega)$ similar to the s-wave scattering length a_{s}. As a reminder, we note that u was defined as $u = Gm^2$, meaning it is always positive. This corresponds then to the strength of the gravitational interaction, therefore $Q > 0$.

The differential equation (2.34) including the contact and Newtonian two-particle interaction is consequently

$$\ddot{\gamma} = -\nu^2\gamma + \frac{1}{\gamma^3} + \frac{P}{\gamma^4} - \frac{Q}{\gamma^2}. \tag{3.47}$$

Note that the additional gravitational part is always attractive like the trapping potential due to the sign of the interaction strength Q. Moreover, the additional gravitational contribution is proportional to γ^{-2} instead of γ^{-4} in case of the contact interaction.

We obtain the steady state again by setting $\ddot{\gamma} = 0$, hence

$$-\nu^2\gamma_0 + \frac{1}{\gamma_0^3} + \frac{P}{\gamma_0^4} - \frac{Q}{\gamma_0^2} = 0. \tag{3.48}$$

Next, we determine the entries in the Hessian matrix (2.42) for Newtonian interaction. To do this, we look again at the integrals in (3.39) with the assumption of spherical symmetry, i.e. the Gauss widths γ_j are equal. For the diagonal elements in spherical coordinates we define the right-hand side of (3.39a) as

$$J_{\mathrm{N}}^{(jj)} = \int_0^\infty \mathrm{d}\kappa \int_0^{2\pi} \mathrm{d}\varphi \int_0^\pi \mathrm{d}\vartheta\, \kappa^2 \sin\vartheta\, \frac{1}{\kappa^2}(\gamma^2\kappa_j^4 - \kappa_j^2) \exp\left\{-\frac{1}{2}\gamma^2\kappa^2\right\}. \tag{3.49}$$

With the κ_j given in Eq. (3.41) the angular parts result in

$$\int_0^{2\pi} \mathrm{d}\varphi \int_0^{\pi} \mathrm{d}\vartheta \, \sin\vartheta \, (\gamma^2\kappa_j^4 - \kappa_j^2) = 4\pi \left(\frac{\gamma^2}{5}\kappa^4 - \frac{1}{3}\kappa^2 \right) \tag{3.50}$$

for all j. Inserting (3.50) into (3.49) eventually leads to

$$J_{\mathrm{N}}^{(jj)} = \frac{16\pi}{15} \sqrt{\frac{\pi}{2}} \frac{1}{\gamma^3}. \tag{3.51}$$

See Appendix B.2 for further details. Evaluating $J_{\mathrm{N}}^{(jj)}$ at the equilibrium point $\gamma = \gamma_0$ results therefore in the diagonal elements

$$M_{\mathrm{N}}^{(jj)} = -\frac{4}{5}\frac{Q}{\gamma_0^3} \tag{3.52}$$

with the definition of Q in (3.46).

The off-diagonal elements (3.39b) are treated analogously. In spherical symmetry, we define

$$J_{\mathrm{N}}^{(jk)} = \gamma^2 \int_0^{\infty} \mathrm{d}\kappa \int_0^{2\pi} \mathrm{d}\varphi \int_0^{\pi} \mathrm{d}\vartheta \, \kappa^2 \sin\vartheta \, \frac{1}{\kappa^2}\kappa_j^2\kappa_k^2 \exp\left\{ -\frac{1}{2}\gamma^2\kappa^2 \right\}. \tag{3.53}$$

The angular integration shown in the Appendix B.2 is

$$\int_0^{2\pi} \mathrm{d}\varphi \int_0^{\pi} \mathrm{d}\vartheta \, \sin\vartheta \, \kappa_j^2\kappa_k^2 = \frac{4\pi}{15}\kappa^4 \tag{3.54}$$

for all j and k. This and the radial integral in Eq. (3.53) then gives

$$J_{\mathrm{N}}^{(jk)} = \frac{12\pi}{15}\sqrt{\frac{\pi}{2}}\frac{1}{\gamma^3}. \tag{3.55}$$

Once more, evaluating at the equilibrium point γ_0 leads to the off-diagonal elements

$$M_{\mathrm{N}}^{(jk)} = -\frac{3}{5}\frac{Q}{\gamma_0^3}. \tag{3.56}$$

Finally, the Hessian matrix including contact and Newtonian interaction in spherical

symmetry is

$$M = \begin{pmatrix} \nu^2 + \frac{3}{\gamma_0^4} + \frac{2P}{\gamma_0^5} - \frac{4}{5}\frac{Q}{\gamma_0^3} & \frac{P}{\gamma_0^5} - \frac{3}{5}\frac{Q}{\gamma_0^3} & \frac{P}{\gamma_0^5} - \frac{3}{5}\frac{Q}{\gamma_0^3} \\ \frac{P}{\gamma_0^5} - \frac{3}{5}\frac{Q}{\gamma_0^3} & \nu^2 + \frac{3}{\gamma_0^4} + \frac{2P}{\gamma_0^5} - \frac{4}{5}\frac{Q}{\gamma_0^3} & \frac{P}{\gamma_0^5} - \frac{3}{5}\frac{Q}{\gamma_0^3} \\ \frac{P}{\gamma_0^5} - \frac{3}{5}\frac{Q}{\gamma_0^3} & \frac{P}{\gamma_0^5} - \frac{3}{5}\frac{Q}{\gamma_0^3} & \nu^2 + \frac{3}{\gamma_0^4} + \frac{2P}{\gamma_0^5} - \frac{4}{5}\frac{Q}{\gamma_0^3} \end{pmatrix}. \tag{3.57}$$

Similar to Sec. 3.1, we find the breathing mode with the frequency

$$\frac{\Omega_{\mathrm{br}}^{(\mathrm{N})}}{\omega} = \sqrt{\nu^2 + \frac{3}{\gamma_0^4} + \frac{4P}{\gamma_0^5} - \frac{2Q}{\gamma_0^3}} \tag{3.58}$$

and two quadrupole modes each with the frequency

$$\frac{\Omega_{\mathrm{qu}}^{(\mathrm{N})}}{\omega} = \sqrt{\nu^2 + \frac{3}{\gamma_0^4} + \frac{P}{\gamma_0^5} - \frac{Q}{5\gamma_0^3}}. \tag{3.59}$$

In the next section we discuss these results.

3.2.3. Discussion

Analogous to Section 3.1.3, we investigate the behavior of the equilibrium cloud width and the collective frequencies now depending on the gravitational interaction strength Q. Setting $\nu = 1$, we rewrite the equation for the cloud width from Eq. (3.48) as

$$\gamma_0^5 - \gamma_0 - P + Q\gamma_0^2 = 0. \tag{3.60}$$

To apply Descartes' rule of sign, we rearrange the coefficients such that

$$\gamma_0^5 + Q\gamma_0^2 - \gamma_0 - P = 0. \tag{3.61}$$

Here we clearly see that we have only one sign change if $P > 0$, so once again we have exactly one guaranteed positive root.

In the case $P < 0$ we have two sign changes again, but in contrast to the previous section we now have two attractive components as well as the contact interaction and the gravitational interaction. The latter results in an instability of the condensate even for $|P| < |P_{\mathrm{min}}| = 0.535$ if the gravitational strength Q is large enough.

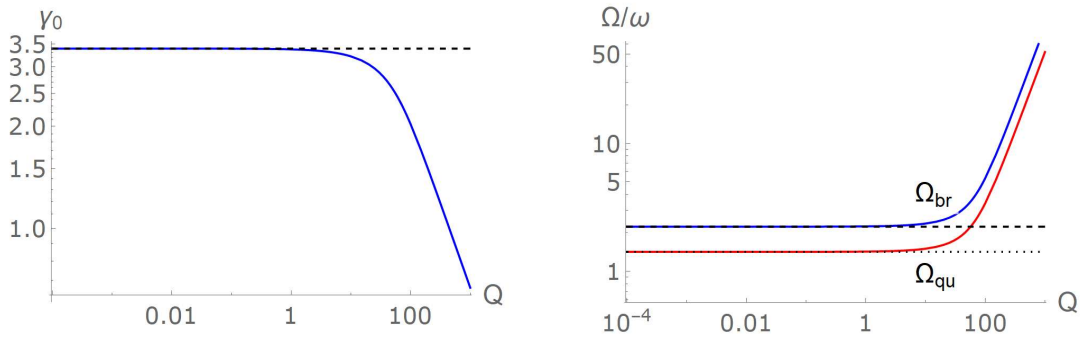

Figure 3.3.: Equilibrium cloud width γ_0 and collective frequencies $\Omega_{\mathrm{br}}/\omega$ and $\Omega_{\mathrm{qu}}/\omega$ depending on the gravitational interaction strength Q for a spherical BEC. In this example we choose $P = 446$. The black dashed and black dotted lines show the corresponding case without gravitational contribution, so $Q = 0$.

For a numerical evaluation we set the contact interaction strength to the realistic value for ^{87}Rb $P = 446$ as shown in the end of Section 3.1.3. We search again for the roots of the functions on the left hand-side of Eq. (3.60). This time, although, variable gravitational interaction strengths Q are considered. This leads to the equilibrium cloud width γ_0, which is then used to determine the collective frequencies given by Eqs. (3.58) and (3.59) with the fixed value for P and variable Q.

Fig. 3.3 shows the behavior of the equilibrium cloud width and the collective frequencies as a function of the gravitational interaction strength Q. For small values of Q, neither the cloud width nor the collective frequencies show any visible dependency. Eventually at $Q \sim 10$ the attractive interaction is strong enough to compete with the repulsive contact interaction, leading to a significant shrinkage of the cloud width. On the other side, the collective frequencies are increased for these large values of Q.

As a short remark, we mention here an analytical limit. For high values of Q, we are allowed to neglect the kinetic contribution as part of a Thomas-Fermi limit. If we now additionally set $P = 0$, Eq. (3.60) becomes

$$\gamma_0^3 + Q = 0, \tag{3.62}$$

which does not have a positive solution for the Gauss width γ. Here, we see in a very simplified case that a BEC with only an attractive interaction is not stable. Either a repulsive force, usually given by the contact interaction, is required to at least compen-

Table 3.1.: Comparison of s-wave scattering length a_s, contact interaction strength P, and gravitational interaction strength Q for some condensed atomic species. The values for the a_s are taken from Refs. [38, 113], the interactions strengths are calculated with Eqs. (3.6) and (3.46). We assume $N = 10^5$ particles and a trap frequency of $\omega = 1$ kHz.

	a_s [nm]	P	Q [10^{-20}]
^{7}Li	1.7	46	0.08
^{23}Na	1.0	49	1.5
^{41}Ka	4.5	289	6.3
^{87}Rb	4.7	446	41
^{133}Cs	14.8	1714	119
^{174}Yb	5.5	728	234

sate the attractive force, or there is no interaction, which corresponds to an ideal Bose gas.

In the end of this section, we give a realistic value for the gravitational interaction strength Q. It can be determined by inserting the typical experimental values from Eq. (3.19) and Eq. (3.20) into the definition (3.46), which leads to $Q = 4.1 \cdot 10^{-19}$. Compared to the contact interaction strength $P = 446$ derived in the previous section, the gravitational interaction strength is more than twenty orders of magnitude smaller. For the equilibrium cloud width and the collective frequencies including a Newtonian interaction we obtain

$$A_0 \approx 2.89\ \mu\text{m}, \quad \Omega_{\text{br}}^{(\text{N})} \approx 2.234\ \text{kHz}, \quad \Omega_{\text{qu}}^{(\text{N})} \approx 1.420\ \text{kHz} \tag{3.63}$$

in physical units, which are thus identical to the values in case of the contact interaction within the given accuracy, as seen in the previous section. This suggests that any changes in the equilibrium width and the collective frequency due to Newtonian gravity are far too small to be realistically measured in present laboratory.

In Tab. 3.1 we give a brief overview of the interaction strengths P and Q for some condensed atomic species. In comparison with Fig. 3.1 every listed value of P can be considered in the Thomas-Fermi regime. In regards of the gravitational interaction, Q is greater for heavier elements as expected.

3.3. Yukawa interaction

In the last part of the chapter we explore the effects of a Yukawa-like gravitational interaction potential on a condensate. As mentioned in the introduction of this thesis in Section 1.2, the Yukawa potential is a simple yet interesting model and nowadays still part of active research in the field of short-range gravity. Although the experiments so far have mainly dealt with the case of a test mass interacting with a classical external gravitation field, we will now focus on a purely intrinsic interaction within a quantum system. Analogue to the previous sections, we derive expressions for the equilibrium cloud width and the collective frequencies in the special case of a spherically symmetric BEC.

3.3.1. Lagrangian of the Yukawa interaction

To investigate the model for short-range gravity, we change the self-gravitating interaction potential by adding a Yukawa-like interaction given by (1.7) in addition to the prior used Newton potential. For simplicity we split the gravitational interaction into the sum of Newtonian and Yukawa-like gravity

$$V_{\mathrm{Yuk}}(\mathbf{r}) = -\frac{u}{r} - \alpha\frac{u}{r}\exp\left\{-\frac{r}{\lambda}\right\}. \tag{3.64}$$

The advantages of this potential are the following: First, we introduced two additional variables, the interaction strength α and the effective range λ. As shown in Fig. 3.4, the effective range guarantees us that for larger scales only the Newtonian part remains. On the other side, the parameter α can be used to significantly increase the gravitational effects on smaller length scales, despite the small interaction strength Q, as seen in Sec. 3.2.3.

For our method developed in this thesis, we are now interested in the Fourier transform of the Yukawa potential (3.64). The calculations are straightforward since we have already solved the integrals with the pure Newtonian potential in the previous section. The Fourier transformation of the potential (3.64) can also be split into two parts and the integrals are solved analogously to Eq. (3.33)

$$\tilde{V}_{\mathrm{Yuk}}(\mathbf{k}) = -u\frac{4\pi}{k^2} - \alpha u\frac{4\pi}{k^2 + \frac{1}{\lambda^2}}, \tag{3.65}$$

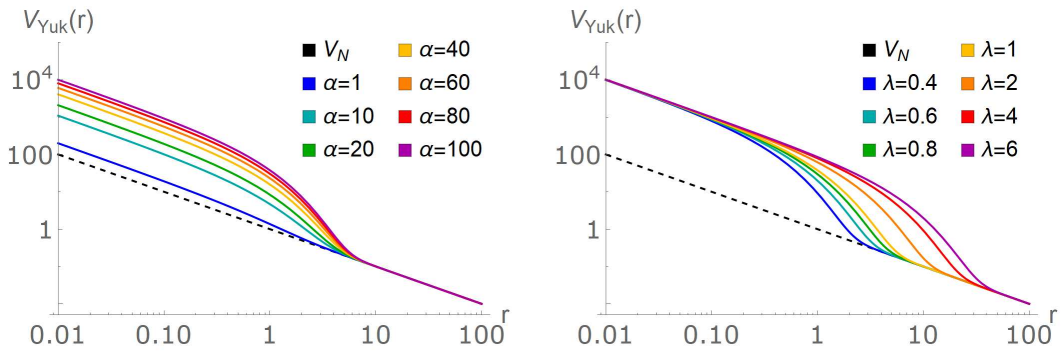

Figure 3.4.: Schematic sketch of the Yukawa potential $V_{\text{Yuk}}(r)$ for different values of α and λ. In the left plot we set $\lambda = 1$, while on the right plot we use $\alpha = 100$. The black dashed line indicates the Newtonian potential.

where the limit in the second integral is not required due to the finite effective range λ. Therefore, the second part of the expression still depends on both Yukawa parameters.

With the dimensionless units in (2.33) and (3.35) we formulate the Lagrangian in Fourier space analogous to (3.36) as

$$L_{\text{Yuk}} = \frac{uN^2}{(2\pi)^2}\sqrt{\frac{m\omega}{\hbar}}\int \mathrm{d}^3\kappa \left(\frac{1}{\kappa^2} + \frac{\alpha}{\kappa^2 + \bar{\lambda}^{-2}}\right) \exp\left\{-\frac{1}{2}(\gamma_x^2\kappa_x^2 + \gamma_y^2\kappa_y^2 + \gamma_z^2\kappa_z^2)\right\}, \quad (3.66)$$

where we introduced the dimensionless effective range

$$\bar{\lambda} = \sqrt{\frac{m\omega}{\hbar}}\lambda. \quad (3.67)$$

3.3.2. Equilibrium and the Hessian matrix

We follow the steps of the investigations in the previous section for the Newtonian interaction. It is convenient to define

$$I = \int \mathrm{d}^3\kappa \left(\frac{1}{\kappa^2} + \frac{\alpha}{\kappa^2 + \bar{\lambda}^{-2}}\right) \exp\left\{-\frac{1}{2}(\gamma_x^2\kappa_x^2 + \gamma_y^2\kappa_y^2 + \gamma_z^2\kappa_z^2)\right\}, \quad (3.68)$$

which we split into the two parts $I = I_{\text{N}} + I_{\text{Yuk}}$. The first is the Newtonian interaction treated in Sec. 3.2, while the second describes the correction due to the Yukawa-like

interaction

$$I_{\mathrm{Yuk}} = \int \mathrm{d}^3\kappa \; \frac{\alpha}{\kappa^2 + \bar{\lambda}^{-2}} \exp\left\{-\frac{1}{2}(\gamma_x^2\kappa_x^2 + \gamma_y^2\kappa_y^2 + \gamma_z^2\kappa_z^2)\right\}. \tag{3.69}$$

The first derivatives regarding the dimensionless Gauss width γ_j are

$$\partial_{\gamma_j} I_{\mathrm{Yuk}} = -\gamma_j \int \mathrm{d}^3\kappa \; \frac{\alpha}{\kappa^2 + \bar{\lambda}^{-2}} \kappa_j^2 \exp\left\{-\frac{1}{2}(\gamma_x^2\kappa_x^2 + \gamma_y^2\kappa_y^2 + \gamma_z^2\kappa_z^2)\right\} \tag{3.70}$$

and second derivatives leads to the diagonal and off-diagonal elements

$$\partial_{\gamma_j}^2 I_{\mathrm{Yuk}} = \int \mathrm{d}^3\kappa \; \frac{\alpha}{\kappa^2 + \bar{\lambda}^{-2}} (\gamma_j^2\kappa_j^4 - \kappa_j^2) \; \exp\left\{-\frac{1}{2}(\gamma_x^2\kappa_x^2 + \gamma_y^2\kappa_y^2 + \gamma_z^2\kappa_z^2)\right\}, \tag{3.71a}$$

$$\partial_{\gamma_j}\partial_{\gamma_k} I_{\mathrm{Yuk}} = \gamma_j\gamma_k \int \mathrm{d}^3\kappa \; \frac{\alpha}{\kappa^2 + \bar{\lambda}^{-2}} \kappa_j^2\kappa_k^2 \; \exp\left\{-\frac{1}{2}(\gamma_x^2\kappa_x^2 + \gamma_y^2\kappa_y^2 + \gamma_z^2\kappa_z^2)\right\}. \tag{3.71b}$$

From this point on, we apply the spherical symmetry (3.11) and solve the integrals (3.70) and (3.71) under these conditions. Because of the symmetry, we use spherical coordinates given in (3.41). Since the Fourier transformed potential does only depend on the radial coordinate κ, the angular parts are the same as in the Newtonian case, see Eqs. (3.42), (3.50) and (3.54).

Consequently, the radial integral remains in the right-hand side of Eq. (3.70), which we denote as

$$J_{\mathrm{Yuk}} = -\gamma \frac{4\pi}{3} \int \mathrm{d}\kappa \; \frac{\alpha\kappa^4}{\kappa^2 + \bar{\lambda}^{-2}} \exp\left\{-\frac{1}{2}\gamma^2\kappa^2\right\}. \tag{3.72}$$

As shown in the Appendix B.3, this expression is solved by

$$J_{\mathrm{Yuk}} = -\frac{4\pi}{3}\alpha\sqrt{\frac{\pi}{2}} \left(\frac{1}{\gamma^2} - \frac{1}{\bar{\lambda}^2} + \sqrt{\frac{\pi}{2}}\frac{\gamma}{\bar{\lambda}^3} \exp\left\{\frac{\gamma^2}{2\bar{\lambda}^2}\right\} \mathrm{erfc}\left[\sqrt{\frac{\gamma^2}{2\bar{\lambda}^2}}\right]\right). \tag{3.73}$$

With this result we obtain an additional term in the ODE (2.34). The differential equation including contact, Newtonian, and Yukawa-like interaction then reads

$$\ddot{\gamma} = -\nu^2\gamma + \frac{1}{\gamma^3} + \frac{P}{\gamma^4} - \frac{Q}{\gamma^2} - \alpha Q \left(\frac{1}{\gamma^2} - \frac{1}{\bar{\lambda}^2} + \sqrt{\frac{\pi}{2}}\frac{\gamma}{\bar{\lambda}^3} \exp\left\{\frac{\gamma^2}{2\bar{\lambda}^2}\right\} \mathrm{erfc}\left[\sqrt{\frac{\gamma^2}{2\bar{\lambda}^2}}\right]\right). \tag{3.74}$$

For both gravitational interactions we have the identical interaction strength Q as defined in (3.46). The equilibrium cloud width is then determined by

$$-\nu^2\gamma_0 + \frac{1}{\gamma_0^3} + \frac{P}{\gamma_0^4} - \frac{Q}{\gamma_0^2} - \alpha Q\left(\frac{1}{\gamma_0^2} - \frac{1}{\bar{\lambda}^2} + \sqrt{\frac{\pi}{2}}\frac{\gamma_0}{\bar{\lambda}^3}\exp\left\{\frac{\gamma_0^2}{2\bar{\lambda}^2}\right\}\operatorname{erfc}\left[\sqrt{\frac{\gamma^2}{2\bar{\lambda}^2}}\right]\right) = 0. \tag{3.75}$$

Next, we derive the Hessian matrix. To do this, we evaluate the right-hand side of Eq. (3.71) with spherical symmetry (3.11) and spherical coordinates (3.41). As already mentioned, the angular integration is identical to the Newtonian case (3.50) and (3.54), since the potential depends only on the radial coordinate κ. Thus, we only have to perform the radial integral for both the diagonal and the off-diagonal elements.

For the diagonal elements we have the radial integral

$$J_{\text{Yuk}}^{(jj)} = 4\pi\int_0^\infty \mathrm{d}\kappa\ \kappa^2\left(\frac{\gamma^2}{5}\kappa^4 - \frac{1}{3}\kappa^2\right)\frac{\alpha}{\kappa^2+\bar{\lambda}^{-2}}\exp\left\{-\frac{1}{2}\gamma^2\kappa^2\right\}. \tag{3.76}$$

The detailed calculation can be found in the Appendix B.3. Here, we only mention the result

$$\begin{aligned} J_{\text{Yuk}}^{(jj)} = 4\pi\sqrt{\frac{\pi}{2}}\Bigg[&\frac{4}{15}\frac{1}{\gamma^3} + \frac{2}{15}\frac{1}{\gamma\bar{\lambda}^2} + \frac{1}{5}\frac{\gamma}{\bar{\lambda}^4} \\ &- \sqrt{\frac{\pi}{2}}\left(\frac{1}{3}\frac{1}{\bar{\lambda}^3} + \frac{1}{5}\frac{\gamma^2}{\bar{\lambda}^5}\right)\exp\left\{\frac{\gamma^2}{2\bar{\lambda}^2}\right\}\operatorname{erfc}\left[\sqrt{\frac{\gamma^2}{2\bar{\lambda}^2}}\right]\Bigg]. \end{aligned} \tag{3.77}$$

Evaluating at the equilibrium point γ_0 and including the prefactors of the Lagrangian (3.66) and the Hessian (2.42), the contribution of the Yukawa-like interaction to the diagonal elements in the Hessian matrix is

$$M_{\text{Yuk}}^{(jj)} = -\alpha Q\left(\frac{4}{5}\frac{1}{\gamma_0^3} + \frac{2}{5}\frac{1}{\gamma_0\bar{\lambda}^2} + \frac{3}{5}\frac{\gamma_0}{\bar{\lambda}^4} - \sqrt{\frac{\pi}{2}}\left(\frac{1}{\bar{\lambda}^3} + \frac{3}{5}\frac{\gamma_0^2}{\bar{\lambda}^5}\right)\exp\left\{\frac{\gamma_0^2}{2\bar{\lambda}^2}\right\}\operatorname{erfc}\left[\sqrt{\frac{\gamma_0^2}{2\bar{\lambda}^2}}\right]\right), \tag{3.78}$$

where we used the definition of the gravitational interaction strength Q from (3.46).

The off-diagonal elements result in

$$J_{\mathrm{Yuk}}^{(jk)} = \frac{4\pi}{15}\gamma^2 \int_0^\infty \mathrm{d}\kappa\, \kappa^6 \frac{\alpha}{\kappa^2 + \bar{\lambda}^{-2}} \exp\left\{-\frac{1}{2}\gamma^2\kappa^2\right\}, \tag{3.79}$$

which gives

$$J_{\mathrm{Yuk}}^{(jk)} = \alpha\, 4\pi\sqrt{\frac{\pi}{2}}\left(\frac{1}{5}\frac{1}{\gamma^3} - \frac{1}{15}\frac{1}{\gamma\bar{\lambda}^2} + \frac{1}{15}\frac{\gamma}{\bar{\lambda}^4} - \sqrt{\frac{\pi}{2}}\frac{1}{15}\frac{\gamma^2}{\bar{\lambda}^5}\exp\left\{\frac{\gamma^2}{2\bar{\lambda}^2}\right\}\mathrm{erfc}\left[\sqrt{\frac{\gamma^2}{2\bar{\lambda}^2}}\right]\right). \tag{3.80}$$

Thus, analogously the off-diagonal elements of the Hessian matrix are given by

$$M_{\mathrm{Yuk}}^{(jk)} = -\alpha Q\left(\frac{3}{5}\frac{1}{\gamma_0^3} - \frac{1}{5}\frac{1}{\gamma_0\bar{\lambda}^2} + \frac{1}{5}\frac{\gamma_0}{\bar{\lambda}^4} - \sqrt{\frac{\pi}{2}}\frac{1}{5}\frac{\gamma_0^2}{\bar{\lambda}^5}\exp\left\{\frac{\gamma_0^2}{2\bar{\lambda}^2}\right\}\mathrm{erfc}\left[\sqrt{\frac{\gamma_0^2}{2\bar{\lambda}^2}}\right]\right), \tag{3.81}$$

due to the Yukawa-like interaction

With the Yukawa corrections to the diagonal and off-diagonal elements given by (3.78) and (3.81), the full Hessian matrix M containing the contact interaction as well as both Newtonian and Yukawa corrections, consists of the entries

$$\begin{aligned} M^{(jj)} = \nu^2 &+ \frac{3}{\gamma_0^4} + \frac{2P}{\gamma_0^5} - \frac{4}{5}\frac{Q}{\gamma_0^3} - \alpha Q\left(\frac{4}{5}\frac{1}{\gamma_0^3} + \frac{2}{5}\frac{1}{\gamma_0\bar{\lambda}^2} + \frac{3}{5}\frac{\gamma_0}{\bar{\lambda}^4}\right. \\ &\left. - \sqrt{\frac{\pi}{2}}\left(\frac{1}{\bar{\lambda}^3} + \frac{3}{5}\frac{\gamma_0^2}{\bar{\lambda}^5}\right)\exp\left\{\frac{\gamma_0^2}{2\bar{\lambda}^2}\right\}\mathrm{erfc}\left[\sqrt{\frac{\gamma_0^2}{2\bar{\lambda}^2}}\right]\right), \end{aligned} \tag{3.82a}$$

$$\begin{aligned} M^{(jk)} = &\frac{P}{\gamma_0^5} - \frac{3}{5}\frac{Q}{\gamma_0^3} - \alpha Q\left(\frac{3}{5}\frac{1}{\gamma_0^3} - \frac{1}{5}\frac{1}{\gamma_0\bar{\lambda}^2} + \frac{1}{5}\frac{\gamma_0}{\bar{\lambda}^4}\right. \\ &\left. - \sqrt{\frac{\pi}{2}}\frac{1}{5}\frac{\gamma_0^2}{\bar{\lambda}^5}\exp\left\{\frac{\gamma_0^2}{2\bar{\lambda}^2}\right\}\mathrm{erfc}\left[\sqrt{\frac{\gamma_0^2}{2\bar{\lambda}^2}}\right]\right) \end{aligned} \tag{3.82b}$$

for $j \neq k$. Its eigenvalues and thus the collective frequencies are calculated numerically in the next section.

As a short remark at the end of this part, we investigate here a limiting case of the Yukawa corrections. In the case of infinite interaction range $\lambda \to \infty$ both the exponential and the complementary error function tend to the value one, leaving only the first part of the Yukawa correction. The differential equation (3.74) and the elements of the Hessian

matrix (3.82) simplify in this limit to

$$\ddot{\gamma} \to -\nu^2\gamma + \frac{1}{\gamma^3} + \frac{P}{\gamma^4} - \frac{Q}{\gamma^2} - \alpha\,\frac{Q}{\gamma^2}, \tag{3.83a}$$

$$M^{(jj)} \to \nu^2 + \frac{3}{\gamma_0^4} + \frac{2P}{\gamma_0^5} - \frac{4}{5}\frac{Q}{\gamma_0^3} - \alpha\,\frac{4}{5}\frac{Q}{\gamma_0^3}, \tag{3.83b}$$

$$M^{(jk)} \to \frac{P}{\gamma_0^5} - \frac{3}{5}\frac{Q}{\gamma_0^3} - \alpha\,\frac{3}{5}\frac{Q}{\gamma_0^3}. \tag{3.83c}$$

Reducing the strength α to zero leads to the results (3.47) and (3.57) from the previous section.

3.3.3. Discussion

In this section we numerically evaluate the collective frequencies of a spherical condensate interacting via a Yukawa-like potential. For this, we have to solve the equation for the equilibrium cloud width (3.75), insert the results into the Hessian matrix given by Eq. (3.82) and calculate its eigenvalues. We set the values for the contact interaction strength P and the gravitational interaction strength Q fixed, while keeping the Yukawa parameters α and λ as variables. This allows us to create contour plots, which we then compare to experimental results shown in the introduction of Sec. 1.2.

First of all, we choose $P = 446$ and $Q = 4.1 \cdot 10^{-19}$ according to the typical values shown previously in Sec. 3.1.3 and Sec. 3.2.3. Furthermore, the typical length scale of a condensate can be roughly characterized by the oscillator length $l = \sqrt{\hbar/(m\omega)}$, which is commonly in the μm regime. As a consequence, the interesting values for λ are around this length scale, i.e. it varies from 1 nm to 1 mm. For $\lambda > 1$mm, the interaction already includes the whole condensate, thus it is uniform. On the other side, for $\lambda < 1$nm there is effectively no interaction at all due of the dilute nature of condensates. Considering values of α, we need to check whether the GPE theory, namely the assumption of a mean-field, is valid. For this, we compare the energy contributions of the two-particles interactions in the Lagrangian. The Lagrangian for the contact interaction was already derived as in Eq. (3.3). An estimate for the Lagrangian of the Newtonian interaction is obtained by a rough but simple approximation. If we focus just on the breathing mode, we allow only a radial oscillation, i.e. the Gauss widths and their variations are identical, namely $A_x = A_y = A_z = A$ and $\delta A_x = \delta A_y = \delta A_z = \delta A$. Under these conditions, we evaluate the Lagrangian in Eq. (3.34) in spherical coordinates. The integrals are easily

solved and the result is

$$L_{\mathrm{N}} = \frac{uN^2}{\sqrt{2\pi}}\frac{1}{A}. \tag{3.84}$$

Strictly speaking, this is only valid for the breathing mode. However, as we have seen in previous chapters, the quadrupole modes are of the same order of magnitude.

Assuming the particle number $N = 10^5$ and the Gaussian width A given by the oscillator length as a length scale, we roughly estimate for a ^{87}Rb condensate with the typical values in Eqs. (3.19) and (3.20)

$$L_{\mathrm{con}} = -\frac{gN^2}{2\sqrt{(2\pi)^3}}\frac{1}{A^3} = -\frac{4\pi\hbar^2}{m}a_{\mathrm{s}}\frac{N^2}{2\sqrt{(2\pi)^3}}\frac{1}{A^3} \sim -10^{-24}\mathrm{J}, \tag{3.85a}$$

$$L_{\mathrm{N}} = \frac{uN^2}{\sqrt{2\pi}}\frac{1}{A} = \frac{Gm^2}{\sqrt{2\pi}}N^2\frac{1}{A} \sim 10^{-45}\mathrm{J}. \tag{3.85b}$$

Since the Newtonian is roughly twenty orders of magnitude smaller than the contribution of the contact interaction, the gravitational contribution can be neglected.

However, as we mentioned before, a fifth force, e.g. a Yukawa interaction, introduces an additional interaction strength α, which in principle can compensate the difference between Newtonian and contact interaction. Analogous to the Lagrangian for the Newton interaction, we derive the Lagrangian for the Yukawa-like interaction by focusing only on the breathing mode. Thus, under the same conditions as before, we have to solve the integrals in the Lagrangian (3.66) in spherical coordinates. As shown in detail in the Appendix B.4, this results in

$$L_{\mathrm{Yuk}} = \frac{uN^2}{\sqrt{2\pi}}\frac{1}{A} + \alpha\frac{uN^2}{\sqrt{2\pi}}\left(\frac{1}{A} - \sqrt{\frac{\pi}{2}}\frac{1}{\lambda}\exp\left\{\frac{A^2}{2\lambda^2}\right\}\mathrm{Erfc}\left[\sqrt{\frac{A}{2\lambda}}\right]\right). \tag{3.86}$$

To simplify the discussion, we introduce $x = \sqrt{A/(2\lambda)}$ as a short-hand notation, such that

$$L_{\mathrm{Yuk}} = \frac{uN^2}{\sqrt{2\pi}}\frac{1}{A} + \alpha\frac{uN^2}{\sqrt{2\pi}}\left(\frac{1}{A} - \frac{\sqrt{\pi}}{A}x\exp\left\{x^2\right\}\mathrm{Erfc}\left[x\right]\right). \tag{3.87}$$

In the limit $x \to 0$, corresponding to an infinite interaction range $\lambda \to \infty$, we get

$$L_{\mathrm{Yuk}} \to \frac{uN^2}{\sqrt{2\pi}} \frac{1}{A} + \alpha \frac{uN^2}{\sqrt{2\pi}} \frac{1}{A}. \tag{3.88}$$

For infinite interaction length λ, the Lagrangian is therefore identical to the Newtonian case multiplied by a constant α, as seen in Fig. 3.4 at the level of the potential. In this case, an estimation with the same particle number N and Gauss width A as above leads to

$$L_{\mathrm{Yuk}} \to \alpha \frac{Gm^2}{\sqrt{2\pi}} N^2 \frac{1}{A} \sim 10^{-45}\mathrm{J} \cdot \alpha \tag{3.89}$$

in the limit of infinite interaction range. For $\alpha < 10^{21}$, the contribution of the Yukawa interaction is equal to or less than the contact contribution. This suggests that the mean-field description is valid for these values of the interaction strength α.

On the other hand, for small effective ranges $\lambda \to 0$ or $x \to \infty$ respectively, we have

$$L_{\mathrm{Yuk}} \to \frac{uN^2}{\sqrt{2\pi}} \frac{1}{A} + \alpha \frac{uN^2}{\sqrt{2\pi}} \left(\frac{1}{A} - \frac{\sqrt{\pi}}{A} \frac{1}{\sqrt{\pi}} \right) = L_{\mathrm{N}}. \tag{3.90}$$

This is intuitively clear, as according to the definition of the Yukawa potential (3.64) the additional term vanishes in the case $\lambda = 0$. Thus, it coincides with the Newton potential and is therefore independent of α. This phenomenon can also be seen in Fig. 3.4, as we decrease the effective range. A better approximation for small but finite interaction ranges is achieved by the series expansion up to second order. To do this, we approximate in the Lagrangian (3.87)

$$x \exp\left\{x^2\right\} \mathrm{Erfc}\left[x\right] \approx \frac{1}{\sqrt{\pi}} - \frac{1}{2\sqrt{\pi}} \frac{1}{x^2}. \tag{3.91}$$

Now the first term cancels, but the second remains, so

$$L_{\mathrm{Yuk}} \to +\alpha \frac{uN^2}{\sqrt{2\pi}} \frac{1}{A} \cdot \frac{1}{2\sqrt{\pi}} \frac{1}{x^2}, \tag{3.92}$$

Table 3.2.: Upper boundaries for the interaction strength α depending on the effective range λ, such that the Yukawa interaction is smaller or comparable to the contact interaction. Therefore the mean-field description is still valid. The values are calculated with Eq. (3.94). In the limit $\lambda \to \infty$ Eq. (3.89) holds.

λ [m]	10^{-10}	10^{-9}	10^{-8}	10^{-7}	10^{-6}	∞
α	10^{28}	10^{26}	10^{24}	10^{22}	10^{20}	10^{21}

which in terms of the effective interaction range λ leads to the estimation

$$L_{\text{Yuk}} \to \alpha \frac{uN^2}{\sqrt{2\pi}} \frac{1}{A^3} \lambda^2 \sim 10^{-32} \frac{\text{J}}{\text{m}^2} \cdot \alpha \lambda^2. \tag{3.93}$$

Following the same arguments as above, we derive a simple relation between the Yukawa parameter

$$\alpha = 10^8 \text{ m}^2 \, \frac{1}{\lambda^2}. \tag{3.94}$$

A few exemplary values for pairs of the Yukawa parameter are shown in Tab. 3.2. There we see that e.g. for $\lambda = 1$ nm we have $\alpha < 10^{26}$. The last value shows the limit for infinite effective range shown in Eq. (3.89). This suggests that even for $\lambda = 1$ μm we can safely assume $\alpha < 10^{21}$.

With these possible values for the Yukawa parameters α and λ, we can now go further into detail of the numerical calculation. First of all, we rewrite the equation for the steady state containing the Yukawa correction (3.75)

$$\gamma_0^5 - \gamma_0 - P + Q\gamma_0^2 + \alpha Q \left(\gamma_0^2 - \frac{\gamma_0^4}{\bar{\lambda}^2} + \sqrt{\frac{\pi}{2}} \frac{\gamma_0^5}{\bar{\lambda}^3} \exp\left\{ \frac{\gamma_0^2}{2\bar{\lambda}^2} \right\} \text{erfc}\left[\frac{\gamma_0}{\sqrt{2}\bar{\lambda}} \right] \right) = 0 \tag{3.95}$$

and numerically search for the roots of the function on the left hand-side for a given set of α and $\bar{\lambda}$. Unfortunately, we cannot take advantage of Descartes' rule of sign to Eq. (3.95) due to the transcendental functions. A series expansion of both the exponential and the complementary error function leads to a polynomial of infinite order with alternating signs. According to Descartes' rule, there can be an infinite number of roots. In this case we have to check that these are the only physical plausible roots.

Using the dimensionless transformation (2.33) backwards, we can now express the

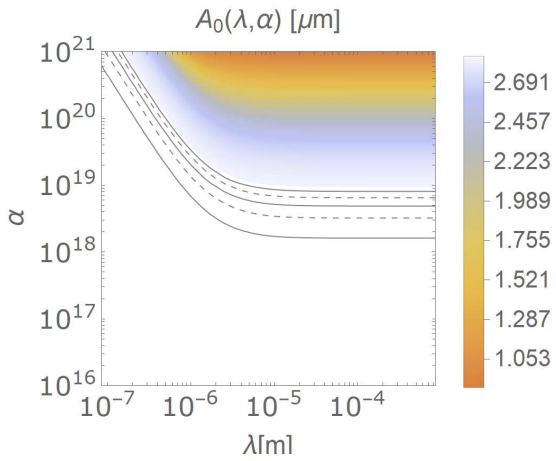

Figure 3.5.: Contour plot for the equilibrium cloud width $A_0(\lambda, \alpha)$ for $P = 446$ and $Q = 4.1 \cdot 10^{-19}$. The black lines indicate a difference of 0.01 μm to 0.05 μm compared to the Newtonian case given in Eq. (3.63). For better visibility, the curves alternate between solid and dashed lines.

values of the equilibrium cloud width γ_0 in physical units, which is the Gauss width A_0 depending on α and λ. For the typical example of ^{87}Rb we insert the parameters given in (3.19) and (3.20) as in the previous section.

The results are shown in Fig. 3.5. We plot the physical value of the Gauss width A_0 as a color coded contour plot. The black curves correspond to a difference of 0.01 μm up to 0.05 μm compared to the Newtonian case given in Eq. (3.63) in the previous section. To distinguish each curve we choose to show the lines as solid or dashed alternating. Significant changes occur for higher values of $\alpha > 10^{18}$. A larger interaction strength leads to a smaller equilibrium width, as expected from an attractive gravitational interaction. On the other hand, for an effective interaction range of $\lambda > 10^{-5}$m, the curves become flat because the whole mass is already concentrated within this length.

We plug the values for the dimensionless equilibrium width γ_0 now into the Hessian matrix given by (3.82) to calculate the eigenvalues representing the collective frequencies. As already seen in the analytical results (3.59), it turns out that the two quadrupole modes are degenerated, hence they occur with the same frequency. Both frequencies of the breathing mode Ω_{br} and the quadrupole modes Ω_{qu} are shown in Fig. 3.6. Again, we show the physical values in colors and differences ranging from 1 Hz to 5 Hz compared to the Newtonian case given in Eq. (3.63) as black curves. Qualitatively, the plots show the same behavior as for the equilibrium width, except that the frequencies increase

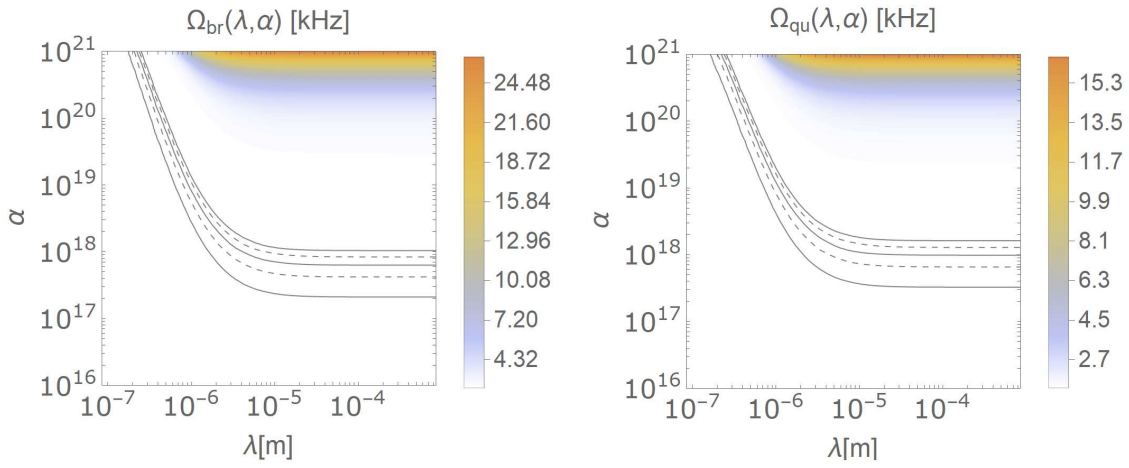

Figure 3.6.: Contour plot for the breathing frequency $\Omega_{\mathrm{br}}(\lambda, \alpha)$ and the quadrupole frequency $\Omega_{\mathrm{qu}}(\lambda, \alpha)$ for $P = 446$ and $Q = 4.1 \cdot 10^{-19}$. The black lines indicate a difference of 1 Hz to 5 Hz compared to the Newtonian case given in Eq. (3.63). For better visibility, the curves alternate between solid and dashed lines.

for stronger interactions, similar to the Newtonian case. Comparing the physical values of both frequencies, the breathing frequency is higher than the quadrupole frequency, similar to the results of the previous sections. This is why the lines indicating a difference of a fixed value like 1 Hz is slightly lower for the breathing frequency.

In the following, we investigate the influence of certain physical parameters such as the particle number and the s-wave scattering length onto the contour plots shown in Fig. 3.6. In the experiment, it is possible to produce condensates with higher particle numbers N or tune the s-wave scattering length a_{s} via Feshbach resonances mentioned in the introduction. As such, we show the breathing frequency in Fig. 3.7 and the quadrupole frequency in Fig. 3.8 for 10^5 to 10^9 particles with scattering lengths between 10^{-9} m and 10^{-11} m. Increasing each parameter leads to higher collective frequencies, which finally results in frequencies of several MHz. If we hypothetically reach a precision of 1 Hz, represented by the lowest black line in each plot, we clearly see that higher particle numbers and lower scattering lengths are favorable to set the best constraints for the Yukawa parameters α and λ. In these examples, we find $\alpha \sim 10^{14}$ as the lowest bound for at effective range of $\lambda \sim 10$ μm. Again, if we look closely, the frequency of the breathing mode Ω_{br} gives slightly better results than those of the quadrupole mode Ω_{qu},

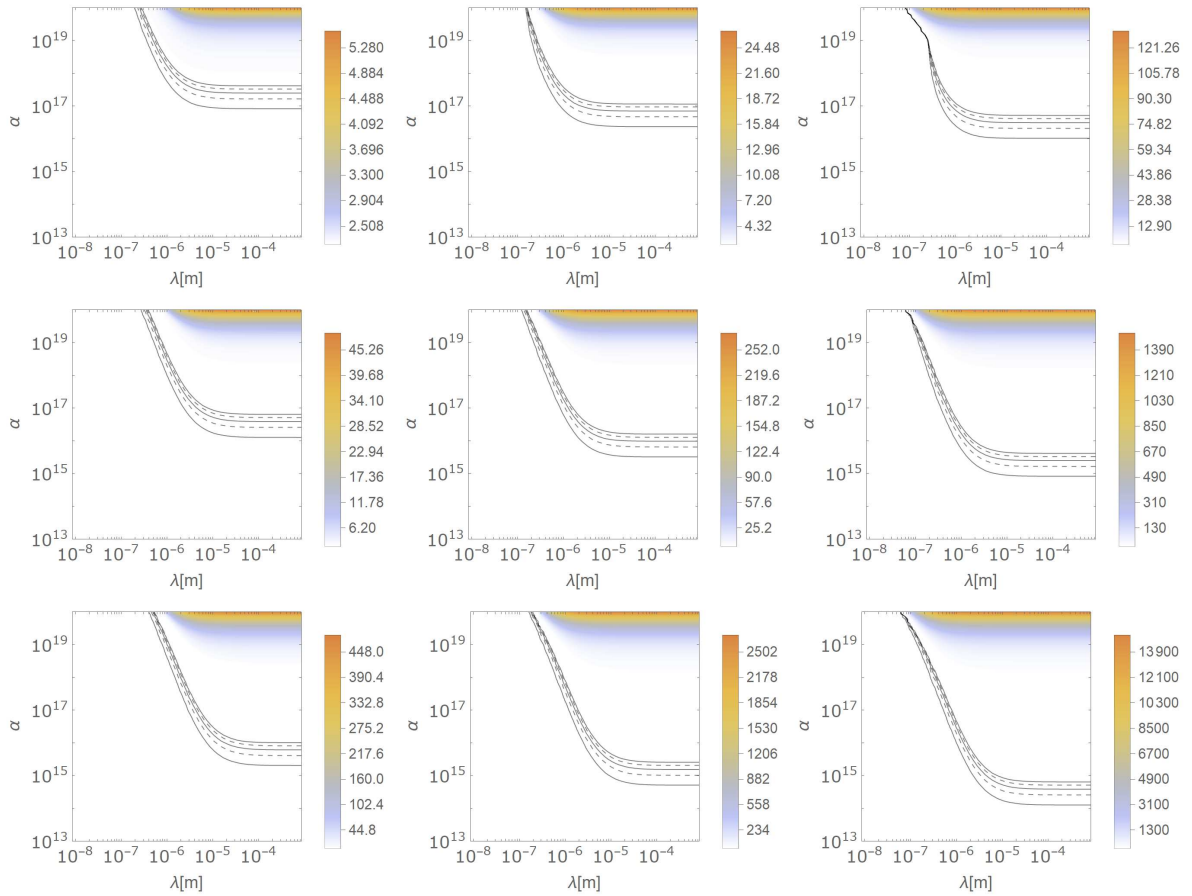

Figure 3.7.: Frequency $\Omega_{\mathrm{br}}(\lambda, \alpha)$ in units of 1 kHz for varying particle number N and scattering length a_{s}. Each row shows $N = 10^5$, $N = 10^7$ and $N = 10^9$ and each column $a_{\mathrm{s}} = 10^{-9}$ m, $a_{\mathrm{s}} = 10^{-10}$ m and $a_{\mathrm{s}} = 10^{-11}$ m. The black lines indicate a difference of 1 Hz to 5 Hz compared to the Newtonian case given in Eq. (3.63). For better visibility, the curves alternate between solid and dashed lines.

as Ω_{br} is in general larger.

Next, we also show how the trap frequency affects the collective frequencies. In the experiment, this is controlled by the frequency of the laser beams used for the magneto-optical trap. For the calculations we assume trap frequencies of 10^3 Hz to 10^5 Hz. The results are shown in Fig. 3.9 for both the breathing frequency and the quadrupole frequency. Increasing the trap frequency leads to higher values of the collective frequencies and also to better constraints for α. Note that we also shift the black lines indicating a difference to the Newtonian case towards lower effective ranges λ, because the con-

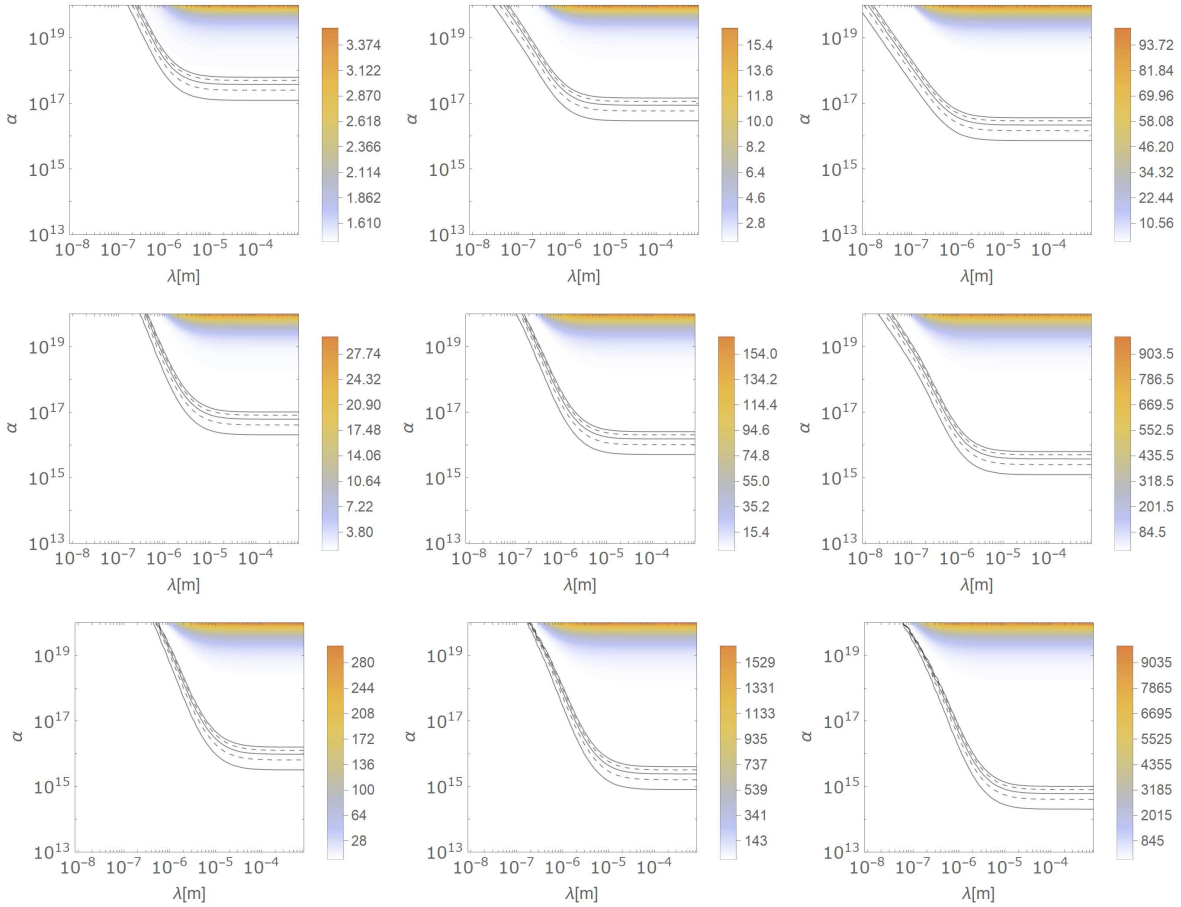

Figure 3.8.: Frequency $\Omega_{\mathrm{qu}}(\lambda, \alpha)$ in units of 1 kHz for varying particle number N and scattering length a_{s}. Each row shows $N = 10^5$, $N = 10^7$ and $N = 10^9$ and each column $a_{\mathrm{s}} = 10^{-9}$ m, $a_{\mathrm{s}} = 10^{-10}$ m and $a_{\mathrm{s}} = 10^{-11}$ m. The black lines indicate a difference of 1 Hz to 5 Hz compared to the Newtonian case given in Eq. (3.63). For better visibility, the curves alternate between solid and dashed lines.

version factor between dimensionless values and those in physical units depends on the trap frequency ω, see Eq. (3.67). As a consequence, we hypothetically improve the constraints of effective range by one order of magnitude by increasing the trap frequency to $\omega = 10^5$ Hz.

Instead of increasing the trap frequency, which is only possible for one or two orders of magnitude in the experiment and therefore only marginally realistic for further improvement, we can increase the precision of the frequency measurement. In Fig. 3.10 we assume that we measure the collective frequency with a precision of 10 Hz (left),

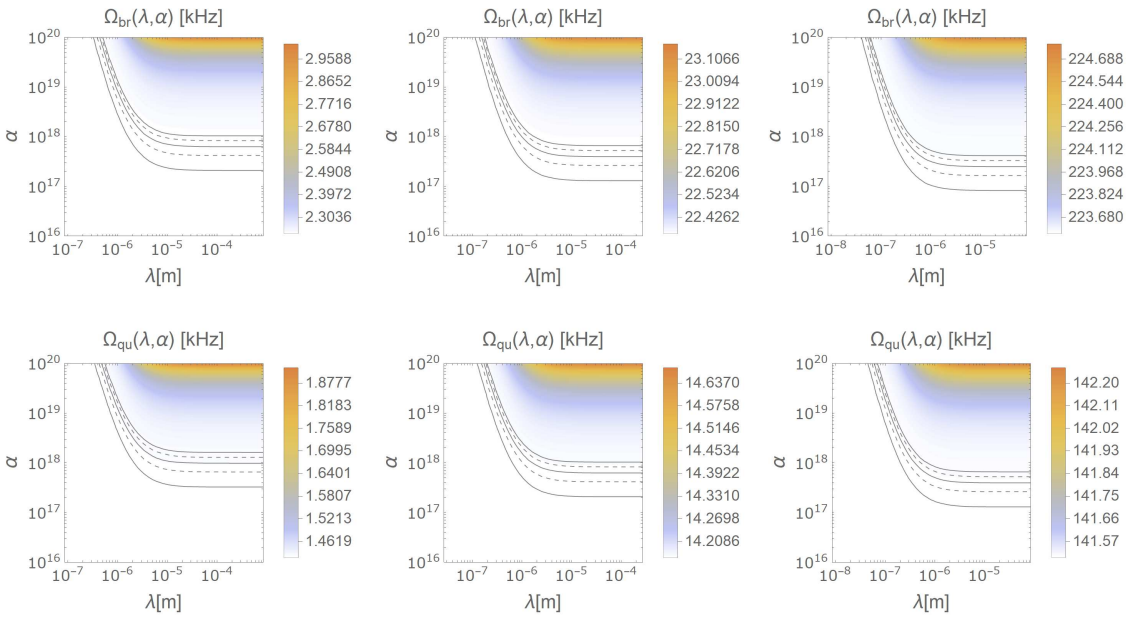

Figure 3.9.: Breathing and quadrupole frequency $\Omega_{\mathrm{br}}(\lambda, \alpha)$ and $\Omega_{\mathrm{qu}}(\lambda, \alpha)$ for a varying trap frequency $\omega = 10^3$ Hz, $\omega = 10^4$ Hz and $\omega = 10^5$ Hz. The black lines indicate a difference of 1 Hz to 5 Hz compared to the Newtonian case given in Eq. (3.63). For better visibility, the curves alternate between solid and dashed lines. Note that the range of λ differs for each column.

1 Hz (middle) and 0.1 Hz (right). The color coded contour plot in all three pictures is the same for each frequency Ω_{br} and Ω_{qu}, respectively. The measurements precision only affects the black lines, indicating the difference compared to the Newtonian results. Similar to the results in Fig. 3.9, we reach constraints for the interactions strength $\alpha \approx 10^{16}$ by increasing the precision to 0.1 Hz. On the other hand, we only slightly improve the constraints for the effective range λ in contrast to Fig. 3.9, since the range depends directly on the trap frequency ω, but not on the precision of the measurement. As a consequence, increasing the trap frequency instead of the precision of the measurement turns out to be more valuable in considerations for future experiments.

Lastly, and in regards of gravity, the most obvious choice is a variation of the mass. We consider ^{7}Li as a very light atom species, ^{87}Rb as the typical condensate and ^{174}Yb as the heaviest element, which were successfully condensed, see Ref. [17]. Since the s-wave scattering length a_{s} depends on the chosen species we now have two possibilities: First, we use the corresponding natural scattering length for each mass, which are $a_{\mathrm{s}}^{\mathrm{Li}} = 33a_0$, $a_{\mathrm{s}}^{\mathrm{Rb}} = 90a_0$ [38] and $a_{\mathrm{s}}^{\mathrm{Yb}} = 104a_0$ [113] in units of the Bohr radius $a_0 = 5.29{\cdot}10^{-11}$ m. The

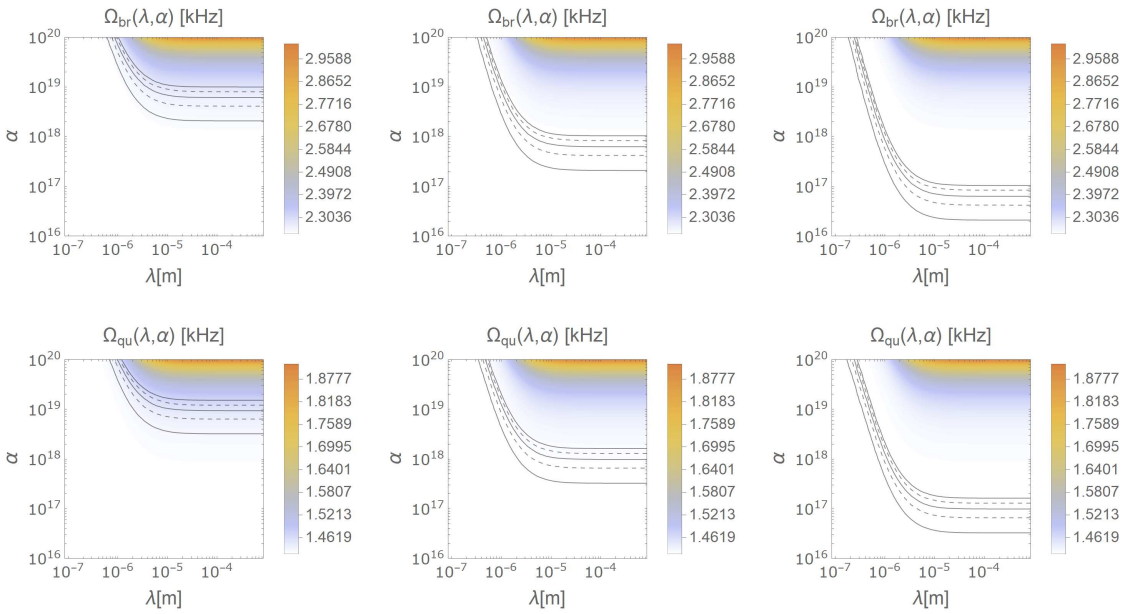

Figure 3.10.: Breathing and quadrupole frequency $\Omega_{\mathrm{br}}(\lambda, \alpha)$ and $\Omega_{\mathrm{qu}}(\lambda, \alpha)$ for a the trap frequency $\omega = 10^3$ Hz. The black lines indicate a difference of 10 Hz, 1 Hz and 0.1 Hz to the Newtonian results in Eq. (3.63), respectively. For better visibility, the curves alternate between solid and dashed lines.

results are shown in Fig. 3.11. Secondly, for a better comparison and with the argument of Feshbach resonances, we set a fixed value for the scattering length as $a_{\mathrm{s}} = 1$ nm to particularly observe the mass dependency of the collective frequencies. These results are shown in Fig. 3.12. In both cases the figures look quite similar. Larger masses result in higher frequencies and again the quadrupole frequency in absolute units is smaller than the breathing frequency. For ^{7}Li, the black lines advocate very rough constraints on the Yukawa parameters and are barely visible in the region shown. This is expected because the gravitational interaction should be small for small masses. Increasing the mass improves these constraints such that for ^{174}Yb the lowest black line is of the order $\alpha \sim 10^{16}$. We also notice a very small shift to smaller effective ranges λ, as the conversion factor between the dimensionless value and its corresponding physical value depends on the mass. This is the same pattern we have seen earlier with the trap frequency, but with a much smaller effect because we are only changing the mass by two orders of magnitude.

To summarize, with our model of a self-gravitating spherical condensate interacting

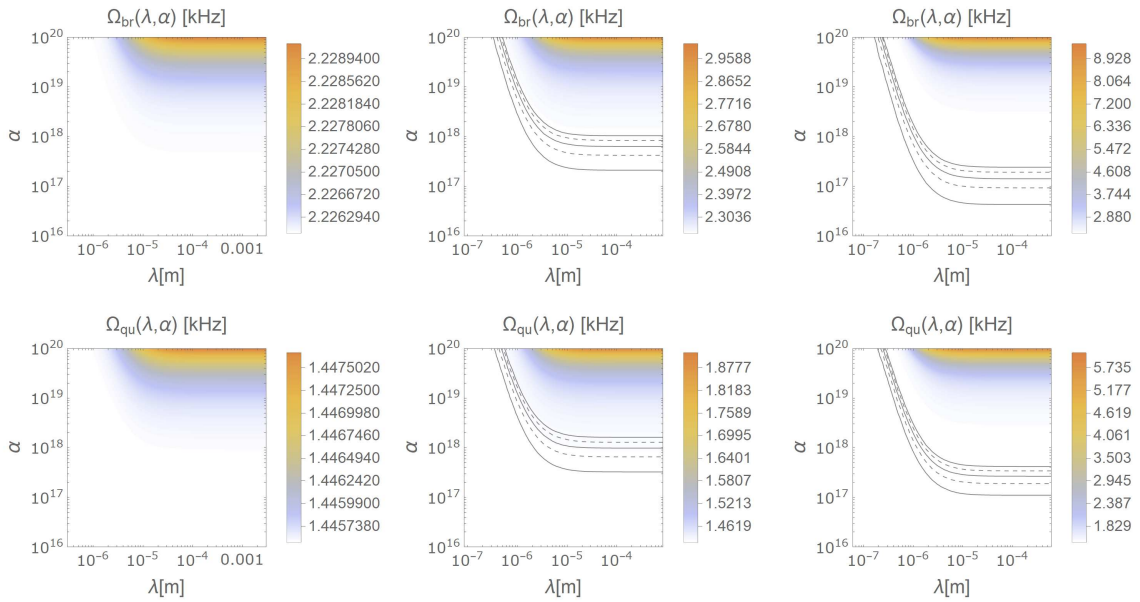

Figure 3.11.: Breathing and quadrupole frequency $\Omega_{\mathrm{br}}(\lambda, \alpha)$ and $\Omega_{\mathrm{qu}}(\lambda, \alpha)$ for different atomic species with their respective scattering length: ^{7}Li ($a_{\mathrm{s}} = 33a_0$) (left), ^{87}Rb ($a_{\mathrm{s}} = 90a_0$) (mid) and ^{174}Yb ($a_{\mathrm{s}} = 104a_0$) (right). The black lines indicate a difference of 1 Hz to 5 Hz compared to the Newtonian case given in Eq. (3.63). For better visibility, the curves alternate between solid and dashed lines. For ^{7}Li the black lines are not visible, since the difference to the Newtonian case is smaller than 1 Hz in the shown area.

via a Yukawa-like potential, we find constraints on the interaction strength α and the effective range λ. These constraints can be improved by higher particle numbers N, lower scattering lengths a_{s}, larger trapping frequencies ω and of course heavier atom species. It turns out that the collective frequency of the breathing mode is better suited than that of the quadrupole mode.

Finally, in the end of this chapter, we compare our theoretical results to the experimentally verified constraints shown in the Introduction 1.2 in Fig. 1.4. We will use three examples, the first of which is the typical realizable condensate of ^{87}Rb with $N = 10^5$, $a_{\mathrm{s}} = 90a_0$ and $\omega = 1$ kHz. As the second example we choose ^{174}Yb with $N = 10^8$, $a_{\mathrm{s}} = 10^{-10}$ m and $\omega = 10$ kHz, which is more or less the limit of realizable condensates. And as a third condensate we assume hypothetically ^{174}Yb with $N = 10^{11}$, $a_{\mathrm{s}} = 10^{-11}$ m and $\omega = 10^3$ kHz in order to obtain better constraints. In Fig. 3.13 we show the results of each model embedded into Fig. 1.4 with the current experimental data. The colored curves each imply the difference of 1 Hz compared to the Newtonian case given

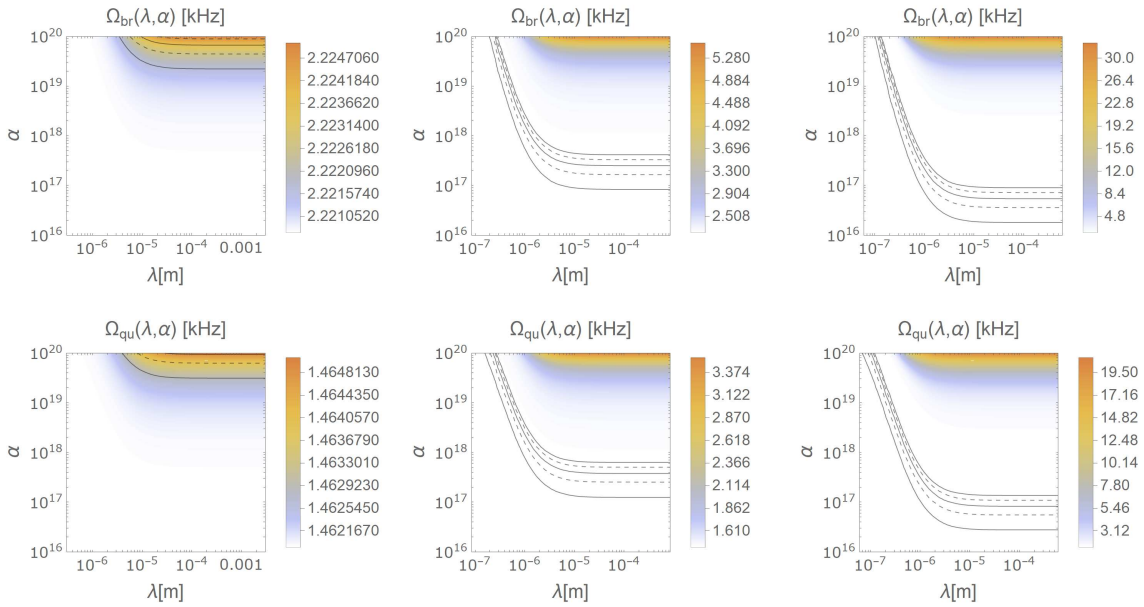

Figure 3.12.: Breathing and quadrupole frequency $\Omega_{\mathrm{br}}(\lambda, \alpha)$ and $\Omega_{\mathrm{qu}}(\lambda, \alpha)$ for different atomic species ^{7}Li (left), ^{87}Rb (mid) and ^{174}Yb (right) with fixed scattering length $a_{\mathrm{s}} = 10^{-9}$m. The black lines indicate a difference of 1 Hz to 5 Hz compared to the Newtonian case given in Eq. (3.63). For better visibility, the curves alternate between solid and dashed lines.

in Eq. (3.63). For the first case of a realistic ^{87}Rb condensate, the results are completely within the experimentally excluded area. The second example comes very close to the experimental boundary and even leads to slightly better constraints for $\lambda < 10^{-8}$ m, as seen at the blue shaded area. The largest improvements are achieved in theory for the third example of a Yb condensate. We can again see the effect of varying the trap frequency. As a consequence, it is essential to increase the trap frequency and as such the confinement of the condensate in order to reach significantly lower boundaries for the Yukawa parameters α and λ.

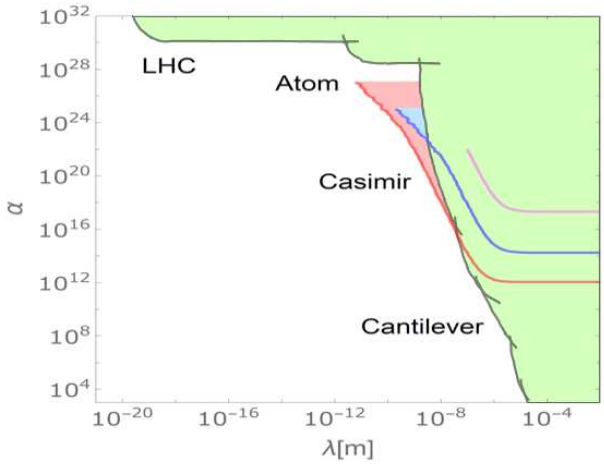

Figure 3.13.: Comparison between the experimental data shown in Ref. [69] and our results under the assumption of measuring a difference to the Newtonian case in Eq. (3.63) of 1 Hz. The magenta line is the result for a typical ^{87}Rb condensate ($N = 10^5$, $a_s = 90a_0$, $\omega = 10^3$ Hz), the blue line for a close to realistic ^{174}Yb condensate ($N = 10^8$, $a_s = 10^{-10}$ m, $\omega = 10^4$ Hz) and the red line for a hypothetical ^{174}Yb condensate ($N = 10^{11}$, $a_s = 10^{-11}$ m, $\omega = 10^6$ Hz). The blue and the red shaded area indicate improvements of the constraints for α and λ.

4. Collective modes in axially symmetric condensates

The variational approach is a powerful tool, as we have seen in the previous chapters by analyzing the dynamics of a spherical three dimensional condensate and determining the collective frequencies for three different types of particle interactions.

Another important application of this method is the derivation of effective equations describing a condensate in lower dimensions [114]. In the experiment, such condensates are realized in cylindrical external trap potentials, leading to cigar-shaped or disk-shaped condensates representing an effective one-dimensional or two-dimensional system, respectively. An interesting consequence of reducing the dimension of the system is a potentially higher interaction strength [115, 116]. The main question of this chapter will therefore be whether we can enhance the gravitational effects by changing the symmetry of the condensate.

To answer this, we generalize our model to axially symmetric condensates. Similar to the previous chapters, we will first review known results by only including the contact interaction. After that, we will include Newtonian and Yukawa-like gravitational interaction step-by-step. We also discuss the numerical results of all three cases depending on the interaction strengths as well as the aspect ratio of the trap, and compare them with the spherical equivalents.

4.1. Contact interaction

Analogous to the previous chapter for spherical condensates, we first consider only the contact interaction and reproduce already known results for the equilibrium cloud widths and the collective frequencies, as a reference see e.g. Ref. [99].

4.1.1. Collective modes

As we have mentioned in the beginning of this chapter, reducing the dimension of the condensate leads to higher effective contact interactions. We investigate now the effect of reducing the dimension on the collective frequencies. In Sec. 3.1 we already derived a general expression of the differential equation for the cloud width γ_j, see Eq. (3.7), especially for the equilibrium width γ_{j0} in (3.8), and for the Hessian matrix M given in Eq. (3.10). These equations are of course still valid in the case of axial symmetry, which is realized by setting two of the three spatial degrees of freedom identical, thus e.g.

$$\nu_x = \nu_y = \nu_t \ , \quad \gamma_{x0} = \gamma_{y0} = \gamma_{t0}. \tag{4.1}$$

Additionally, we introduce the aspect ratio

$$\zeta = \frac{\nu_z}{\nu_t}, \tag{4.2}$$

which describes the ratio between both trap frequencies in the longitudinal and in the transversal direction. Following Eq. (3.8), we now set $\nu_t = 1$ without loss of generality and replace ν_z by the aspect ratio ζ. This leads to the set of equations

$$\text{i)} \ -\gamma_{t0} + \frac{1}{\gamma_{t0}^3} + \frac{P}{\gamma_{t0}^3 \gamma_{z0}} = 0, \tag{4.3a}$$

$$\text{ii)} \ -\zeta^2 \gamma_{z0} + \frac{1}{\gamma_{z0}^3} + \frac{P}{\gamma_{t0}^2 \gamma_{z0}^2} = 0 \tag{4.3b}$$

for both equilibrium widths γ_{t0} in the transversal direction and γ_{z0} in the longitudinal direction. The contact interaction here in form of the dimensionless interaction strength P introduces a coupling between both equations. Thus, for the determination of the equilibrium cloud widths γ_{t0} and γ_{z0}, we have to solve both equations simultaneously. More on this topic can be found in Sec. 4.1.2, where we discuss the numerical evaluation.

Furthermore, we are able to describe different shapes of the condensate depending on the aspect ratio ζ. For $\zeta < 1$ or $\nu_t > \nu_z$, respectively, the trap frequency in the transversal direction is larger resulting in a smaller transversal length, such that the condensate is elongated in the longitudinal direction. This resembles a cigar-shaped form. On the other hand, for $\zeta > 1$, i.e. $\nu_t < \nu_z$, the condensate has a disk-shaped form.

With the equilibrium cloud widths γ_{t0} and γ_{z0} determined by Eqs. (4.3), we write

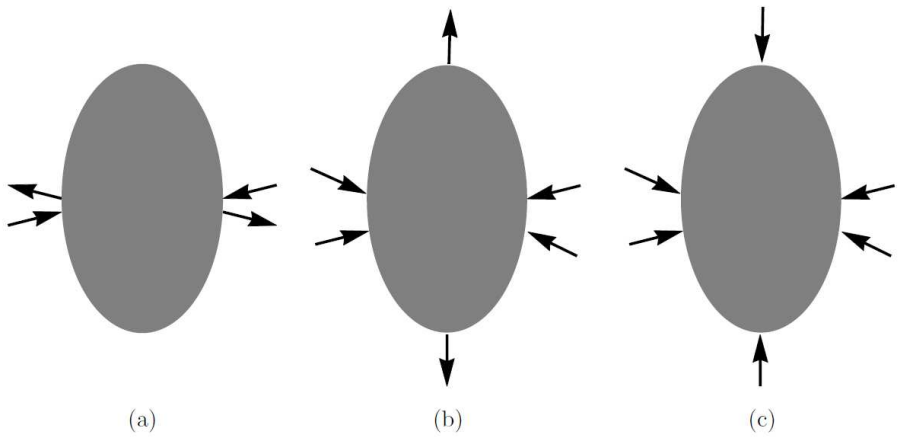

Figure 4.1.: Schematic plot of different collective modes for an axially symmetric BEC by [102]. (a) represents the radial quadrupole mode, (b) the out-of-phase quadrupole mode and (c) is the breathing mode.

down the Hessian matrix M given in general by Eq. (3.10). With the simplification of axial symmetry (4.1), this results in

$$M = \begin{pmatrix} 1 + \frac{3}{\gamma_{t0}^4} + \frac{2P}{\gamma_{t0}^4\gamma_{z0}} & \frac{P}{\gamma_{t0}^4\gamma_{z0}} & \frac{P}{\gamma_{t0}^3\gamma_{z0}^2} \\ \frac{P}{\gamma_{t0}^4\gamma_{z0}} & 1 + \frac{3}{\gamma_{t0}^4} + \frac{2P}{\gamma_{t0}^4\gamma_{z0}} & \frac{P}{\gamma_{t0}^3\gamma_{z0}^2} \\ \frac{P}{\gamma_{t0}^3\gamma_{z0}^2} & \frac{P}{\gamma_{t0}^3\gamma_{z0}^2} & \zeta^2 + \frac{3}{\gamma_{z0}^4} + \frac{2P}{\gamma_{t0}^2\gamma_{z0}^3} \end{pmatrix}. \tag{4.4}$$

As mentioned previously, the eigenvalues of this matrix lead to the collective frequencies, while the eigenvectors give insides of the collective modes. In Fig. 4.1 we show schematically the three possibilities for the low-lying collective modes: (a) the radial quadrupole mode in the axial plane, (b) the out-of-phase quadrupole mode and (c) the breathing mode.

4.1.2. Discussion

Here we discuss the numerical results for the equations (4.3) and the eigenvalues of the matrix in Eq. (4.4).

We start with the equilibrium cloud widths γ_{t0} and γ_{z0} in Eqs. (4.3), which we rewrite

as

$$\gamma_{t0}^5 - \gamma_{t0} - P\frac{\gamma_{t0}}{\gamma_{z0}} = 0, \tag{4.5a}$$

$$\zeta^2\gamma_{z0}^5 - \gamma_{z0} - P\frac{\gamma_{z0}^2}{\gamma_{t0}^2} = 0. \tag{4.5b}$$

Note that in Eq. (4.5) we have now as two additional parameter the trap-aspect ratio ζ and the contact interaction strength P, whose influence are examined separately. Due to the coupling between both cloud widths γ_{t0} and γ_{z0}, the two equations have to be solved simultaneously.

First, we vary the aspect ratio ζ. For this, we set the interaction strength P fixed to three examplary values $P = 0.2$, $P = 10$ and $P = 446$. The root-finding of Eqs. (4.5) is then performed simultaneously. This leads to the equilibrium cloud widths γ_{t0} in the transversal and γ_{z0} in the longitudinal direction. Both results as well as the fixed value for P are then used in the Hessian matrix M given in (4.4) and its eigenvalues are calculated. Similar to the previous chapter, the ratio Ω/ω between the collective frequencies and the trap frequency scale is then simply the square root of the eigenvalues. With the help of the corresponding eigenvectors, we finally assign the respective modes schematically shown in Fig. 4.1.

We present the results of the numerical evaluation in Fig. 4.2. As expected, the equilibrium cloud width γ_{z0} is larger than γ_{t0} in the cigar-shaped configuration with $\zeta < 1$, while in the disk-shaped case $\zeta > 1$ it is the opposite. Both widths cross each other at $\zeta = 1$, which corresponds to the spherical case treated in Sec. 3.1.3. The values for the equilibrium cloud width for each P at $\zeta = 1$ match the ones calculated for a spherical condensate. The further away from $\zeta = 1$, the greater the difference in the equilibrium widths becomes, as both the elongation and the confinement increase in the corresponding direction. The double logarithmic scale of Fig. 4.2 shows that both curves depend on an exponential law to the base ζ. In the following, we analytically verify this for two special cases. First, we investigate the Thomas-Fermi limit similar to Sec. 3.1.3. To do this, we neglect the kinetic contributions $-\gamma_{j0}$ in Eqs. (4.5). The set of equations

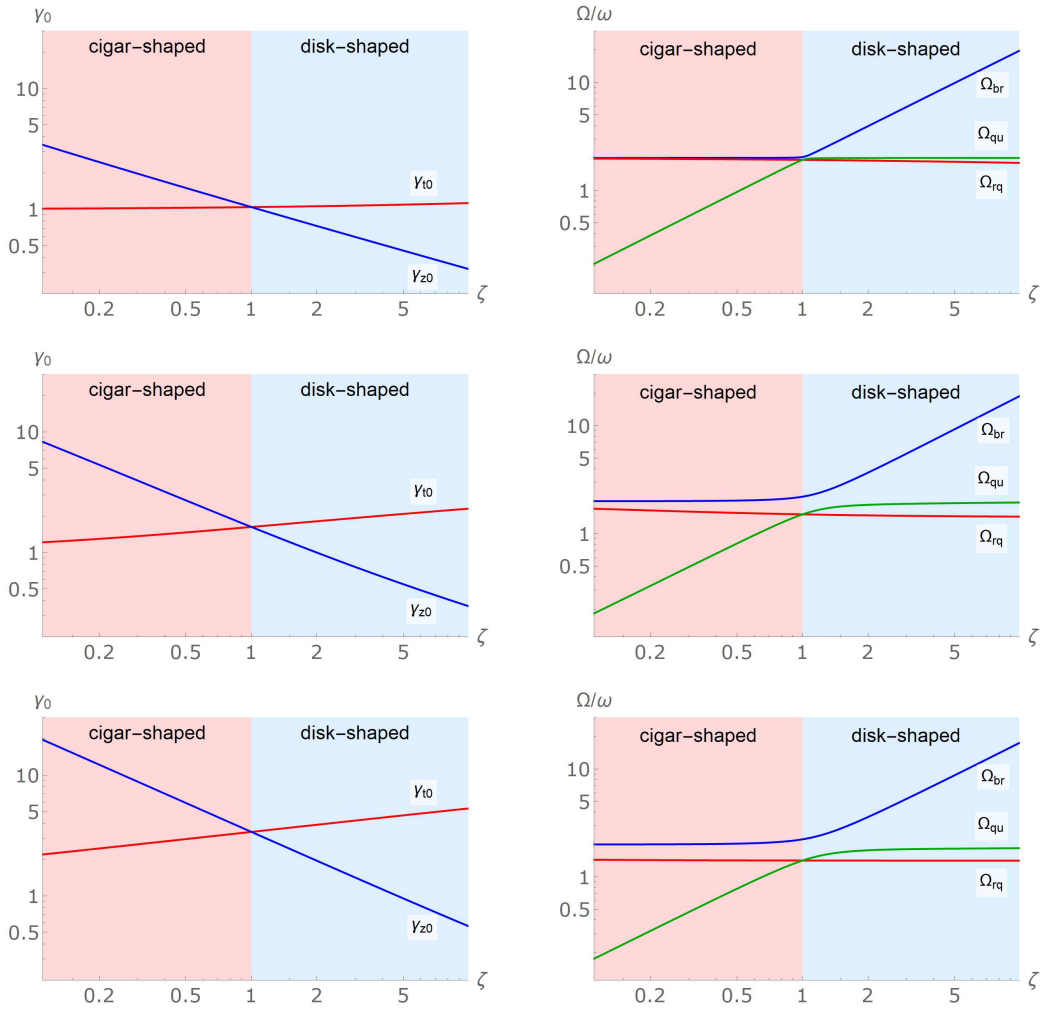

Figure 4.2.: Equilibrium widths γ_{t0} and γ_{z0} (left column), and collective frequencies Ω_{br}, Ω_{qu}, and Ω_{rq} (right column) depending on the aspect ratio ζ for an axially symmetric condensate with contact interaction. In the top row we set $P = 0.2$, in the middle $P = 10$, and at the bottom we have $P = 446$. The red shaded area $\zeta < 1$ represents cigar-shaped configurations, while the blue shaded area $\zeta > 1$ includes disk-shaped condensates. At $\zeta = 1$ we have a spherical condensate.

then reads

$$\gamma_{t0}^5 - P\frac{\gamma_{t0}}{\gamma_{z0}} = 0, \tag{4.6a}$$

$$\zeta^2\gamma_{z0}^5 - P\frac{\gamma_{z0}^2}{\gamma_{t0}^2} = 0. \tag{4.6b}$$

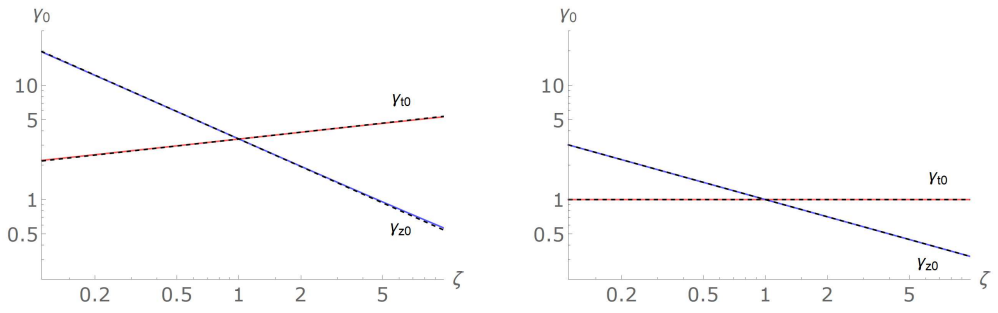

Figure 4.3.: Comparison between numerical (colored) and analytic results (black dashed) depending on the aspect ratio ζ: (left) numerical results for $P = 446$ and the Thomas-Fermi limit in Eq. (4.7), (right) numerical results for $P = 0$ and the non-interacting limit in Eq. (4.9).

According to Descartes' rule of sign, only one pair of solutions exists where both Gaussian widths γ_{t0} and γ_{z0} are positive. These are given by

$$\gamma_{t0}^5 = P\zeta, \quad \gamma_{z0}^5 = \frac{P}{\zeta^4}, \tag{4.7}$$

which is proven by simply putting the solutions into (4.6). The second limit describes a non-interacting axially symmetric condensate. Here, we set $P = 0$ in the Eqs. (4.5). This time the equations read

$$\gamma_{t0}^5 - \gamma_{t0} = 0, \tag{4.8a}$$

$$\zeta^2\gamma_{z0}^5 - \gamma_{0z} = 0 \tag{4.8b}$$

with the only physically possible solution

$$\gamma_{t0} = 1, \quad \gamma_{z0} = \frac{1}{\sqrt{\zeta}}. \tag{4.9}$$

In both cases we find that the dimensionless Gauss widths depend on a root of the aspect ratio. The corresponding exponent of ζ then determines the slope of the straight line in the double logarithmic plot. The comparison between the numerical results seen in Fig. 4.3 and the analytical formulas in Eqs. (4.7) and (4.9) show a highly convincing agreement. It seems likely that the slope transitions from one limiting case to the other as the interaction strength is increased.

Returning to Fig. 4.2, we furthermore see the collective frequencies depending on the aspect ratio on the right side of the figure. Again, at $\zeta = 1$ we have the spherical case, which is identical to the results in Fig. 3.2 for the corresponding value of P. Both frequencies Ω_{qu} and Ω_{rq} of the quadrupole modes, the out-of-phase and the radial mode respectively, are degenerated in this case, while the frequency of the breathing mode Ω_{br} is greater. This degeneracy is split up for $\zeta \neq 1$. Interestingly, the frequency of the radial quadrupole mode seems to be independent of the aspect ratio. As shown in the schematic overview of the possible modes in Fig. 4.1, the radial quadrupole mode is the only one oscillating in just two directions. This could be a possible explanation of this observation. For cigar-shaped condensates, Ω_{qu} is always the smallest frequency out of the three and decreasing furthermore for smaller aspect ratios. On the other hand, in disk-shaped condensates it becomes slightly greater than the frequency of the radial quadrupole mode, but converges asymptotically to a constant value. We also see that the collective frequency Ω_{br} of the breathing mode is always greater than the other two, but behaves like a mirrored version of the out-of-phase quadrupole mode: converging to a constant slightly above Ω_{rq} for $\zeta < 1$ and increasing for $\zeta > 1$.

In the second part, we take a closer look at the influence of the contact interaction strength P on the equilibrium widths and collective frequencies in both configurations $\zeta < 1$ and $\zeta > 1$. In order to achieve this, we choose the aspect ratios $\zeta = 3$ and $\zeta = 7$ for disk-shaped condensates and their reciprocal values for the cigar-shaped configurations, respectively. The interaction strength P is treated as a variable. The method itself is identical to the one described previously for a variable aspect ratio. We simultaneously solve the Eqs. (4.5) with fixed ζ and with the obtained equilibrium cloud widths γ_{t0} and γ_{z0} depending on the interaction strength we derive the collective frequencies as eigenvalues of the Hessian matrix M in (4.4).

We present the results of this calculation in Fig. 4.4 for cigar-shaped condensates and in Fig. 4.5 for disk-shaped BECs. The upper row of Fig. 4.4 shows the equilibrium cloud widths γ_{t0} and γ_{z0} and the collective frequencies Ω_{br}, Ω_{qu} and Ω_{rq} depending on the contact interaction strength P for an aspect ratio $\zeta = 1/3$, while the lower row shows the results for $\zeta = 1/7$. In Fig. 4.5 we have the disk-shaped counterparts with $\zeta = 3$ and $\zeta = 7$, respectively. For a better comparison, all figures are plotted within the same range of values.

The configuration is directly identified by the equilibrium cloud widths. For cigar shapes, the longitudinal direction γ_{z0} is always greater than the transversal direction

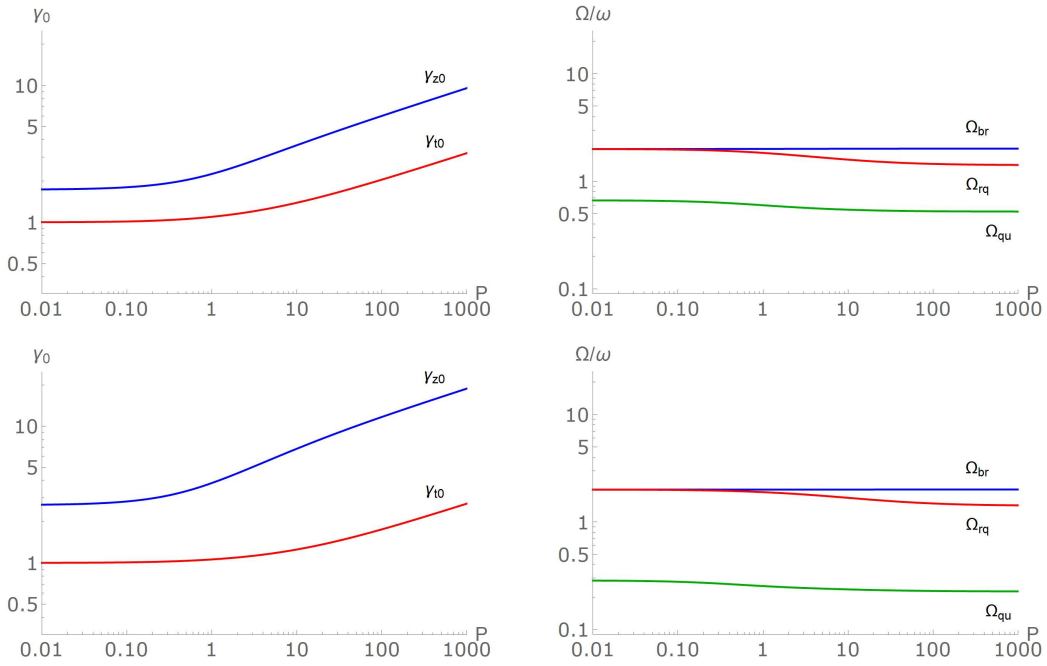

Figure 4.4.: Equilibrium widths γ_{t0} and γ_{z0} (left), and collective frequencies Ω_{br}, Ω_{qu}, and Ω_{rq} (right) depending on the contact interaction strength P for a cigar-shaped condensate. The upper two figures show a condensate with $\zeta = 1/3$ and the lower plots one with $\zeta = 1/7$. For a better comparison the scales match with Fig. 4.5.

γ_{t0}, while for the disk-shape condensates it is the other way around. In both cases, the equilibrium widths increase for higher contact interactions as the repulsion between two particles is greater, similar to the spherical case discussed in Sec. 3.1.3. The coupling term in Eqs. (4.5) vanishes in the limit $P \to 0$ and the first equation leads to the result $\gamma_{t0} = 1$, which matches the corresponding value in Fig. 4.4 and Fig. 4.5. Due to the aspect ratio ζ, the second equation in this example yields $\gamma_{z0} = \sqrt{1/3} \approx 0.58$ or $\gamma_{z0} = \sqrt{3} \approx 1.73$ as well as $\gamma_{z0} = \sqrt{1/7} \approx 0.38$ or $\gamma_{z0} = \sqrt{7} \approx 2.65$ for the two configurations, respectively. Comparison of these results coincides also with the ones shown in both figures. On the right column of Fig. 4.4 and 4.5 each plot shows the three collective frequencies. Again, the frequency of the breathing mode is the greatest and the frequency of the radial quadrupole mode is identical in all pictures, as mentioned in the description of Fig. 4.2. In accordance to Fig. 4.2, Ω_{qu} is significantly smaller in the cigar-shaped case and slightly greater than Ω_{rq} for disk-shaped condensates. The presented results here coincide with similar calculations in Ref. [99], where the collective

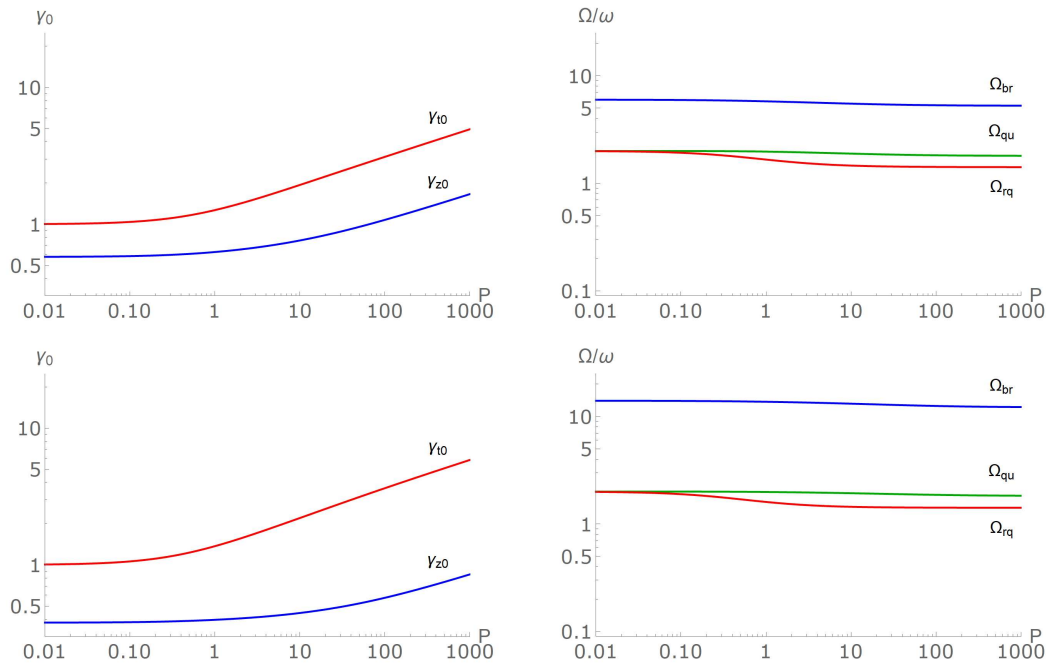

Figure 4.5.: Equilibrium widths γ_{t0} and γ_{z0} (left), and collective frequencies Ω_{br}, Ω_{qu}, and Ω_{rq} (right) depending on the contact interaction strength P for a disk-shaped condensate. For the upper two row we choose $\zeta = 3$ and for the lower figures $\zeta = 7$. For a better comparison the scales match with Fig. 4.4.

frequencies in an axially symmetric condensate are discussed.

4.2. Newtonian interaction

In this section we now consider the Newtonian interaction in an axially symmetric condensate. The method follows the steps of Sec. 3.2, but we have to evaluate the functions $\partial_{\gamma_j} I_{\mathrm{N}}$ in Eqs. (3.38) for the equilibrium cloud widths and $\partial^2_{\gamma_j} I_{\mathrm{N}}$ in (3.39a) as well as $\partial_{\gamma_j}\partial_{\gamma_k} I_{\mathrm{N}}$, see (3.39b) for the Hessian matrix now in axial symmetry (4.1). After this, we present the numerical calculations and the dependencies of the equilibrium widths and the collective frequencies on the gravitational interaction strength as well as the trap-aspect ratio.

4.2.1. Collective modes

In Ch. 2 we already discussed the general form of both the differential equation, see Eq. (2.34) and the Hessian matrix (2.42) depending on the Lagrangian of an arbitrary two-particle interaction. Furthermore, we treated the Fourier transformation of the Newtonian potential (1.6) and the Lagrangian with Newtonian interaction in detail in Sec. 3.2.1. In this context, we defined the integral I_{N} in Eq. (3.37) and its first derivative (3.38) and the second derivatives (3.39a) and (3.39b) independent of the symmetry of the system. Based on these equations, we now assume axial symmetry given in (4.1) and solve the appearing integrals. After that, we take a look at the spherical limit to verify our results. Finally, at the end of this section the numerical calculations are discussed. As the calculations are quite lengthy, although straightforward, we only present the most important steps here. A detailed solution especially for the integrals can be found in Appendix C.1.

Due to the axial symmetry, we now have to deal with two separate Gauss widths, γ_t and γ_z, as seen in the previous section. The problem is approached as usual by derivation of the differential equations for both Gauss widths. As already mentioned, we need to solve the first derivative of the integral I_{N}, which is generally given by (3.38). In axial symmetry (4.1) we choose cylindrical coordinates

$$\kappa_x = \kappa_\rho \cos\varphi, \quad \kappa_y = \kappa_\rho \sin\varphi, \quad \kappa_z = \kappa_z, \tag{4.10}$$

thus the right-hand side of the general form (3.38) gives

$$J_{\mathrm{N}}^{(j)} = -\gamma_j \int_{-\infty}^{\infty} \mathrm{d}\kappa_z \left(\int_0^{\infty} \mathrm{d}\kappa_\rho \int_0^{2\pi} \mathrm{d}\varphi \; \kappa_\rho \frac{\kappa_j^2}{\kappa_\rho^2 + \kappa_z^2} \exp\left\{ -\frac{1}{2}\gamma_t^2 \kappa_\rho^2 \right\} \right) \exp\left\{ -\frac{1}{2}\gamma_z^2 \kappa_z^2 \right\}. \tag{4.11}$$

As described in App. C.1 for all j, we simplify the integrals over κ_ρ in the brackets to

$$\int_0^{\infty} \mathrm{d}\kappa_\rho \; \frac{\kappa_\rho}{\kappa_\rho^2 + \kappa_z^2} \exp\left\{ -\frac{1}{2}\gamma_t^2 \kappa_\rho^2 \right\} = \frac{1}{2}\Gamma\left(0, \xi^2\right) \mathrm{e}^{\xi^2}, \tag{4.12}$$

where we introduce the incomplete gamma function $\Gamma(0, x)$ and define as a short-hand

notation

$$\xi^2 = \frac{1}{2}\gamma_t^2\kappa_z^2. \tag{4.13}$$

The integration over κ_z then leads to the definition

$$K_{\mathrm{N}} = \frac{1}{2}\int_{-\infty}^{\infty} \mathrm{d}\kappa_z\, \Gamma\left(0, \xi^2\right) \mathrm{e}^{\xi^2} \exp\left\{-\frac{1}{2}\gamma_z^2\kappa_z^2\right\}. \tag{4.14}$$

An integration yields

$$K_{\mathrm{N}} = \sqrt{2\pi}\frac{1}{\gamma_t}\frac{\operatorname{arcsinh}\sqrt{\frac{\gamma_z^2}{\gamma_t^2}-1}}{\sqrt{\frac{\gamma_z^2}{\gamma_t^2}-1}}. \tag{4.15}$$

For the sake of readability, the explicit but lengthy expressions for the derivations of K_{N} are omitted. Instead, we write the functions $J_{\mathrm{N}}^{(j)}$ down as formally depending on, for example, $\partial_{\gamma_t} K_{\mathrm{N}}$.

Having derived all the necessary components by now, we now write down the differential equations (2.34) in axial symmetry. Similar to the previous section, we get a set of two equations

$$\text{i)}\quad \ddot{\gamma}_t = -\gamma_t + \frac{1}{\gamma_t^3} + \frac{P}{\gamma_t^3\gamma_z} + \frac{3Q}{2\sqrt{2\pi}}\,\partial_{\gamma_t} K_{\mathrm{N}}, \tag{4.16a}$$

$$\text{ii)}\quad \ddot{\gamma}_z = -\zeta^2\gamma_z + \frac{1}{\gamma_z^3} + \frac{P}{\gamma_t^2\gamma_z^2} + \frac{3Q}{\sqrt{2\pi}}\,\partial_{\gamma_z} K_{\mathrm{N}}. \tag{4.16b}$$

Note that the derivatives in the last part differ: in the first equation we differentiate with respect to the axial Gaussian width γ_t while for the second equation it is γ_z.

The steady state is determined according to the usual procedure so that

$$\text{i)}\quad \gamma_{t0}^5 - \gamma_{t0} - P\frac{\gamma_{t0}}{\gamma_{z0}} - \gamma_{t0}^4\frac{3Q}{2\sqrt{2\pi}}\;\partial_{\gamma_t} K_{\mathrm{N}}\big|_{\substack{\gamma_t=\gamma_{t0}\\ \gamma_z=\gamma_{z0}}} = 0, \tag{4.17a}$$

$$\text{ii)}\quad \zeta^2\gamma_{z0}^5 - \gamma_{z0} - P\frac{\gamma_{z0}^2}{\gamma_{t0}^2} - \gamma_{z0}^4\frac{3Q}{\sqrt{2\pi}}\;\partial_{\gamma_z} K_{\mathrm{N}}\big|_{\substack{\gamma_t=\gamma_{t0}\\ \gamma_z=\gamma_{z0}}} = 0. \tag{4.17b}$$

Solving both equations simultaneously leads to the equilibrium cloud widths in both directions.

In order to determine the collective frequencies in axially symmetric condensates, we

have to derive an expression for the Hessian matrix M. We already know from Sec. 3.2 that the corrections to the elements of M due to the Newtonian interaction depend on the second derivatives of the integral I_{N} given by Eq. (3.39a) for the diagonal elements and Eq. (3.39b) for the off-diagonal elements. In axial symmetry, the right-hand side of (3.39a) then reads

$$J_{\mathrm{N}}^{(jj)} = \int_{-\infty}^{\infty} \mathrm{d}\kappa_z \int_0^{\infty} \mathrm{d}\kappa_\rho \int_0^{2\pi} \mathrm{d}\varphi\ \kappa_\rho \frac{\left(\gamma_j^2\kappa_j^4 - \kappa_j^2\right)}{\kappa_\rho^2 + \kappa_z^2} \exp\left\{-\frac{1}{2}\gamma_t^2\kappa_\rho^2\right\} \exp\left\{-\frac{1}{2}\gamma_z^2\kappa_z^2\right\} \tag{4.18}$$

and the right-hand side of (3.39b) becomes

$$J_{\mathrm{N}}^{(jk)} = \gamma_j\gamma_k \int_{-\infty}^{\infty} \mathrm{d}\kappa_z \int_0^{\infty} \mathrm{d}\kappa_\rho \int_0^{2\pi} \mathrm{d}\varphi\ \kappa_\rho \frac{\kappa_j^2\kappa_k^2}{\kappa_\rho^2 + \kappa_z^2} \exp\left\{-\frac{1}{2}\gamma_t^2\kappa_\rho^2\right\} \exp\left\{-\frac{1}{2}\gamma_z^2\kappa_z^2\right\}. \tag{4.19}$$

Once more, we express the integrals in terms of the function K_{N} given by (4.15) and insert this into the general form of the Hessian matrix M in (2.42). This then leads according to Appendix C.1 to the diagonal elements due to the Newtonian interaction

$$M_{\mathrm{N}}^{(xx)} = M_{\mathrm{N}}^{(yy)} = -\frac{3Q}{2\sqrt{2\pi}} \left[\frac{3}{4}\gamma_t\, \partial_{\gamma_t}\left(\frac{1}{\gamma_t}\, \partial_{\gamma_t} K_{\mathrm{N}}\right) + \frac{1}{\gamma_t}\, \partial_{\gamma_t} K_{\mathrm{N}}\right]\Bigg|_{\substack{\gamma_t=\gamma_{t0}\\ \gamma_z=\gamma_{z0}}}, \tag{4.20a}$$

$$M_{\mathrm{N}}^{(zz)} = -\frac{3Q}{\sqrt{2\pi}} \left[\gamma_z\, \partial_{\gamma_z}\left(\frac{1}{\gamma_z}\, \partial_{\gamma_z} K_{\mathrm{N}}\right) + \frac{1}{\gamma_z}\, \partial_{\gamma_z} K_{\mathrm{N}}\right]\Bigg|_{\substack{\gamma_t=\gamma_{t0}\\ \gamma_z=\gamma_{z0}}} \tag{4.20b}$$

as well as the corrections for the off-diagonal elements

$$M_{\mathrm{N}}^{(xy)} = -\frac{3Q}{8\sqrt{2\pi}} \left[\gamma_t\, \partial_{\gamma_t}\left(\frac{1}{\gamma_t}\, \partial_{\gamma_t} K_{\mathrm{N}}\right)\right]\Bigg|_{\substack{\gamma_t=\gamma_{t0}\\ \gamma_z=\gamma_{z0}}}, \tag{4.21a}$$

$$M_{\mathrm{N}}^{(xz)} = M_{\mathrm{N}}^{(yz)} = -\frac{3Q}{2\sqrt{2\pi}} \left[\partial_{\gamma_t}\partial_{\gamma_z} K_{\mathrm{N}}\right]\Bigg|_{\substack{\gamma_t=\gamma_{t0}\\ \gamma_z=\gamma_{z0}}}. \tag{4.21b}$$

These corrections due to the Newtonian interaction must be added to the corresponding elements given in the Hessian matrix (4.4), which only includes the contact interaction in axial symmetry.

At the end of this section, as usual, we briefly mention the spherical limit of our

obtained results here. It is noteworthy that both the differential equations (4.16) and the elements of the Hessian matrix (4.20) and (4.21) depend on the function K_N. The spherical limit $\gamma_t \to \gamma_z$ of K_N in the explicit form of Eq. (4.15) is quite similar to the well known $\mathrm{sinc}(x)$ function

$$\lim_{\gamma_t \to \gamma_z} \left[\frac{\mathrm{arcsinh}\sqrt{\frac{\gamma_z^2}{\gamma_t^2} - 1}}{\sqrt{\frac{\gamma_z^2}{\gamma_t^2} - 1}} \right] = 1. \tag{4.22}$$

A graphic of the function $x^{-1}\mathrm{arcsinh}(x)$ is provided in the Appendix C.1 in Fig. C.1. The value at $x = 0$ represents the limit above.

As a consequence, we obtain

$$\lim_{\gamma_t \to \gamma_z} K_\mathrm{N} = \frac{\sqrt{2\pi}}{\gamma_z}, \tag{4.23}$$

which coincides with the result in the spherical case, see also Eq. (B.9) in Appendix B.2. Note that the additional factor 2 emerges from different lower integral limit for κ_z. In the spherical case it is simply zero, while in the axially symmetric case we start the integration at $-\infty$.

For the limits of the differential equations, we first have to calculate the derivative of K_N with respect to γ_t. This leads to the three terms

$$\partial_{\gamma_t} K_\mathrm{N} = -\frac{\gamma_z^2}{\gamma_t^2}\sqrt{\frac{\gamma_t^2}{\gamma_z^2}}\frac{1}{\frac{\gamma_z^2}{\gamma_t^2} - 1} + \frac{\gamma_z^2}{\gamma_t^2}\frac{1}{\frac{\gamma_z^2}{\gamma_t^2} - 1}\frac{\mathrm{arcsinh}\sqrt{\frac{\gamma_z^2}{\gamma_t^2} - 1}}{\sqrt{\frac{\gamma_z^2}{\gamma_t^2} - 1}} - \frac{1}{\gamma_t^2}\frac{\mathrm{arcsinh}\sqrt{\frac{\gamma_z^2}{\gamma_t^2} - 1}}{\sqrt{\frac{\gamma_z^2}{\gamma_t^2} - 1}}. \tag{4.24}$$

Taking the limit $\gamma_t \to \gamma_z$ results in the correct differential equation for spherically symmetric condensates as in Eq. (3.47). In case of the second ODE it should be noted that $\zeta = 1$. Similar, although lengthy, we can calculate the second derivatives of K_N and verify the correct limits of the elements of the Hessian matrix M.

4.2.2. Discussion

After deriving the analytical expressions for the equilibrium cloud widths γ_{t0} and γ_{z0} given in Eq. (4.17), as well as for the Hessian matrix with the elements (4.20) and (4.21), it is now time to evaluate them numerically. As in Sec. 4.1.2, we can change various

parameters, so we split the discussion in two parts. First, we investigate the influence of the aspect ratio ζ while holding the gravitational interaction strength Q constant. After that we focus on the dependency of Q for specific values of ζ. For both calculations we fix $P = 446$ according to Sec. 3.1.3. Then we start searching for the equilibrium cloud widths by evaluating both equations in (4.17) simultaneously. Again, the results are used in the Hessian matrix of which we calculate the eigenvalues. Analogue to the previous section the ratio of the collective frequencies and the trap frequency scale Ω/ω is determined by the square root of the eigenvalues and the corresponding eigenvectors yields the collective modes.

In Fig. 4.6 the equilibrium widths γ_{t0} and γ_{z0} and the collective frequencies Ω_{br}, Ω_{rq} and Ω_{qu} depending on the aspect ratio ζ behave in a similar way as in Fig. 4.2. Again both configurations cigar-shaped and disk-shaped are represented in a compact form. For the gravitational interaction strength Q we chose a realistic value $Q = 4.1 \cdot 10^{-19}$ as derived in Sec. 3.2.3 as well as $Q = 10$ and $Q = 50$ for strong gravitational interaction. The black dashed lines in Fig. 4.6 are the results of the previous section for $P = 446$ and serve as a reference.

As expected for a realistic value of Q no changes are visible as the gravitational interaction is just too small. Similar results were already found in 3.2.3 for the spherical case. Changing the form of the condensate by the aspect ratio does not help in that case either. For $Q = 10$ slight differences occur and noticeably in case of the equilibrium widths the effect of gravity seems to be amplified for more elongated condensates compared to the spherical case $\zeta = 1$. Overall the widths become smaller due to the increasing attractive gravitational interaction while the collective frequencies become larger. As the interaction strength Q gets larger the exponential law discussed in the end of Sec. 4.1.2 breaks up and the curves are no more straight lines in the double logarithmic plot. In analogy, the graphs of the collective frequencies gets more curvy, too, such that even the frequency of the radial quadrupole mode decreases in the disk-shaped configuration with $\zeta = 10$. In all pictures the results of Sec. 3.2.3 like the degeneracy of both quadrupole frequencies are successfully recovered for $\zeta = 1$.

In the second part we show the dependency of the clouds widths and collective frequencies on the gravitational interaction strength Q itself. For this we choose a fixed values for ζ, in our examples again $\zeta = 3$ and $\zeta = 7$ for disk-shaped condensates and their reciprocal values for the cigar-shaped configuration.

The results are shown in Fig. 4.7 for cigar-shaped condensates with $\zeta < 1$ and in

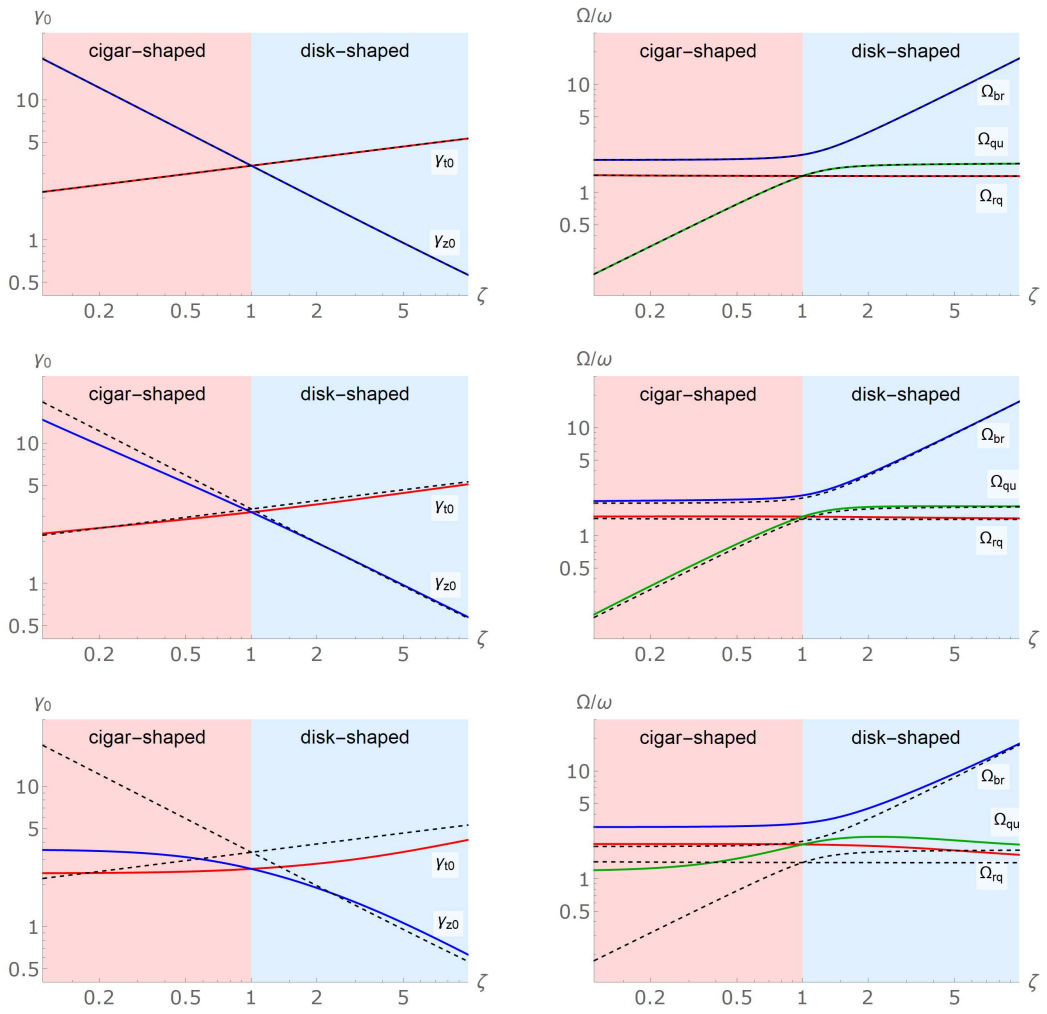

Figure 4.6.: Equilibrium widths γ_{t0} and γ_{z0} (left), and collective frequencies Ω_{br}, Ω_{qu}, and Ω_{rq} (right) depending on the aspect ratio ζ for an axially symmetric condensate with Newtonian interaction Q. The upper two figures show the results for $Q = 4.1 \cdot 10^{-19}$, in the middle we have $Q = 10$, and at the bottom $Q = 50$. The black dashed lines indicate the results for pure contact interaction with $P = 446$, see Fig. 4.2.

Fig. 4.8 for disk-shaped condensates with $\zeta > 1$. As in Sec. 4.1.2 the configuration can be directly identified via the relation between both equilibrium widths. In principle, the trends are analogue to the results of the spherical case in Sec. 3.2.3. For small Q the equilibrium cloud widths and the collective frequencies are constant meaning the gravitational influence is not visible. On the other side, for $Q > 10$ the increased attractive interaction leads to a rapid decrease of the widths and an increase of all frequencies. It

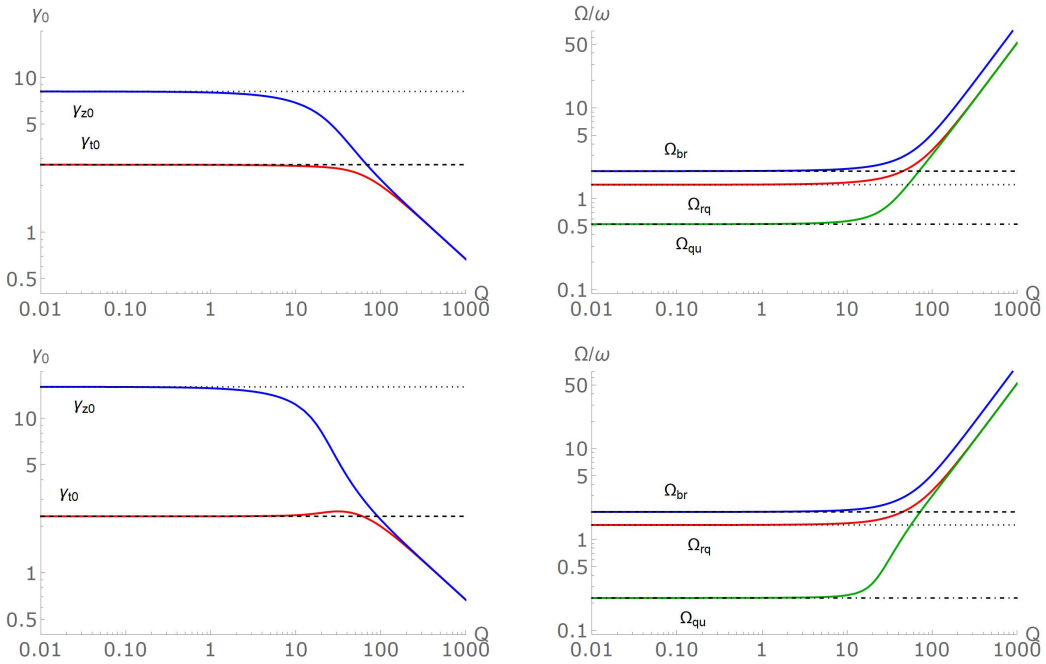

Figure 4.7.: Equilibrium widths γ_{t0} and γ_{z0} (left) and collective frequencies Ω_{br}, Ω_{qu}, and Ω_{rq} (right) depending on the gravitational interaction strength Q for a cigar-shaped condensate. For the upper two plots we choose $\zeta = 1/3$ and for the lower figures $\zeta = 1/7$. The black dashed, dotted, and dash-dotted lines show the corresponding quantity for $Q = 0$

is remarkable that for even higher values $Q > 100$ both widths and both quadrupole frequencies coincide indicating that the condensate transitions to a spherical form. The reason for this is the property of Newtonian gravity being a conservative force which at some point surpasses the repulsive contact interaction. Furthermore, for larger elongations $\zeta = 1/7$ and $\zeta = 7$ in particular one notices a global maximum at $Q \approx 100$ for the lower equilibrium cloud width γ_{t0} or γ_{z0}, respectively. We assume that the cause of this is a density difference in the longitudinal and transversal direction. In the example of the cigar-shaped condensate there are on average more particles in the longitudinal direction than in the stronger confined transversal direction. The gravitational selfinteraction of each individual particle then results in a larger attractive interaction along the z-direction. As a consequence gravity is pulling the condensate together more in said direction. The higher density is then compensated by increasing the size in the transversal direction prior to converging to the spherical limit. This would also explain why the maximum in case of a disk-shaped BEC is larger as the z-direction has to compensate

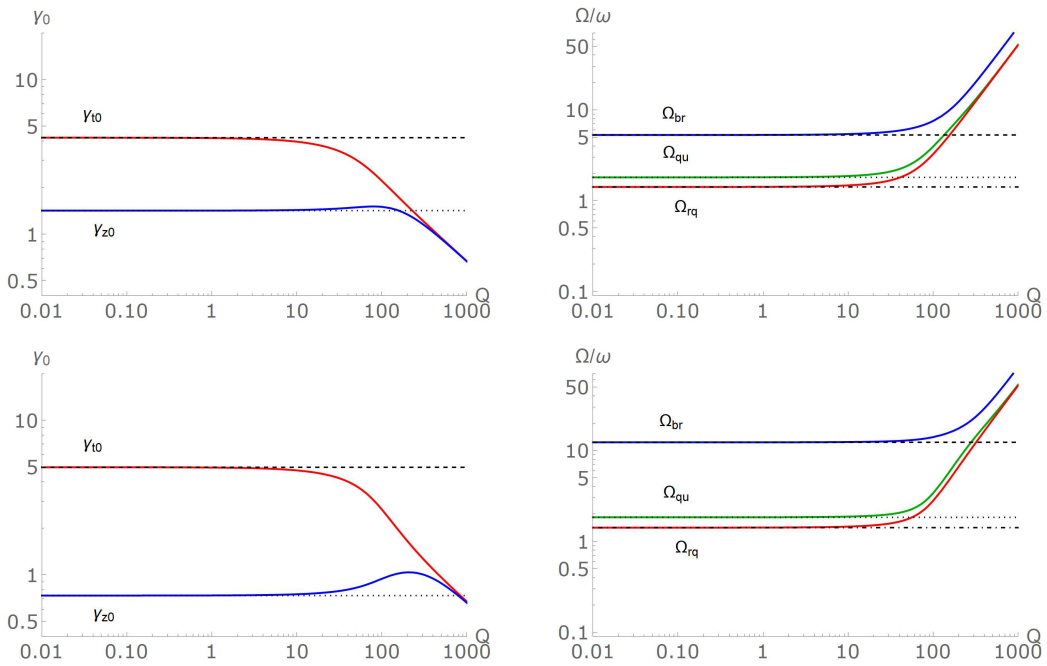

Figure 4.8.: Equilibrium widths γ_{t0} and γ_{z0} (left) and collective frequencies Ω_{br}, Ω_{qu}, and Ω_{rq} (right) depending on the gravitational interaction strength Q for a disk-shaped condensate. For the upper two plots we choose $\zeta = 3$ and for the lower figures $\zeta = 7$. The black dashed, dotted, and dash-dotted lines show the corresponding quantity for $Q = 0$

the density in two dimensions instead of just one.

Additionally, comparing both figures Fig. 4.7 and Fig. 4.8 we see that the equilibrium widths and the collective frequencies of both quadrupole modes are switched. This is in accordance to previous results of this chapter. For small values of Q also the gaps between the widths and between the frequencies are increased for larger elongations which is clearly visible in Fig. 4.6. Furthermore, the individual values of the plateaus for the widths and frequencies for small Q are identical to the values at $P = 446$ in Fig. 4.4 and Fig. 4.5, respectively.

In particular, the widths can be analytically verified via the Thomas-Fermi approximation shown in Eq. (4.7). In the cigar-shaped case with $\zeta = 1/3$ we get $\gamma_{t0} = \sqrt[5]{446 \cdot 1/3} \approx 2.72$ and $\gamma_{z0} = \sqrt[5]{446 \cdot (1/3)^{-4}} \approx 8.16$ or $\gamma_{t0} \approx 2.30$ and $\gamma_{z0} \approx 16.07$ for $\zeta = 1/7$. Analogously, in the disk-shaped configuration with $\zeta = 3$ the equilibrium widths yield $\gamma_{t0} \approx 4.22$ and $\gamma_{z0} \approx 1.41$ while $\gamma_{t0} \approx 5.00$ and $\gamma_{z0} \approx 0.71$ for $\zeta = 7$. These results also reflect that for small Q the gap between the width increases with the elongation of the

condensate. Unfortunately, this calculation is not possible for the collective frequencies as we do not have any analytic expression.

4.3. Yukawa interaction

This section is dedicated to the Yukawa-like interaction within axially symmetric condensates. In Sec. 3.3 where we already mentioned the general expressions for the first and second derivatives of I_{Yuk}, see Eqs. (3.70), (3.71a) and (3.71b) without any assumption on the symmetry of the condensate. Based on these expressions we follow the steps of the previous section. In the end we show contourplots for the equilibrium cloud widths as well as the collective frequencies.

4.3.1. Collective modes

We begin with Eq. (3.70) and apply axial symmetry given by (4.1). Using the cylindrical coordinates in (4.10) we define analogue to the Newtonian case

$$J_{\mathrm{Yuk}}^{(j)} = -\gamma_j \int_{-\infty}^{\infty} \mathrm{d}\kappa_z \int_0^{\infty} \mathrm{d}\kappa_\rho \int_0^{2\pi} \mathrm{d}\varphi \frac{\alpha \kappa_\rho \kappa_j^2}{\kappa_\rho^2 + \kappa_z^2 + \bar{\lambda}^{-2}} \exp\left\{-\frac{1}{2}\gamma_t^2 \kappa_\rho^2\right\} \exp\left\{-\frac{1}{2}\gamma_z^2 \kappa_z^2\right\}. \tag{4.25}$$

Here we immediately notice a fundamental difference caused by the finite dimensionless effective range $\bar{\lambda}$. In Appendix C.2 we explicitly show that we can still formally follow the same calculations by using the slightly modified definition

$$\xi'^2 = \frac{1}{2}\gamma_t^2 \left(\kappa_z^2 + \bar{\lambda}^{-2}\right) \tag{4.26}$$

instead of (4.13) in the Newtonian case. Analogously, we introduce

$$K_{\mathrm{Yuk}} = \frac{1}{2} \int_{-\infty}^{\infty} \mathrm{d}\kappa_z \, \Gamma\left(0, \xi'^2\right) \mathrm{e}^{\xi'^2} \exp\left\{-\frac{1}{2}\gamma_z^2 \kappa_z^2\right\} \tag{4.27}$$

now depending on ξ'. Unfortunately, due to the finite range we are not able to get an analytic solution for the integral, thus we will simply stick to the formal definition in Eq. (4.27).

The set of differential equations including the contact, the Newtonian and the Yukawa

interaction are

$$\text{i)}\quad \ddot{\gamma}_t = -\gamma_t + \frac{1}{\gamma_t^3} + \frac{P}{\gamma_t^3\gamma_z} + \frac{3Q}{2\sqrt{2\pi}}\,\partial_{\gamma_t} K_\mathrm{N} + \alpha\frac{3Q}{2\sqrt{2\pi}}\,\partial_{\gamma_t} K_\mathrm{Yuk}, \tag{4.28a}$$

$$\text{ii)}\quad \ddot{\gamma}_z = -\zeta^2\gamma_z + \frac{1}{\gamma_z^3} + \frac{P}{\gamma_t^2\gamma_z^2} + \frac{3Q}{\sqrt{2\pi}}\,\partial_{\gamma_z} K_\mathrm{N} + \alpha\frac{3Q}{\sqrt{2\pi}}\,\partial_{\gamma_z} K_\mathrm{Yuk}. \tag{4.28b}$$

With the help of the functions K_N from Eq. (4.15) and K_Yuk from (4.27) we can write down both differential equations with a very similar structure although we have no analytic expression for the Yukawa corrections.

Again, the steady state is thus given by

$$\begin{aligned}\text{i)}\quad &\gamma_{t0}^5 - \gamma_{t0} - P\frac{\gamma_{t0}}{\gamma_{z0}} - \gamma_{t0}^4\frac{3Q}{2\sqrt{2\pi}}\;\partial_{\gamma_t} K_\mathrm{N}\big|_{\substack{\gamma_t=\gamma_{t0}\\ \gamma_z=\gamma_{z0}}} \\ &\qquad - \gamma_{t0}^4\,\alpha\frac{3Q}{2\sqrt{2\pi}}\;\partial_{\gamma_t} K_\mathrm{Yuk}\big|_{\substack{\gamma_t=\gamma_{t0}\\ \gamma_z=\gamma_{z0}}} = 0, \end{aligned}\tag{4.29a}$$

$$\begin{aligned}\text{ii)}\quad &\zeta^2\gamma_{z0}^5 - \gamma_{z0} - P\frac{\gamma_{z0}^2}{\gamma_{t0}^2} - \gamma_{z0}^4\frac{3Q}{\sqrt{2\pi}}\;\partial_{\gamma_z} K_\mathrm{N}\big|_{\substack{\gamma_t=\gamma_{t0}\\ \gamma_z=\gamma_{z0}}} \\ &\qquad - \gamma_{z0}^4\,\alpha\frac{3Q}{\sqrt{2\pi}}\;\partial_{\gamma_z} K_\mathrm{Yuk}\big|_{\substack{\gamma_t=\gamma_{t0}\\ \gamma_z=\gamma_{z0}}} = 0, \end{aligned}\tag{4.29b}$$

which determines the equilibrium cloud widths γ_{t0} and γ_{z0}.

Next, we determine the Hessian matrix M. For the Yukawa corrections to the diagonal elements the general formula is Eq. (3.71a) which becomes in axial symmetry

$$J_\mathrm{Yuk}^{(jj)} = \int_{-\infty}^{\infty}\mathrm{d}\kappa_z\int_0^{\infty}\mathrm{d}\kappa_\rho\int_0^{2\pi}\mathrm{d}\varphi\;\frac{\kappa_\rho\left(\gamma_j^2\kappa_j^4-\kappa_j^2\right)}{\kappa_\rho^2+\kappa_z^2+\frac{1}{\lambda^2}}\exp\left\{-\frac{1}{2}\gamma_t^2\kappa_\rho^2\right\}\exp\left\{-\frac{1}{2}\gamma_z^2\kappa_z^2\right\}, \tag{4.30}$$

while the right-hand side of (3.71b) yields

$$J_\mathrm{Yuk}^{(jk)} = \gamma_j\gamma_k\int_{-\infty}^{\infty}\mathrm{d}\kappa_z\int_0^{\infty}\mathrm{d}\kappa_\rho\int_0^{2\pi}\mathrm{d}\varphi\;\frac{\kappa_\rho\kappa_j^2\kappa_k^2}{\kappa_\rho^2+\kappa_z^2+\frac{1}{\lambda^2}}\exp\left\{-\frac{1}{2}\gamma_t^2\kappa_\rho^2\right\}\exp\left\{-\frac{1}{2}\gamma_z^2\kappa_z^2\right\}. \tag{4.31}$$

With the function K_Yuk given by (4.27) the correction to the Hessian matrix then reads

$$M_{\mathrm{Yuk}}^{(xx)} = M_{\mathrm{Yuk}}^{(yy)} = -\alpha\frac{3Q}{2\sqrt{2\pi}}\left[\frac{3}{4}\gamma_t\,\partial_{\gamma_t}\left(\frac{1}{\gamma_t}\,\partial_{\gamma_t}K_{\mathrm{Yuk}}\right)+\frac{1}{\gamma_t}\,\partial_{\gamma_t}K_{\mathrm{Yuk}}\right]\Bigg|_{\substack{\gamma_t=\gamma_{t0}\\ \gamma_z=\gamma_{z0}}}, \tag{4.32a}$$

$$M_{\mathrm{Yuk}}^{(zz)} = -\alpha\frac{3Q}{\sqrt{2\pi}}\left[\gamma_z\,\partial_{\gamma_z}\left(\frac{1}{\gamma_z}\,\partial_{\gamma_z}K_{\mathrm{Yuk}}\right)+\frac{1}{\gamma_z}\,\partial_{\gamma_z}K_{\mathrm{Yuk}}\right]\Bigg|_{\substack{\gamma_t=\gamma_{t0}\\ \gamma_z=\gamma_{z0}}} \tag{4.32b}$$

and the corrections to the off-diagonal elements are

$$M_{\mathrm{Yuk}}^{(xy)} = -\alpha\frac{3Q}{8\sqrt{2\pi}}\left[\gamma_t\,\partial_{\gamma_t}\left(\frac{1}{\gamma_t}\,\partial_{\gamma_t}K_{\mathrm{Yuk}}\right)\right]\Bigg|_{\substack{\gamma_t=\gamma_{t0}\\ \gamma_z=\gamma_{z0}}}, \tag{4.33a}$$

$$M_{\mathrm{Yuk}}^{(xz)} = M_{\mathrm{Yuk}}^{(yz)} = -\alpha\frac{3Q}{2\sqrt{2\pi}}\left[\partial_{\gamma_t}\partial_{\gamma_z}K_{\mathrm{Yuk}}\right]\Bigg|_{\substack{\gamma_t=\gamma_{t0}\\ \gamma_z=\gamma_{z0}}}. \tag{4.33b}$$

Finally, we write down the complete Hessian matrix consisting the contact, Newtonian and Yukawa interaction in a axially symmetric condensate as

$$M = \begin{pmatrix} m_{xx} & m_{xy} & m_{xz} \\ m_{xy} & m_{xx} & m_{xz} \\ m_{xz} & m_{xz} & x_{zz} \end{pmatrix}. \tag{4.34}$$

The elements are then given by

$$\begin{aligned} m_{xx} = 1 + \frac{3}{\gamma_{t0}^4} + \frac{2P}{\gamma_{t0}^4\gamma_{z0}} - \frac{3Q}{2\sqrt{2\pi}}\left[\frac{3}{4}\gamma_t\,\partial_{\gamma_t}\left(\frac{1}{\gamma_t}\,\partial_{\gamma_t}K_{\mathrm{N}}\right)+\frac{1}{\gamma_t}\,\partial_{\gamma_t}K_{\mathrm{N}}\right]\Bigg|_{\substack{\gamma_t=\gamma_{t0}\\ \gamma_z=\gamma_{z0}}} \\ - \alpha\frac{3Q}{2\sqrt{2\pi}}\left[\frac{3}{4}\gamma_t\,\partial_{\gamma_t}\left(\frac{1}{\gamma_t}\,\partial_{\gamma_t}K_{\mathrm{Yuk}}\right)+\frac{1}{\gamma_t}\,\partial_{\gamma_t}K_{\mathrm{Yuk}}\right]\Bigg|_{\substack{\gamma_t=\gamma_{t0}\\ \gamma_z=\gamma_{z0}}}, \end{aligned} \tag{4.35}$$

$$m_{zz} = \zeta^2 + \frac{3}{\gamma_{z0}^4} + \frac{2P}{\gamma_{t0}^2\gamma_{z0}^3} - \frac{3Q}{\sqrt{2\pi}}\left[\gamma_z\,\partial_{\gamma_z}\left(\frac{1}{\gamma_z}\,\partial_{\gamma_z}K_{\mathrm{N}}\right) + \frac{1}{\gamma_z}\,\partial_{\gamma_z}K_{\mathrm{N}}\right]\Bigg|_{\substack{\gamma_t=\gamma_{t0}\\ \gamma_z=\gamma_{z0}}}$$
$$- \alpha\frac{3Q}{\sqrt{2\pi}}\left[\gamma_z\,\partial_{\gamma_z}\left(\frac{1}{\gamma_z}\,\partial_{\gamma_z}K_{\mathrm{Yuk}}\right) + \frac{1}{\gamma_z}\,\partial_{\gamma_z}K_{\mathrm{Yuk}}\right]\Bigg|_{\substack{\gamma_t=\gamma_{t0}\\ \gamma_z=\gamma_{z0}}}, \tag{4.36}$$

and

$$m_{xy} = \frac{P}{\gamma_{t0}^4\gamma_{z0}} - \frac{3Q}{8\sqrt{2\pi}}\left[\gamma_t\,\partial_{\gamma_t}\left(\frac{1}{\gamma_t}\,\partial_{\gamma_t}K_{\mathrm{N}}\right)\right]\Bigg|_{\substack{\gamma_t=\gamma_{t0}\\ \gamma_z=\gamma_{z0}}}$$
$$- \alpha\frac{3Q}{8\sqrt{2\pi}}\left[\gamma_t\,\partial_{\gamma_t}\left(\frac{1}{\gamma_t}\,\partial_{\gamma_t}K_{\mathrm{Yuk}}\right)\right]\Bigg|_{\substack{\gamma_t=\gamma_{t0}\\ \gamma_z=\gamma_{z0}}}, \tag{4.37}$$

$$m_{xz} = \frac{P}{\gamma_{t0}^3\gamma_{z0}^2} - \frac{3Q}{2\sqrt{2\pi}}\left[\partial_{\gamma_t}\partial_{\gamma_z}K_{\mathrm{N}}\right]\Bigg|_{\substack{\gamma_t=\gamma_{t0}\\ \gamma_z=\gamma_{z0}}} - \alpha\frac{3Q}{2\sqrt{2\pi}}\left[\partial_{\gamma_t}\partial_{\gamma_z}K_{\mathrm{Yuk}}\right]\Bigg|_{\substack{\gamma_t=\gamma_{t0}\\ \gamma_z=\gamma_{z0}}}, \tag{4.38}$$

where K_{N} is defined in Eq. (4.15) and K_{Yuk} by the integral form in Eq. (4.27). In particular, the dependency on the finite effective range $\bar{\lambda}$ is hidden in K_{Yuk}.

4.3.2. Discussion

In the end of this chapter we take a look into the numerical results for both cigar-shaped and disk-shaped condensates interacting via a Yukawa-like potential. Analogue to the previous section we choose for the aspect ratio of the trap frequency the values $\zeta = 1/3$ and $\zeta = 1/7$ for a cigar-shaped configuration as well as $\zeta = 3$ and $\zeta = 7$ in the disk-shaped case. For the contact interaction strength and the gravitational interaction strength we set $P = 446$ and $Q = 4.1 \cdot 10^{-19}$.

Following the same procedure, we first calculate the solutions of Eq. (4.29) which lead to the equilibrium cloud widths γ_{t0} and γ_{z0}. We insert the result into the Hessian matrix given by Eqs. (4.34)-(4.38) and derive the collective frequencies as eigenvalues of that matrix. Again, we get the Gauss widths A_{t0} and A_{z0} as well as the frequencies Ω_{br}, Ω_{qu} and Ω_{rq} in physical units with the help of a backwards transformation with the dimensionless variables (2.33) and (3.67). The final results are then shown as contourplots depending on the Yukawa parameters α and λ analogue to Sec. 3.3.3.

We present the results in Figs. 4.9, 4.10, 4.11 and 4.12 for $\zeta = 1/3$, $\zeta = 1/7$, $\zeta = 3$

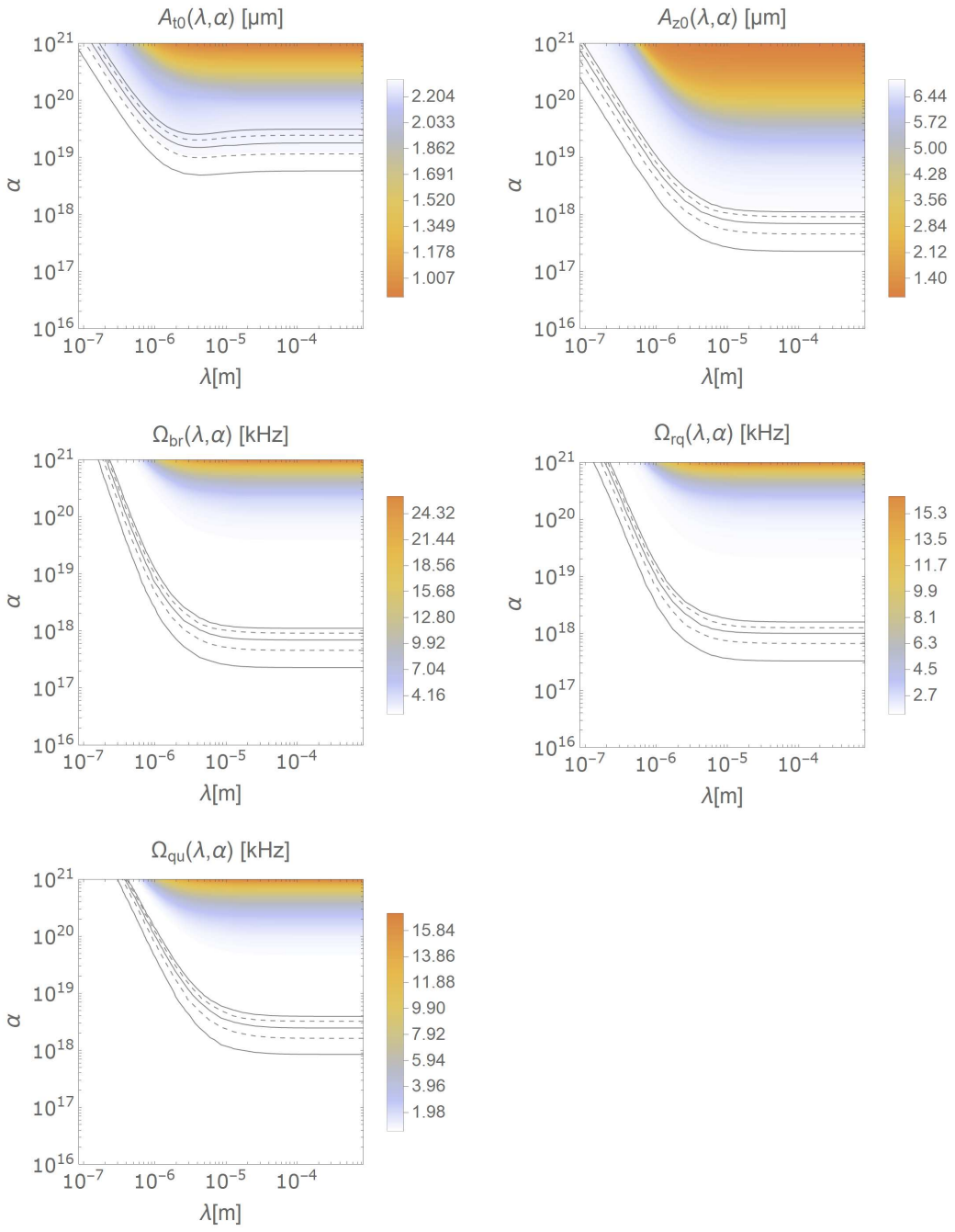

Figure 4.9.: Equilibrium cloud widths A_{t0} and A_{z0} and collective frequencies Ω_{br}, Ω_{rq}, and Ω_{qu} for a cigar-shaped condensate with Yukawa-like interaction and $\zeta = 1/3$. The black and black dashed lines indicate a difference of 0.01 μm to 0.05 μm or 1 Hz to 5 Hz, respectively, to the Newtonian case.

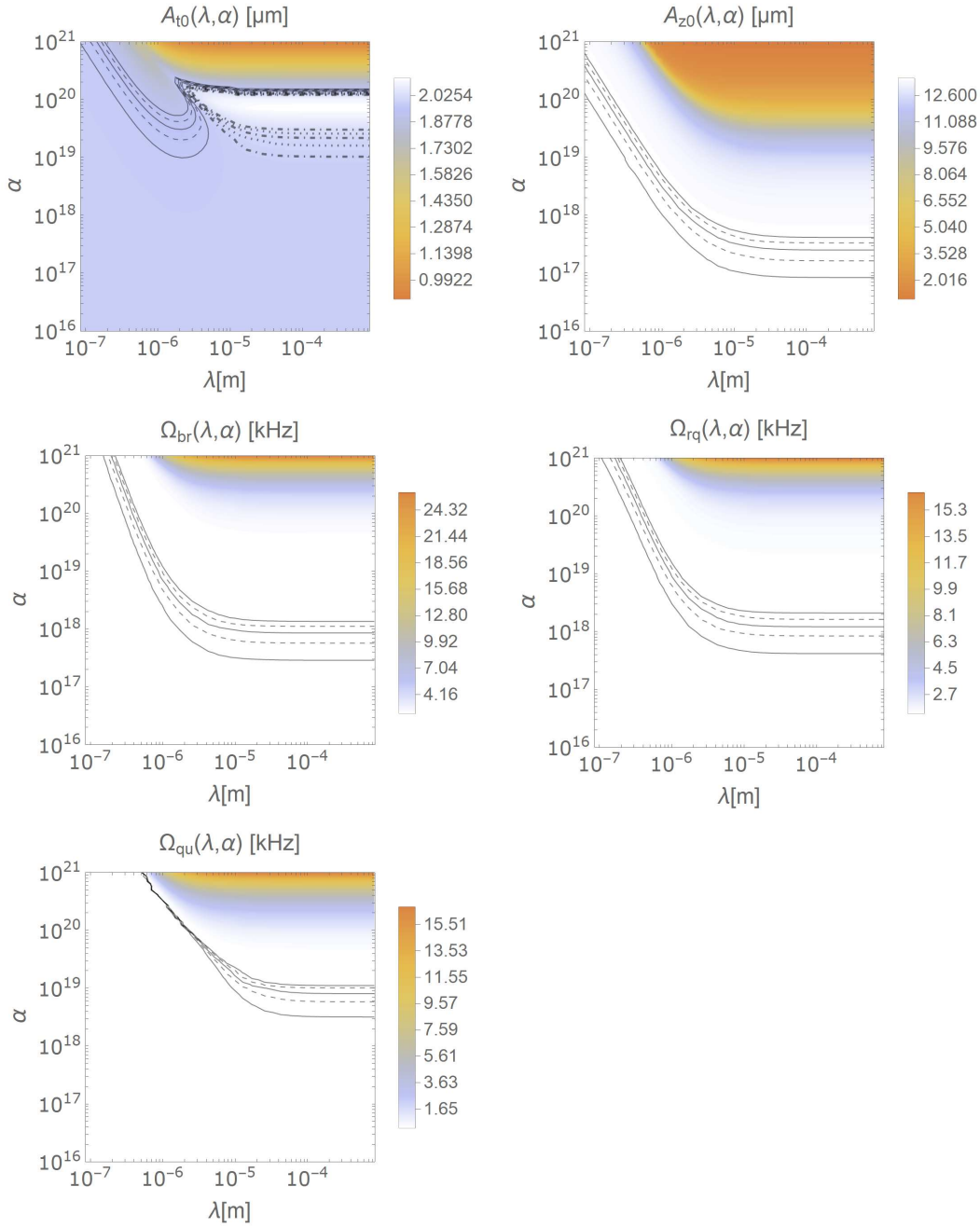

Figure 4.10.: Equilibrium cloud widths A_{t0} and A_{z0} and the collective frequencies Ω_{br}, Ω_{rq}, and Ω_{qu} for a cigar-shaped condensate with Yukawa-like interaction and $\zeta = 1/7$. In the first picture the black solid and dashed lines indicate a decrease of 0.01 μm to 0.05 μm and black dashed dotted and dotted lines represent an increase of 0.01 μm to 0.05 μm compared to the Newtonian case. In case of the frequencies, the differences are 1 Hz to 5 Hz.

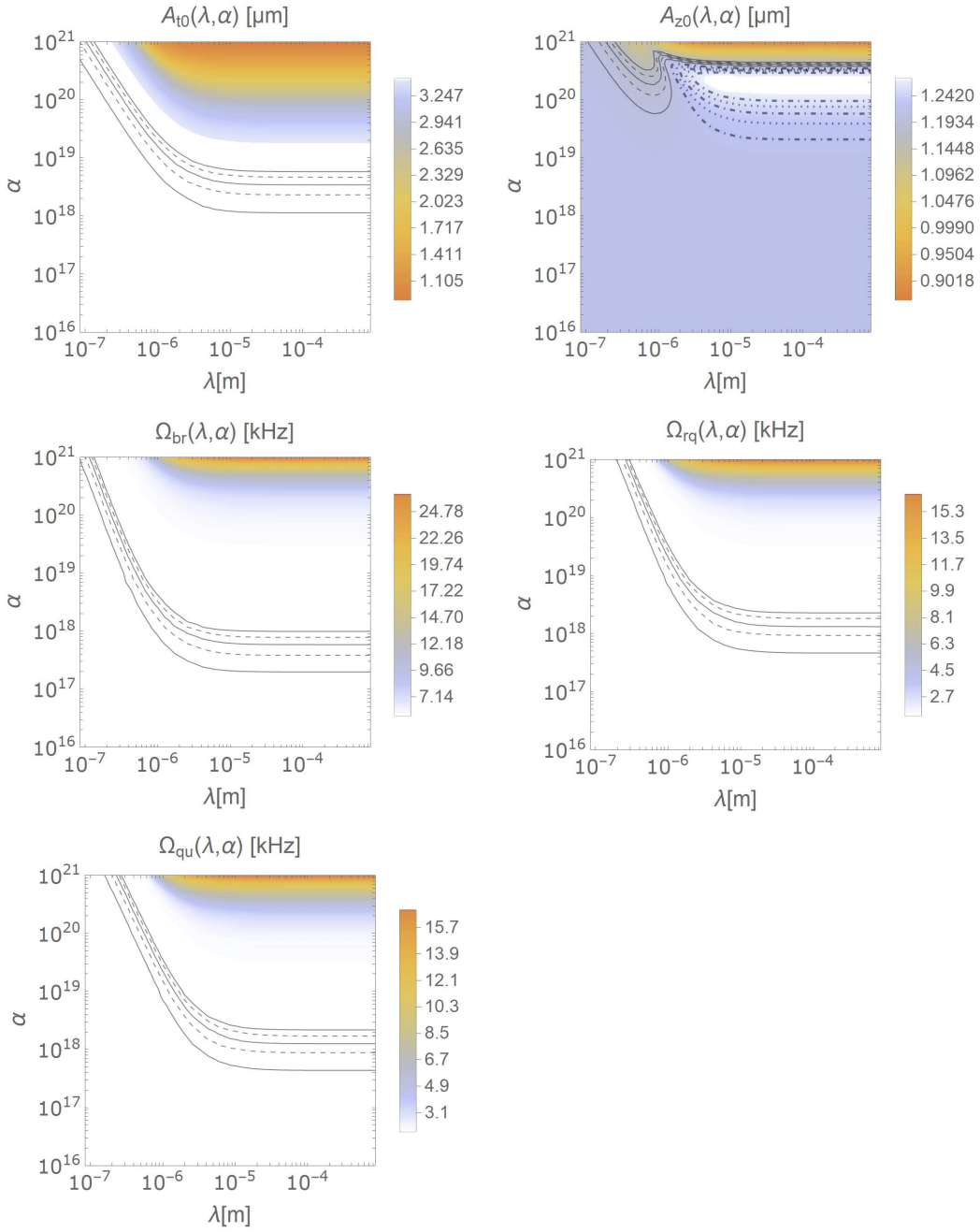

Figure 4.11.: Equilibrium cloud widths A_{t0} and A_{z0} and the collective frequencies Ω_{br}, Ω_{rq}, and Ω_{qu} for a disk-shaped condensate with Yukawa-like interaction and $\zeta = 3$. For A_{z0} the black solid and dashed lines indicate a decrease of 0.01 μm to 0.05 μm and black dashed dotted and dotted lines represent an increase of 0.01 μm to 0.05 μm compared to the Newtonian case. In case of the frequencies, the differences are 1 Hz to 5 Hz.

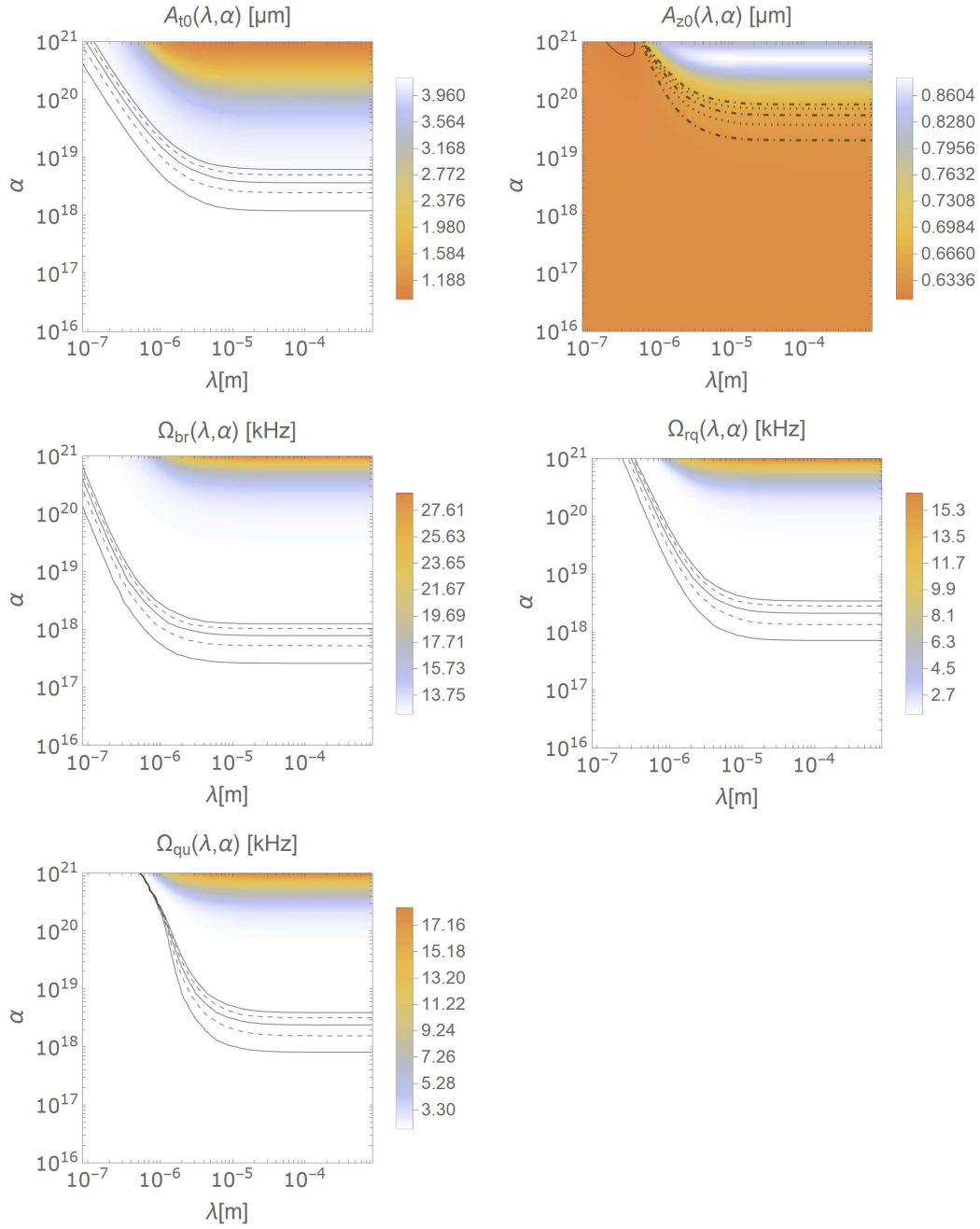

Figure 4.12.: Equilibrium cloud widths A_{t0} and A_{z0} and the collective frequencies Ω_{br}, Ω_{rq}, and Ω_{qu} for a disk-shaped condensate with Yukawa-like interaction and $\zeta = 7$. For A_{z0} the black solid and dashed lines indicate a decrease of 0.01 μm to 0.05 μm and black dashed dotted and dotted lines represent an increase of 0.01 μm to 0.05 μm compared to the Newtonian case. In case of the frequencies, the differences are 1 Hz to 5 Hz.

and $\zeta = 7$, respectively. First of all, the results look very similar to the spherical case discussed in Sec. 3.3.3. Both Gauss widths decrease for higher interaction strengths and larger effective ranges while the collective frequencies increase. Again, it turns out that the frequency belonging to the breathing mode is the largest frequency and the most sensitive in regard to the difference between the Newtonian and Yukawa-like interaction.

As a short remark, taking a closer look at the transversal Gauss width A_{t0} reveals an interesting feature. The black and black dashed lines indicating the difference of 0.01 μm to 0.05 μm towards the Newtonian interaction have a local minimum and increase very slightly again at $\lambda \sim 10^{-5}$ m. This effect is more visible for higher confinements with $\zeta = 1/7$ shown in Fig. 4.10. In principle, it is the same observation as in Sec. 4.2.2, where the lower Gauss width increases for high interaction strengths right before the spherical case occurs. According to this, in the cigar-shaped configuration A_{t0} as the lower Gauss width reaches higher values within a certain area of the strength α before approaching the spherical limit where both Gauss widths coincide. The increase of 0.01 μm to 0.05 μm of the Gaussian width compared to the Newtonian case is indicated by the black dashed dotted and dotted lines. In contrast to the black and black dotted lines they differ by the sign: the solid and dashed lines depict a decrease while the dotted and dashed dotted are showing an increase. In the following two figures Figs. 4.11 and 4.12 for disk-shaped condensates this effect occurs in the Gauss width A_{z0}, as it is lower than A_{t0} here.

Finally, we compare these results with the spherical case discussed in Sec. 3.3.3. As the collective frequency of the breathing mode is the most sensitive we restrict the comparison to Ω_{br} for each case considered. We show the results in Fig. 4.13. On the left side we compare both cigar-shaped condensates $\zeta = 1/3$ and $\zeta = 1/7$ to the spherically symmetric condensate and on the right side analogously for the disk shapes.

In contrast to our first expectations, for quasi one dimensional systems in form of cigar-shaped condensates the lines are very close to each other and do not change much for larger confinement. On the other side though, we see some significant differences in the disk-shaped configuration. There, we improve the boundaries for smaller effective ranges although the lowest boundaries for the interaction strength gets even slightly worse. In accordance to our findings in Figs. 4.7 and 4.8 in particular in regards of the Gaussian widths γ_{t0} and γ_{z0} the effects of a long-range gravitational interaction are more distinct for quasi two dimensional systems. In that sense the same tendency is visible for cigar-shaped condensates although very small.

In the last part of this chapter, we present a method to determine the Yukawa pa-

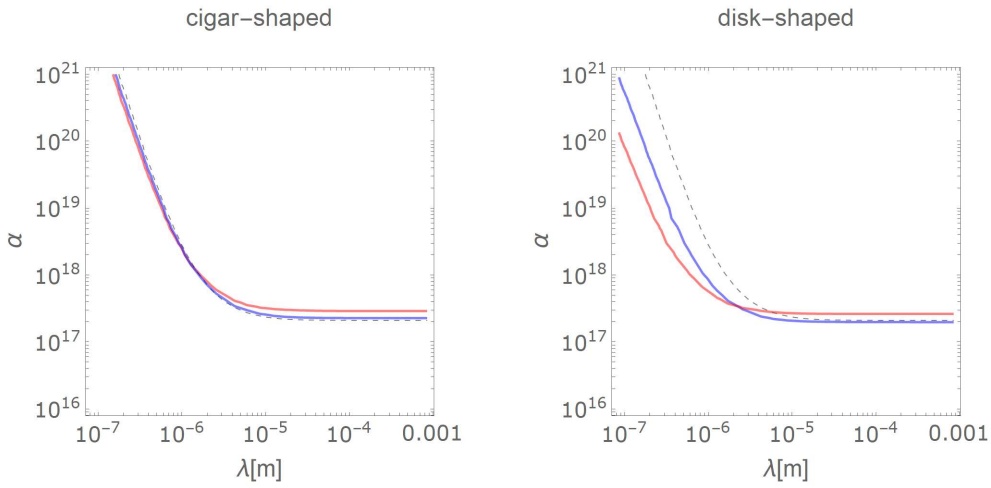

Figure 4.13.: Comparison between the frequencies of the breathing mode. (Left) For cigar-shaped configurations with $\zeta = 1/3$ (blue) and $\zeta = 1/7$ (red) and (Right) for disk-shaped condensate with $\zeta = 3$ (blue) and $\zeta = 7$ (red). In both pictures the black dashed lines correspond to the spherical case taken from Fig. 3.6. All curves indicate a difference of 1 Hz to their respective Newtonian case.

rameters α and λ based on a precise measurement of the collective frequencies. As an example, we consider a condensate of ^{87}Rb atoms with $N = 10^5$ particles, and a trap frequency scale $\omega = 1$ kHz. Furthermore, we assume a disk-shaped configuration with $\zeta = 7$, since this case leads to the best constraints of all our examples so far. If we assume for a moment that the Yukawa parameters are known, we can then calculate the equilibrium cloud widths with Eq. (4.29) and the collective frequencies as eigenvalues of the Hessian matrix with the elements given in Eqs. (4.35)-(4.38). As an example we choose the interaction strength $\alpha = 10^{20}$ and the dimensionless effective range $\bar{\lambda} = 10$, which corresponds to $\lambda = 8.53\ \mu$m in case of the described ^{87} Rb condensate. A numerical calculation then leads to the frequencies $\Omega_{\mathrm{br}} = 12.752$ kHz, $\Omega_{\mathrm{qu}} = 2.023$ kHz, and $\Omega_{\mathrm{rq}} = 1.616$ kHz. The next step is then to look for the corresponding contour lines for each frequency, i.e. in Fig. 4.12. We then combine the contour lines in one figure and by construction all three lines intersect at the initially chosen values of α and λ. This is shown in Fig. 4.14 for the breathing frequency Ω_{br} and the out-of-phase quadrupole frequency Ω_{qu}. We omit the radial quadrupole frequency, since the curve almost completely overlaps with Ω_{qu}. In principle, it is thus possible to determine both Yukawa

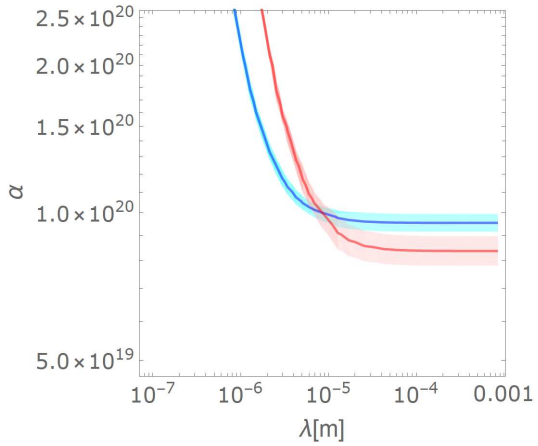

Figure 4.14.: Exemplary determination of the Yukawa parameter α and λ with the collective frequencies of the breathing mode (blue) and the out-of-phase quadrupole mode (red). The blue and red shaded area indicates an assumed error of 20 Hz.

parameters independently by a measurement of at least two collective frequencies. Additionally, we can also include a measurement error of the frequencies, as indicated with the shaded area in Fig. 4.14. Assuming an error of 20 Hz, we can then estimate the errors $\Delta\lambda \approx 3\ \mu$m and $\Delta\alpha \approx 0.1 \cdot 10^{20}$ for both Yukawa parameters in our example. Note that the chosen example of α and λ are already excluded by experimental data, see Fig. 1.4. However, the experimental challenge is a highly precise frequency measurement, since the contour lines of the collective frequencies are very close together, in particular in the non-excluded area. If the error bars are too large, they easily overlap over a huge area, which can be imagined based on Fig. 4.14 for $\lambda > 10^{-5}$ m.

5. Interactions via modified potentials

So far in this work, we have studied two-particle interactions via Newton and Yukawa potentials within both a spherical and an axially symmetric condensate. However, since it is mostly unknown how gravity acts at such small scales, it is possible that gravity does not behave like those two potentials. All theories we have so far available, propose some sort of divergence or singularity at the origin of the gravitational field, more specifically at the origin $r = 0$. So the remaining question is how we approach said singularity. In mathematics, one can classify singularities and define isolated and non-isolated singularities as well as essential or removeable singularities or even poles. Furthermore, direct and indirect transcendental singularities are discussed [117, 118].

In this chapter, however, we propose three additional potentials that might be interesting from a physical point of view. The first one is motivated by [119], which is a modification in form a rational function. The other two potentials are hypothetical and we formulate them as an exponential and a logarithmic function. The modifications here are introduced on the level of the potential energy and serve as toy models for our method. We do not present here any fundamental theories claiming that these potentials emerge from certain differential equations, as it is the case for the Newtonian and Yukawa potential. The potential describing Newtonian gravity arises as a solution to the Poisson equation, while for the Yukawa potential we modify the Poisson equation to the so-called screened Poisson equation.

Nevertheless, in the next section we start with an overview of our proposed modifications and compare them to both the Newtonian and the Yukawa potential. After that we investigate the rational potential. In order to apply the method developed in this work, we need to find the Fourier transform of that potential, which is mathematically challenging and requires a new technique. With the Fourier transformed potential, we then follow the steps in Ch. 3 to determine the equilibrium cloud width and the Hessian matrix. For simplicity, we only consider spherically symmetric condensates in this chapter. The collective frequencies are then again plotted as a contour plot depending

on the parameters α and λ. At the end of this chapter, we make a few remarks on the exponential and logarithmic potentials based on the results of the rational potential.

5.1. Modifications

Here we give a short overview of the modified potentials we assume in this chapter. The three examples are the following

$$V_{\mathrm{rat}}(r) = -\frac{u}{r}\left(1+\alpha\left(\frac{\lambda}{r}\right)^{\epsilon}\right), \tag{5.1a}$$

$$V_{\exp}(r) = -\frac{u}{r}\left(1+\alpha\left[\exp\left\{\left(\frac{\lambda}{r}\right)^{\epsilon}\right\}-1\right]\right), \tag{5.1b}$$

$$V_{\log}(r) = -\frac{u}{r}\left(1-\alpha\log\left[\frac{r}{\lambda}\right]\exp\left\{-\mu\frac{r}{\lambda}\right\}\right). \tag{5.1c}$$

The first one is a generalization of the Newtonian potential where we allow an arbitrary real value for the exponent ϵ. The interaction strength α is dimensionless analogue to the Yukawa potential in (3.64), while the parameter λ has the dimension of a length. In the form of Eq. (5.1) the Newtonian limit is recovered by setting $\epsilon = 0$ and taking the limit $\alpha \to 0$. This potential was indeed discussed in Ref. [119]. In this work we call the first expression in Eq. (5.1) the rational potential.

The other two alternatives demonstrate a hypothetical exponential or logarithmic divergence although we have to add some correction to guarantee the Newtonian limit for larger scales. For the exponential potential we simply have to subtract 1 of the exponential, since

$$\lim_{r\to\infty}\exp\left\{\left(\frac{\lambda}{r}\right)^{\epsilon}\right\} = 1 \tag{5.2}$$

for $\epsilon > 0$ and real λ, such that the second summand vanishes for large r. To obtain the correct Newtonian limit for the logarithmic potential at large distances we choose to add a decreasing exponential term $\exp\left\{-\mu\frac{r}{\lambda}\right\}$ with a dimensionless parameter μ to guarantee that the correction vanishes for large r and to obtain a dimensionless argument. Furthermore, since the function $\log\, r/\lambda$ has a root at $r = \lambda$ and is positive for $r > \lambda$, we have to choose μ such that the positive part becomes negligible. It can be verified numerically that for $\mu > 5$, this part is of the order 10^{-4} and lower. Note

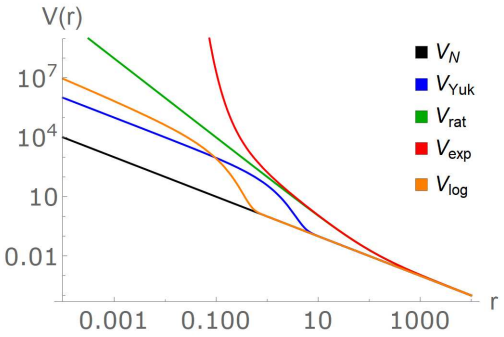

Figure 5.1.: Schematic representation of the modified potentials given in Eq. (5.1): the rational (green), the exponential (red) and the logarithmic potential (orange) compared to the Newton (blue) and Yukawa potential (blue). We choose the parameters $\alpha = 100$, $\lambda = 1$, $\epsilon = 1$, $\mu = 10$ and $u = 1$ as examples.

that an additional exponent ϵ in the argument of the logarithm analogue to the other two examples is irrelevant, since ϵ can then be written as a prefactor in front of the logarithm and thus merged with the interaction strength α.

For illustration purposes we show all three modifications in Fig. 5.1 besides the Newtonian and Yukawa-like potential. By construction all potentials are stronger than the Newtonian potential although this can be easily adjusted by flipping the sign of the strength α if needed. For the chosen parameters in this figure, the rational and exponential potential differ from the Newtonian potential already at larger distances r compared to the Yukawa potential, while for the logarithmic modification this difference occurs at even smaller values. Nonetheless, all three modifications diverge faster than the Newtonian and Yukawa potential and in this example for $r < 0.1$ all five potentials are clearly distinguishable.

In Fig. 5.2 we present the dependency of the potentials in Eq. (5.1) on each parameter individually. In case of the rational and exponential potential, λ cannot be interpreted as an effective range of the potential although it is a length. In fact a variation of λ, as seen in the middle column, shows similar effects as the interaction strength α on the left side for both potentials. The slope of these modifications are adjusted by the parameter ϵ as shown in the right column. In case of the logarithmic potential the curves look quite similar to the Yukawa potential presented in Fig. 3.4. While α can be seen as a strength, both λ and μ determine the effective range of the potential.

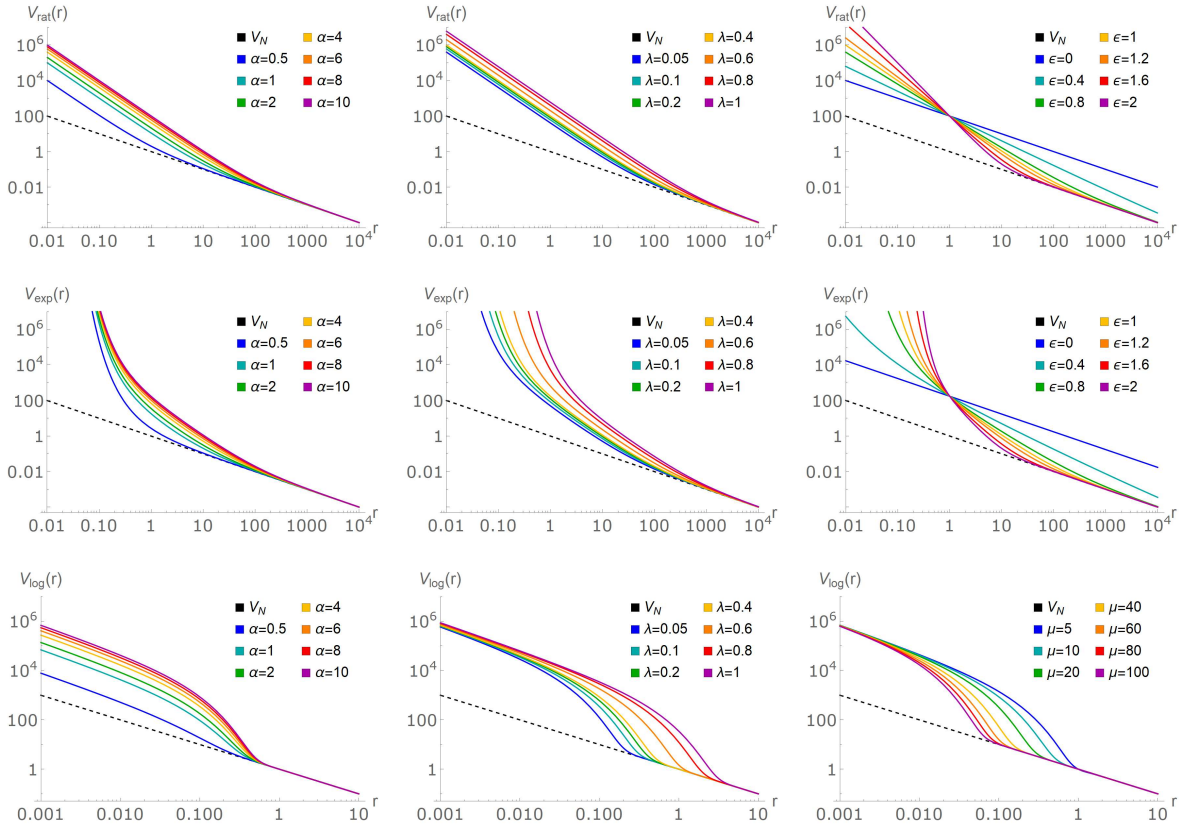

Figure 5.2.: Schematic sketch of the modified potentials given in Eq. (5.1) depending on the parameters α, λ, ϵ or μ, respectively. If a parameter is not varied we set it to the fixed value $\alpha = 100$, $\lambda = 1$, $\epsilon = 1$, $\mu = 10$ and $u = 1$.

All presented potentials have the divergence at the origin in common but each divergence behaves differently. In the following sections we test our theory developed in this thesis to derive once again the collective frequencies of a spherical condensate.

5.2. Rational potential

In this part we investigate the rational potential given in the first expression of Eq. (5.1). Analogue to Sec. 3.2 and Sec. 3.3 we start by deriving the Fourier transformation of the potential. After that we define the integral appearing in the Lagrangian and solve the first and second derivatives of that expression in spherical symmetry. This leads us to an equation for the equilibrium cloud width γ_0 and the elements of the Hessian matrix M.

Again, the collective frequencies of the breathing and quadrupole modes are calculated by the eigenvalues of M depending on the equilibrium cloud width γ_0.

5.2.1. Rational potential in Fourier space

The first step is to find the Fourier transformation of the rational potential

$$V_{\mathrm{rat}}(r) = -\frac{u}{r} - \alpha u \frac{\lambda^\epsilon}{r^{1+\epsilon}}. \tag{5.3}$$

The mathematically necessary condition for a function to be Fourier transformable is that this function is an element of the L_1 space, see also Refs. [120, 121] for more details. This denotes the space of Lebesque-integrable functions whose absolute value has a finite integral. This, however, restricts the number of functions which are Fourier transformable. As an example, the already discussed Newtonian or Coulomb potential is in fact not an element of the L_1 space as the integral does not converge. We have already seen in Sec. 3.2 that we can solve this problem by introducing a convergent factor in form of a decreasing exponential. With this the product of both is in L_1 and we can perform the Fourier transformation. In the end we simply take a limit to get rid of the additional parameter. Here we perform the calculations for the rational potential in a similar way, so we apply the replacement

$$V_{\mathrm{rat}}(r) \to V_{\mathrm{rat}}(r)\mathrm{e}^{-\mu r}. \tag{5.4}$$

We then need to show that the integral over the absolute value leads to a finite expression, i.e.

$$\int \mathrm{d}r\; r^2 \; |V_{\mathrm{rat}}(r)\mathrm{e}^{-\mu r}| < \infty, \tag{5.5}$$

where the factor r^2 originates from the volume element. The angular part can be neglected in this calculation as it is only a fixed factor of 4π. We insert the rational potential (5.3) and apply the triangle inequality for the absolute value

$$\int_0^\infty \mathrm{d}r\; r^2 \; \left| -\frac{u}{r}\mathrm{e}^{-\mu r} - \alpha u \frac{\lambda^\epsilon}{r^{1+\epsilon}}\mathrm{e}^{-\mu r} \right| \leq \int_0^\infty \mathrm{d}r\; r^2 \left(\left| \frac{u}{r}\mathrm{e}^{-\mu r} \right| + \left| \alpha u \frac{\lambda^\epsilon}{r^{1+\epsilon}}\mathrm{e}^{-\mu r} \right| \right) \tag{5.6}$$

This leads to two integrals which are solved by Ref. [108], Eqs. (3.351) and (3.381)

$$u \int_0^\infty \mathrm{d}r\; r\; \mathrm{e}^{-\mu r} + \alpha u \lambda^\epsilon \int_0^\infty \mathrm{d}r\; r^{1-\epsilon}\; \mathrm{e}^{-\mu r} = u \frac{1}{\mu^2} + \alpha u \lambda^\epsilon \Gamma(2-\epsilon) \frac{1}{\mu^{2-\epsilon}}. \tag{5.7}$$

The restriction mentioned in the literature leads to the condition $\epsilon < 2$ in our case. Otherwise, for $\epsilon \geq 2$ the integrand in (5.7) is singular at $r = 0$. The last expression is smaller than infinity, thus we can derive now the Fourier transformation of a product of the rational potential and a decreasing exponential for $\epsilon < 2$.

The Fourier transformation itself is performed analogue to Sec. 3.2.1. In particular, the calculation of the angular part is identical to Eqs. (3.28) to (3.31), which leads to the expression

$$\tilde{V}_{\mathrm{rat}}(k) = -2\pi u \int_0^\infty \mathrm{d}r\; r^2 \left(\frac{1}{r} + \alpha \lambda^\epsilon \frac{1}{r^{1+\epsilon}} \right) \frac{2 \sin kr}{kr}\; \mathrm{e}^{-\mu r}. \tag{5.8}$$

The first summand is the contribution of the Newtonian part derived in Sec. 3.2.1. However, the second part is the correction due to the modification we assumed. It is simplified and evaluated with Ref. [108], Eq. (3.944)

$$\begin{aligned} -4\pi\; \alpha u \lambda^\epsilon\; \frac{1}{k} \int_0^\infty \mathrm{d}r\; \frac{1}{r^\epsilon} \sin kr\; \mathrm{e}^{-\mu r} \\ = -\alpha u \lambda^\epsilon \frac{4\pi}{k} \left(\mu^2 + k^2\right)^{-\frac{1-\epsilon}{2}} \Gamma(1-\epsilon) \sin\left[(1-\epsilon)\; \arctan \frac{k}{\mu} \right]. \end{aligned} \tag{5.9}$$

Once again, the integration is only valid for $\epsilon < 2$. Now we take the limit $\mu \to 0$ and simplify the sine function, such that we get the Fourier transform of the rational potential (5.3)

$$\tilde{V}_{\mathrm{rat}}(k) = -\frac{4\pi u}{k^2} - \alpha \frac{4\pi u}{k^{2-\epsilon}}\; \lambda^\epsilon \cos\left(\frac{\pi}{2}\epsilon\right) \Gamma(1-\epsilon) \tag{5.10}$$

with the restriction $\epsilon < 2$.

The limiting case $\epsilon \to 0$ is quickly determined, since $\cos(\epsilon\pi/2) \to \cos(0) = 1$ and $\Gamma(1-\epsilon) \to \Gamma(1) = 1$ so the limit is given by

$$\tilde{V}_{\mathrm{rat}}(k) \to -\frac{4\pi u}{k^2} - \alpha \frac{4\pi u}{k^2}, \tag{5.11}$$

which reduces to the Newtonian potential if the strength α of the correction is set to zero.

In the end of this section, we mention that it is indeed possible to generalize the expression in (5.10) to $\epsilon > 2$. However, this requires to interpret the function $r^{-1-\epsilon}$ as a generalized function or a distribution. In that sense, this functional is analytically continued and sometimes also called Riesz potential [122]. A detailed mathematical description would go beyond the scope of this thesis, thus we refer to the book given in Ref. [120]. There, the Fourier transformation of the distribution $r^{-1-\epsilon}$ in three dimensions with $r = \sqrt{x^2 + y^2 + z^2}$ is given as

$$\mathcal{F}\left[r^{-1-\epsilon}\right] = 2^{2-\epsilon}\sqrt{\pi^3}\frac{\Gamma\left(\frac{2-\epsilon}{2}\right)}{\Gamma\left(\frac{1+\epsilon}{2}\right)}\frac{1}{k^{2-\epsilon}}, \tag{5.12}$$

see p. 363 in Ref. [120]. In the Appendix D we show explicitly that this expression can be simplified to

$$\mathcal{F}\left[r^{-1-\epsilon}\right] = 4\pi\cos\left(\frac{\pi}{2}\epsilon\right)\Gamma(1-\epsilon)\frac{1}{k^{2-\epsilon}}. \tag{5.13}$$

With the prefactor $-\alpha u$ this is formally identical to the correction term in Eq. (5.10) but now also valid for $\epsilon > 2$.

To visualize the Fourier transformation given in (5.10) we show in Fig. 5.3 the function depending on ϵ. We notice the typical behavior of the Gamma function $\Gamma(x)$, which has simple poles at non-positive integers. In our case the argument of the Gamma function is $1 - \epsilon$ thus these pole occur for positive integers of ϵ. In combination with the cosine function the poles at odd integers vanish. As a result the Fourier transform of the rational potential is undefined at positive and even values of ϵ. This coincides with the conditions given in Ref. [120] and is a fact which we have to take into consideration later on.

5.2.2. Equilibrium width and Hessian matrix

With the Fourier transformed rational potential (5.10) we now write down the Lagrangian for that modification analogue to (3.36) for the Newton interaction and (3.66)

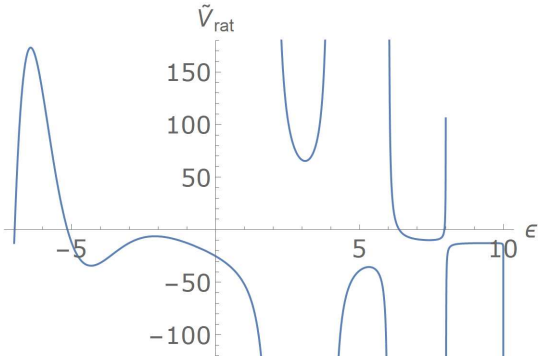

Figure 5.3.: Schematic plot of the Fourier transform of the rational potential given in Eq. (5.10). We choose $\alpha = 1$, $\lambda = 2$, $\kappa = 1$ and $u = 1$ as examples.

for the Yukawa interaction as

$$L_{\text{rat}} = \frac{uN^2}{(2\pi)^2}\sqrt{\frac{m\omega}{\hbar}}\int \mathrm{d}^3\kappa \ \left[\frac{1}{\kappa^2} + \alpha\bar{\lambda}^\epsilon \frac{1}{\kappa^{2-\epsilon}}\cos\left(\frac{\pi}{2}\epsilon\right)\Gamma(1-\epsilon)\right] \times \exp\left\{-\frac{1}{2}(\gamma_x^2\kappa_x^2 + \gamma_y^2\kappa_y^2 + \gamma_z^2\kappa_z^2)\right\} \tag{5.14}$$

with the dimensionless momentum κ defined in Eq. (3.35) and the dimensionless length $\bar{\lambda}$ introduced in (3.67).

Again, we split the integral in a Newtonian part and a correction due to the rational modification and define

$$I_{\text{rat}} = \alpha\bar{\lambda}^\epsilon \cos\left(\frac{\pi}{2}\epsilon\right)\Gamma(1-\epsilon)\int \mathrm{d}^3\kappa \ \frac{1}{\kappa^{2-\epsilon}} \exp\left\{-\frac{1}{2}(\gamma_x^2\kappa_x^2 + \gamma_y^2\kappa_y^2 + \gamma_z^2\kappa_z^2)\right\}. \tag{5.15}$$

Since the cosine and the gamma function are independent of κ, they can be written in front of the integral as a prefactor.

The first derivative of I_{rat} is needed for an expression for the cloud width γ. In spherical symmetry (3.11) and with the angular parts derived in App. B.2 only the radial integral remains which we label as $J_{\text{rat}}^{(j)}$ in accordance to the previous chapters

$$J_{\text{rat}}^{(j)} = -\alpha\frac{4\pi}{3}\gamma\bar{\lambda}^\epsilon \cos\left(\frac{\pi}{2}\epsilon\right)\Gamma(1-\epsilon)\int \mathrm{d}\kappa \ \kappa^{2+\epsilon} \exp\left\{-\frac{1}{2}\gamma^2\kappa^2\right\}. \tag{5.16}$$

In Appendix D we derive the solution

$$J_{\mathrm{rat}}^{(j)} = -\alpha \frac{4\pi}{3} \bar{\lambda}^{\epsilon} \sqrt{2^{\epsilon+1}} \cos\left(\frac{\pi}{2}\epsilon\right) \Gamma(1-\epsilon)\, \Gamma\left(\frac{\epsilon+3}{2}\right) \frac{1}{\gamma^{2+\epsilon}}, \tag{5.17}$$

which is only valid for $\epsilon > -3$.

The full ODE determining the cloud width γ then reads

$$\ddot{\gamma} = -\nu^2\gamma + \frac{1}{\gamma^3} + \frac{P}{\gamma^4} - \frac{Q}{\gamma^2} - \alpha \frac{2Q}{\sqrt{\pi}}\, \bar{\lambda}^{\epsilon} \sqrt{2^{\epsilon}} \cos\left(\frac{\pi}{2}\epsilon\right) \Gamma(1-\epsilon)\, \Gamma\left(\frac{3+\epsilon}{2}\right) \frac{1}{\gamma^{2+\epsilon}} \tag{5.18}$$

with the same gravitational interaction strength Q defined in Eq. (3.46). Thus, we determine the equilibrium cloud width γ_0 by

$$-\nu^2\gamma_0 + \frac{1}{\gamma_0^3} + \frac{P}{\gamma_0^4} - \frac{Q}{\gamma_0^2} - \alpha \frac{2Q}{\sqrt{\pi}}\, \bar{\lambda}^{\epsilon} \sqrt{2^{\epsilon}} \cos\left(\frac{\pi}{2}\epsilon\right) \Gamma(1-\epsilon)\, \Gamma\left(\frac{3+\epsilon}{2}\right) \frac{1}{\gamma_0^{2+\epsilon}} = 0. \tag{5.19}$$

Next, the second derivatives of I_{rat} again in spherical symmetry results in the following radial integrals

$$J_{\mathrm{rat}}^{(jj)} = \alpha\, 4\pi \bar{\lambda}^{\epsilon} \cos\left(\frac{\pi}{2}\epsilon\right) \Gamma(1-\epsilon) \int \mathrm{d}\kappa\, \left(\frac{\gamma^2}{5}\kappa^4 - \frac{1}{3}\kappa^2\right) \kappa^{\epsilon} \exp\left\{-\frac{1}{2}\gamma^2\kappa^2\right\} \tag{5.20}$$

and

$$J_{\mathrm{rat}}^{(jk)} = \alpha \frac{4\pi}{15} \gamma^2 \bar{\lambda}^{\epsilon} \cos\left(\frac{\pi}{2}\epsilon\right) \Gamma(1-\epsilon) \int \mathrm{d}\kappa\, \kappa^{4+\epsilon} \exp\left\{-\frac{1}{2}\gamma^2\kappa^2\right\} \tag{5.21}$$

for the diagonal and off-diagonal elements. The solution of both integrals is explained in Appendix D. We give here the results

$$J_{\mathrm{rat}}^{(jj)} = \alpha \frac{4\pi}{15} \bar{\lambda}^{\epsilon} \sqrt{2^{\epsilon+1}} (4+3\epsilon) \cos\left(\frac{\pi}{2}\epsilon\right) \Gamma(1-\epsilon)\, \Gamma\left(\frac{\epsilon+3}{2}\right) \frac{1}{\gamma^{3+\epsilon}} \tag{5.22}$$

and

$$J_{\mathrm{rat}}^{(jk)} = \alpha \frac{4\pi}{15} \bar{\lambda}^{\epsilon} \sqrt{2^{\epsilon+3}} \cos\left(\frac{\pi}{2}\epsilon\right) \Gamma(1-\epsilon)\, \Gamma\left(\frac{\epsilon+5}{2}\right) \frac{1}{\gamma^{3+\epsilon}} \tag{5.23}$$

if $\epsilon > -1$.

The elements of the complete Hessian matrix M including the contact and Newtonian

interaction as well as the rational modification are then given by

$$M^{(jj)} = \nu^2 + \frac{3}{\gamma_0^4} + \frac{2P}{\gamma_0^5} - \frac{4}{5}\frac{Q}{\gamma_0^3} - \alpha\,\frac{2Q}{5\sqrt{\pi}}(4+3\epsilon)\bar{\lambda}^\epsilon\sqrt{2^\epsilon}\cos\left(\frac{\pi}{2}\epsilon\right)\Gamma(1-\epsilon)\,\Gamma\left(\frac{\epsilon+3}{2}\right)\frac{1}{\gamma_0^{3+\epsilon}}, \tag{5.24a}$$

$$M^{(jk)} = \frac{P}{\gamma_0^5} - \frac{3}{5}\frac{Q}{\gamma_0^3} - \alpha\,\frac{4Q}{5\sqrt{\pi}}\bar{\lambda}^\epsilon\sqrt{2^\epsilon}\cos\left(\frac{\pi}{2}\epsilon\right)\Gamma(1-\epsilon)\,\Gamma\left(\frac{\epsilon+5}{2}\right)\frac{1}{\gamma_0^{3+\epsilon}}. \tag{5.24b}$$

Now, we verify quickly the correct Newtonian limit of the Eq. (5.19) and Eqs. (5.24). As mentioned earlier, for this we simply take the limit $\epsilon \to 0$. With the limiting cases of the cosine and the gamma function already mentioned for Eq. (5.11), and in addition with the values $\Gamma(3/2) = \sqrt{\pi}/2$ and $\Gamma(5/2) = 3\sqrt{\pi}/4$, this immediately leads to

$$\ddot{\gamma} = -\nu^2\gamma + \frac{1}{\gamma^3} + \frac{P}{\gamma^4} - \frac{Q}{\gamma^2} - \alpha\frac{Q}{\gamma^2}, \tag{5.25a}$$

$$M^{(jj)} = \nu^2 + \frac{3}{\gamma_0^4} + \frac{2P}{\gamma_0^5} - \frac{4}{5}\frac{Q}{\gamma_0^3} - \alpha\frac{4}{5}\frac{Q}{\gamma_0^3}, \tag{5.25b}$$

$$M^{(jk)} = \frac{P}{\gamma_0^5} - \frac{3}{5}\frac{Q}{\gamma_0^3} - \alpha\frac{3}{5}\frac{Q}{\gamma_0^3}. \tag{5.25c}$$

Decreasing the interaction strength α then successfully results in the correct limit given in Eq. (3.47) and Eq. (3.57).

5.2.3. Discussion

In this section we present the numerical results for a condensate with a hypothetical interaction caused by a rational potential. Analogue to previous discussions we first evaluate Eq. (5.19) in the alternative form

$$\gamma_0^5 - \gamma_0 - P + Q\gamma_0^2 + \alpha Q\frac{2}{\sqrt{\pi}}\,\bar{\lambda}^\epsilon\sqrt{2^\epsilon}\cos\left(\frac{\pi}{2}\epsilon\right)\Gamma(1-\epsilon)\,\Gamma\left(\frac{3+\epsilon}{2}\right)\gamma_0^{2-\epsilon} = 0, \tag{5.26}$$

where we set $\nu = 1$ without loss of generality. We then put the results for γ_0 into the Hessian matrix given in Eq. (5.24) and calculate the eigenvalues. Again, the collective frequencies are given by the square root of these eigenvalues.

According to Sec. 3.1.3 and Sec. 3.2.3 we set the interactions strengths to $P = 446$ and $Q = 4.1 \cdot 10^{-19}$ throughout all calculations in this section. Furthermore, we first present

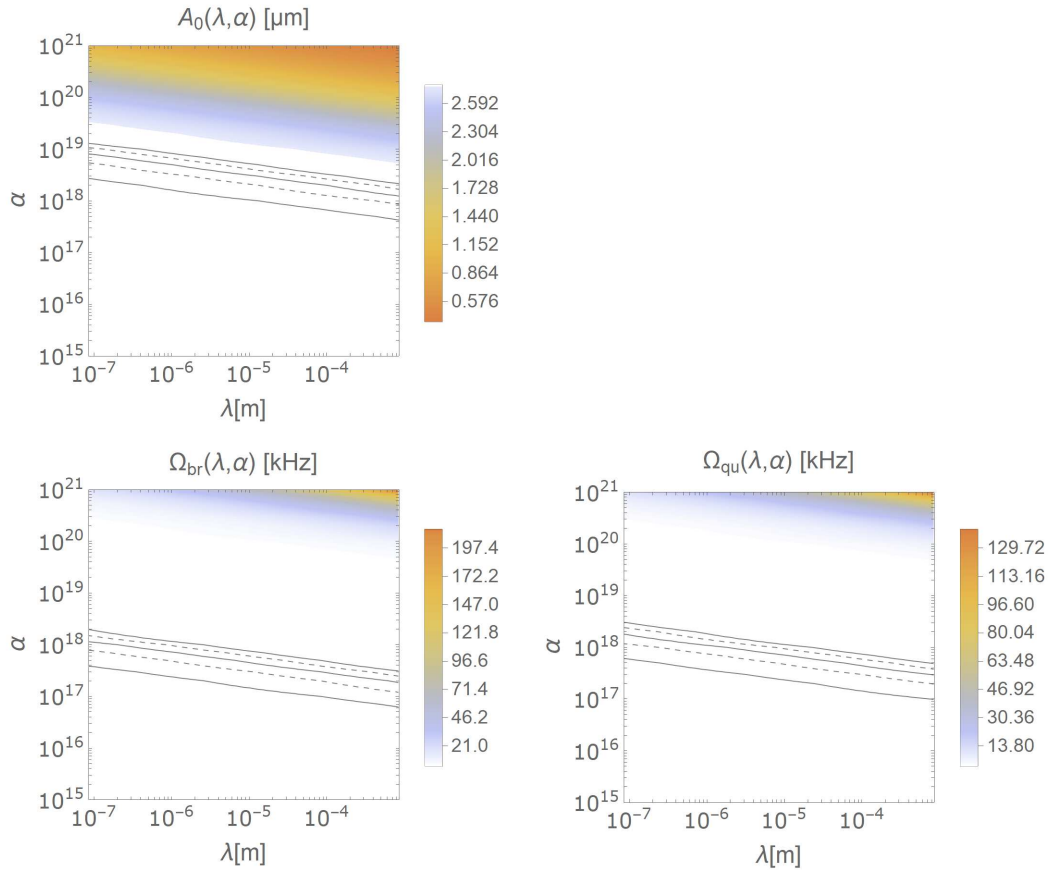

Figure 5.4.: Contour plots for the equilibrium cloud width A_0 and the collective frequencies Ω_{br} and Ω_{qu} for a spherical BEC with an interaction via the rational potential with $\epsilon = 0.2$. The black lines indicate a difference of 0.01 μm to 0.05 μm or 1 Hz to 5 Hz, respectively, compared to the Newtonian case treated in Sec. 4.2.

the contour plots of the equilibrium cloud width A_0 and the collective frequencies Ω_{br} and Ω_{qu} for some values of ϵ. To compare the results with the contour plots for the Yukawa-like interaction discussed in Sec 3.3.3, we choose for α and λ roughly the same range of values. Additionally, it turns out that the quadrupole modes are degenerate as we have seen before for spherical condensates.

Figure 5.4 shows the results for $\epsilon = 0.2$. In the first picture we see the equilibrium width A_0, which, in absolute values, is of the same order than the results of the Yukawa-like interaction shown in Fig. 3.5 as indicated by the color code. However, on the upper side for large interaction strengths we reach lower cloud widths. It is remarkable that even for $\lambda \approx 10^{-7}$ m the black curves indicating a difference of 0.01 μm to 0.05 μm

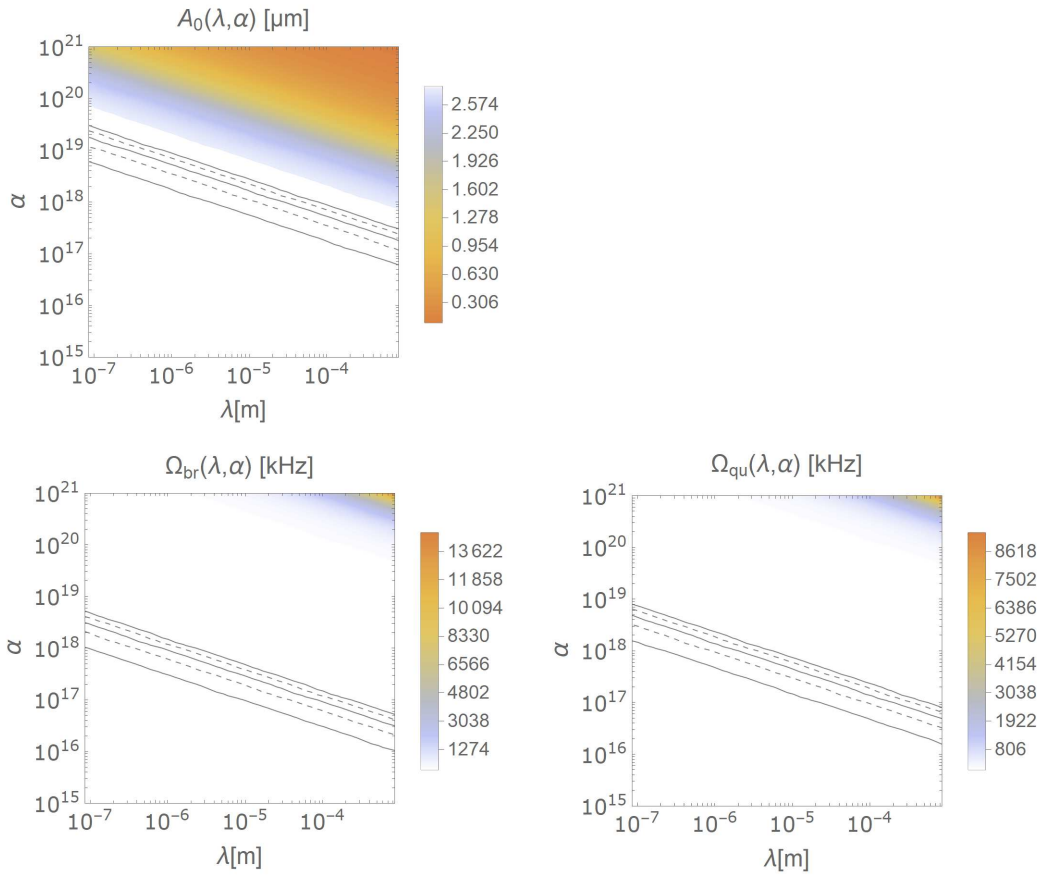

Figure 5.5.: Contour plots for the equilibrium cloud width A_0 and the collective frequencies Ω_{br} and Ω_{qu} for a spherical BEC with an interaction via the rational potential with $\epsilon = 0.5$. The black lines indicate a difference of 0.01 μm to 0.05 μm or 1 Hz to 5 Hz, respectively, compared to the Newtonian case treated in Sec. 4.2.

to the Newtonian case are at values of α of the order 10^{18}, which is a clear distinction between both interactions. The same behavior is found for the collective frequencies in the bottom row of Fig. 5.4. Compared to the frequencies for the Yukawa-like interaction in Fig. 3.6 the frequencies for the rational interaction are almost ten times larger. Thus it is not surprising that the black lines are lower as their Yukawa counterparts.

In Fig. 5.5 we show the results for $\epsilon = 0.5$. We clearly see that increasing the parameter ϵ leads to a larger slope of the curves. This agrees with our previous findings in Sec. 5.1. However, note that the collective frequencies are drastically increased. This gets even worse as we approach the singular point $\epsilon = 2$. As an example, we present the collective

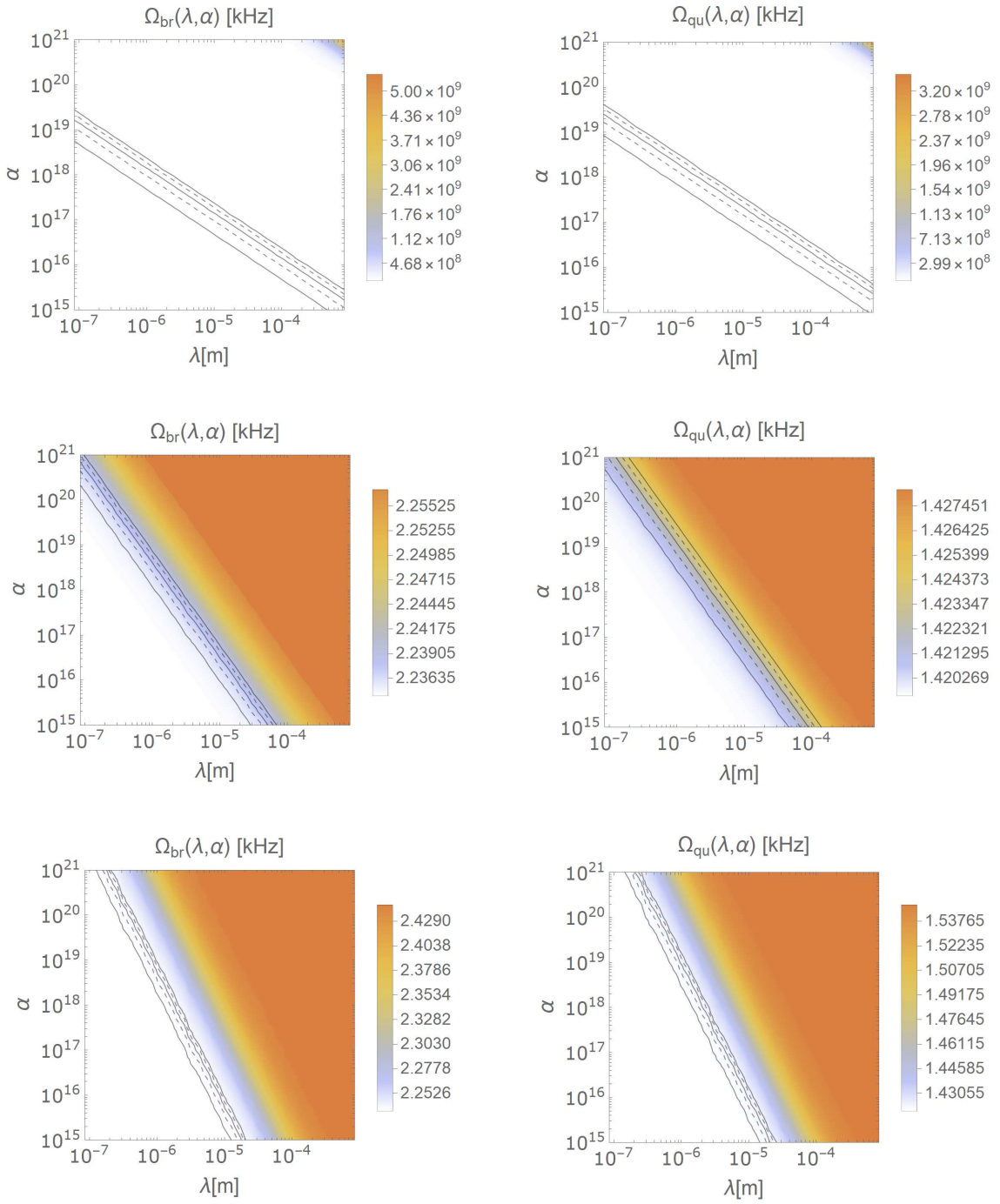

Figure 5.6.: Collective frequencies Ω_{br} and Ω_{qu} for $\epsilon = 1$ (top row), $\epsilon = 2.1$ (mid row) and $\epsilon = 3$ (bottom row). The black lines indicate a difference of 1 Hz to 5 Hz, respectively, compared to the Newtonian case treated in Sec. 4.2.

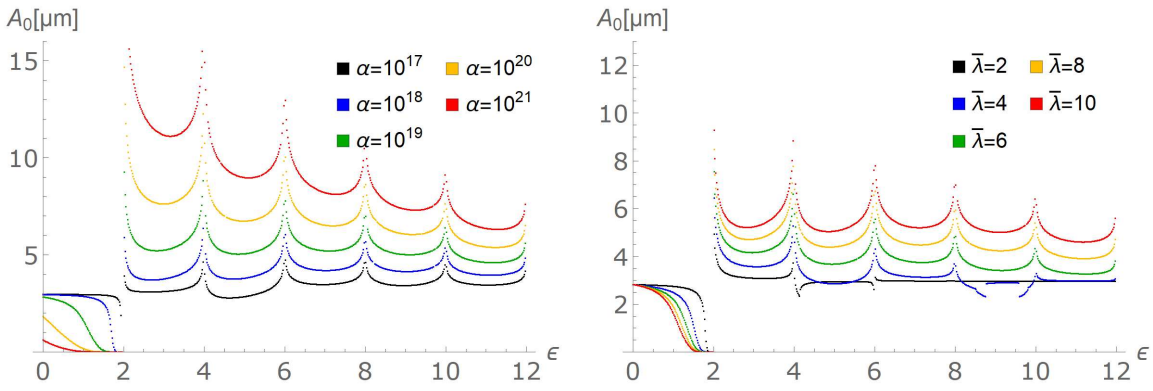

Figure 5.7.: Equilibrium cloud width A_0 depending on ϵ. On the left side we set $\bar{\lambda} = 10$ and on the right side $\alpha = 10^{19}$.

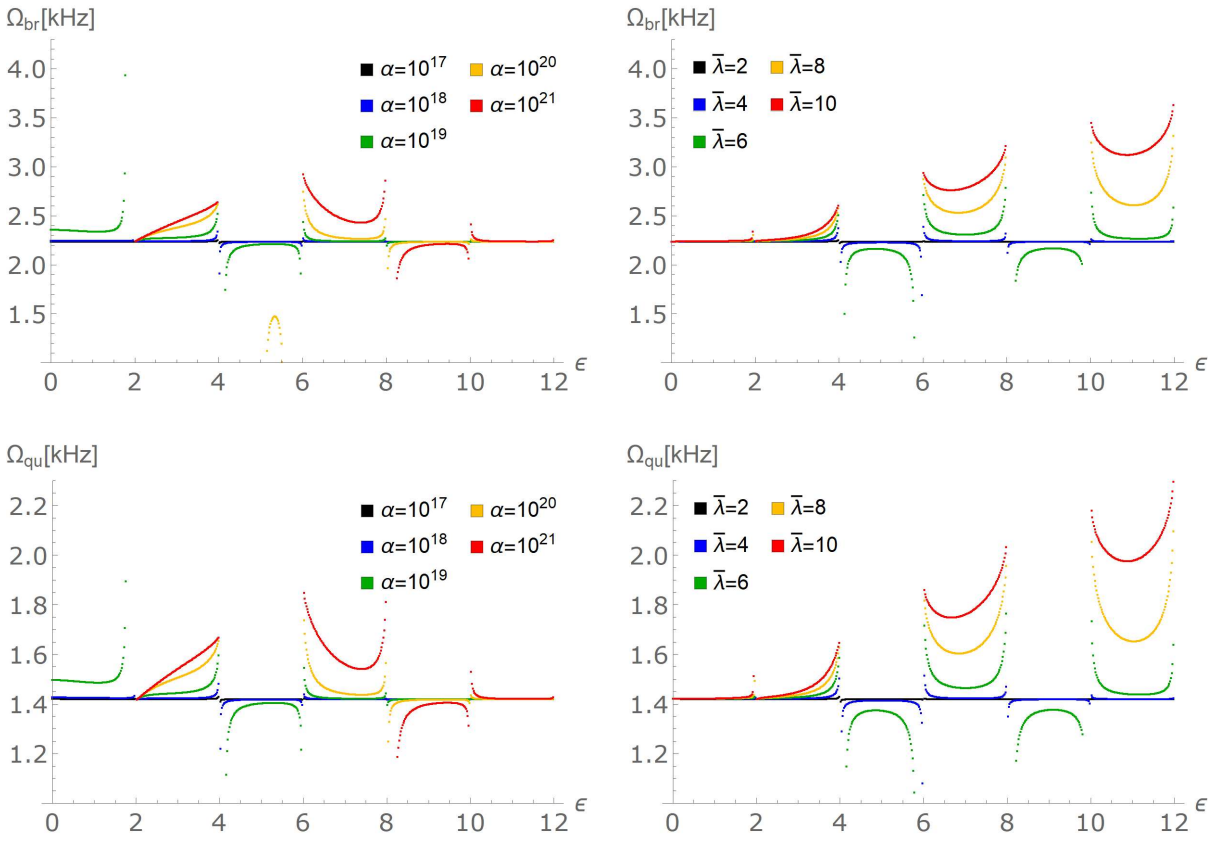

Figure 5.8.: Collective frequencies Ω_{br} and Ω_{qu} depending on ϵ. In the left column we set $\bar{\lambda} = 2$ and in the right column $\alpha = 10^{17}$.

frequencies in case of $\epsilon = 1$ in Fig. 5.6 at the top. Surprisingly, beyond the singularity we get again some plausible frequencies as also shown in Fig. 5.6 for $\epsilon = 2.1$ and $\epsilon = 3$.

To investigate this behavior we now present the equilibrium width and the collective frequencies in dependence of ϵ for fixed values of α and λ. The numerical procedure is basically identical to the previous one and the results are given in Figs. 5.7 and 5.8. The explicit values for α and λ are given in the captions of each figure. On first sight we clearly see the singularities for even integers of ϵ in accordance to Fig. 5.3. For $\epsilon < 2$ the equilibrium cloud width A_0 is decreasing for each larger ϵ, α and λ as we expect for larger attractive interactions. As a reminder, in this area of ϵ we have shown in Sec. 5.2.1 that the traditional Fourier transformation is valid and the Fourier transformed potential can be calculated in a straightforward manner. However, for $\epsilon > 2$ we have to rely on a generalized formalism allowing us to calculate Fourier transformations of distributions. In our case of a spherical condensate the numerical calculations for $\epsilon > 2$ indicate a drastic increase of the size of the condensate represented by a large equilibrium width A_0. In between each singularity we also see a local minimum.

The collective frequencies shown in Fig. 5.8 are also not defined for even integers of ϵ. In between it shows a similar behavior than the equilibrium cloud width with the addition that the sign of the correction seems to alternate.

Although these results seem incorrect from a physical point of view, in the appendix E we verify at least the behavior of the equilibrium cloud width with an alternative method. This method is based of the effective potential introduced in Eq. (2.36).

5.3. Logarithmic potential

In this section we give a few short remarks on the logarithmic potential defined in Eq. (5.1)

$$V_{\log} = -\frac{u}{r} + \alpha u \frac{1}{r} \ln\left[\frac{r}{\lambda}\right] \exp\left\{-\mu \frac{r}{\lambda}\right\}. \tag{5.27}$$

First of all, we could not find a proper Fourier transformation of this potential. However, instead we consider the following series expansion

$$\ln(1+x) = \sum_{k=1}^{\infty} (-1)^{k+1} \frac{x^k}{k} = x - \frac{x^2}{2} + \frac{x^3}{3} - \frac{x^4}{4} + \cdots . \tag{5.28}$$

With the simple substitution

$$1 + x = \frac{r}{\lambda} \;\rightarrow\; x = \frac{r}{\lambda} - 1, \tag{5.29}$$

we express the logarithm in (5.27) as

$$\ln\left[\frac{r}{\lambda}\right] = \left(\frac{r}{\lambda} - 1\right) - \frac{1}{2}\left(\frac{r}{\lambda} - 1\right)^2 + \frac{1}{3}\left(\frac{r}{\lambda} - 1\right)^3 - \cdots . \tag{5.30}$$

Together with the expansion

$$\exp\left\{-\mu\frac{r}{\lambda}\right\} = 1 - \mu\frac{r}{\lambda} + \frac{1}{2!}\left(\mu\frac{r}{\lambda}\right)^2 - \frac{1}{3!}\left(\mu\frac{r}{\lambda}\right)^3 + \cdots \tag{5.31}$$

and the prefactor $1/r$ we write the potential (5.27) as

$$V_{\log} = -\frac{u}{r} + \alpha u\left[-\frac{1}{r} + \sigma_0(\lambda,\mu) + \sigma_1(\lambda,\mu)r + \sigma_2(\lambda,\mu)r^2 + \cdots\right], \tag{5.32}$$

where $\sigma_p(\lambda,\mu)$ are some constants. This is a series in r^p with $p \in \mathbb{Z}_{\geq -1}$. In terms analogue to the rational potential $r^{-(1+\epsilon)}$ we set $p = -1 - \epsilon \geq -1$. As a consequence, we have the condition $\epsilon \leq 0$. So in general the Fourier transform of the logarithmic potential exists as the sum over all Fourier transformations of the rational potential with $\epsilon \in \mathbb{Z}_{\leq 0}$. However, for the differential equation and the elements of the Hessian matrix we have to evaluate $J^{(j)}$, $J^{(jj)}$ and $J^{(jk)}$, which are only solvable for $\epsilon > -3$ and $\epsilon > -1$, respectively. Apart from finitely many terms this is a contradiction such that we cannot analytically evaluate the logarithmic potential with the method discussed in this thesis.

5.4. Exponential potential

The last potential we originally wanted to discuss is the exponential potential given in (5.1)

$$V_{\exp} = -\frac{u}{r} - \alpha u\frac{1}{r}\left(\exp\left\{\left(\frac{\lambda}{r}\right)^{\epsilon}\right\} - 1\right). \tag{5.33}$$

Analogous to the previous section we were not able to find a Fourier transform, thus we apply the series expansion

$$\exp\left\{\left(\frac{\lambda}{r}\right)^{\epsilon}\right\} = 1 + \left(\frac{\lambda}{r}\right)^{\epsilon} + \frac{1}{2!}\left(\frac{\lambda}{r}\right)^{2\epsilon} + \frac{1}{3!}\left(\frac{\lambda}{r}\right)^{3\epsilon} + \cdots \tag{5.34}$$

which results a series in $r^{-1-\epsilon p}$ with $p \in \mathbb{Z}_{\geq 0}$ for the potential in Eq. (5.33). The case $p = 1$ corresponds to the rational potential and $p = 0$ to the Newtonian potential.

If we now substitute $\tilde{\epsilon} = \epsilon p$, each term of the series is mathematically identical to the rational potential. As also discussed for the logarithmic potential, we need to fulfill two conditions in order for our method to work: i) the Fourier transform exists at every point except when $\tilde{\epsilon}$ is an even integer and ii) for the calculation of $J^{(j)}$, $J^{(jj)}$ and $J^{(jk)}$ for each term individually we need $\tilde{\epsilon} > -3$ or $\tilde{\epsilon} > -1$.

In the series in $r^{-1-\epsilon p}$ we now distinguish two cases. For $\epsilon < 0$ it turns out that we violate the second condition (ii). How ever small ϵ is at some value of p the product will eventually be $\epsilon p < -3$. As a consequence, we are then not able to derive $J^{(j)}$, $J^{(jj)}$ and $J^{(jk)}$ needed for the differential equation and the Hessian matrix. On the other side if $\epsilon > 0$ we know from the first condition (i) that the product ϵp must be different from even integers. The only possibility to guarantee this in the infinite sum over p is that ϵ is an irrational number. However, we were not able to find a Fourier transform for these cases.

6. Conclusions

6.1. Summary

According to current knowledge, it is still unclear if Newton's theory of gravity is valid for arbitrary short distances. Many theories even predict deviations from Newtonian gravity due to the existence of exotic particles or extra dimensions. As a consequence, numerous experimental tests have been carried out in the search for evidences to these claims. A wide variety of systems and effects were studied like the torsion balance pendulum [76, 67], collider experiments [72, 73, 74] and the Casimir effect [78, 79, 80]. So far, all experiments have verified Newton's law of gravity up to a certain range for different parameters as shown for example in Fig. 1.4.

The main goal of this thesis was to improve the theoretical constraints by using self-gravitating Bose-Einstein condensate. In this model we assumed that each particle in the condensate interacts via a gravitational potential in addition to the commonly used contact interaction. In order to encourage experimental tests, we decided to study the low-lying collective frequencies of the condensate. On the one hand, they are experimentally accessible via time-of-flight measurements or even in-situ by using photonic systems as platform, and can be measured with a relative precision of 10^{-3} [46]. On the other hand, it is known that these frequencies are sensitive to the character of the interaction, see e.g. Refs. [99, 112]. Hence, we predict in the following the changes in the collective frequencies caused by a hypothetical gravitational interaction.

Inspired by Refs. [99] and [100], we began this work in Ch. 2 by presenting the variational method. This is an approach to find approximate solutions to the time-dependent Gross-Pitaevskii equation with small interactions. The solutions are given in form of differential equations for the cloud widths in each spatial direction. The linearisation of the differential equations around the steady state then led to a matrix, of which its eigenvalues corresponded to the frequencies of the oscillations.

The general expressions for arbitrary interactions and without any assumptions of symmetry derived in Ch. 2 are then specified in Ch. 3 to spherically symmetric condensates. To verify our calculations so far, we assumed the contact interaction and reproduced then known results from the literature. This included the dependence of the equilibrium cloud width as well as the collective frequencies on the contact interaction strength. Next, we considered a Newtonian two-particle interaction. Due to the divergence at the origin, however, we performed the calculation in the Fourier space. This method is also discussed in the context of dipolar interaction, see Ref. [112]. From this, we analytically derived corrections to the collective frequencies, which, as expected, turned out to be too small to be measured experimentally, in particular twenty orders of magnitude smaller than the contact interaction. Since we are interested in modifications to Newton's law, we performed the calculations for the most prominent modified potential, namely the Yukawa potential, which includes two additional parameter the interaction strength α and the effective range λ. Especially α is of interest, as it can easily compensate the difference between contact and Newtonian interaction. We derived the equilibrium cloud width and the collective frequencies as a function of both parameters and therefore present the results as contour plots showing the constraints for both Yukawa parameters. Furthermore, we studied the influence of the particle number, the s-wave scattering length, the trap frequency, and the mass given by the atomic species. Assuming accurate frequency measurements of 1 Hz, we have shown that under certain experimentally feasible conditions, the constraints are slightly improved in the region of $\lambda \approx 10^{-8}$ m and $\alpha \approx 10^{24}$.

In Ch. 4 we generalized our calculations to axially symmetric condensates. Although more realistic experimentally, we also wanted to further improve the constraints with condensates in lower dimensions. It is known from the literature that the contact interaction strength increases when the condensate is strongly confined to quasi two or one dimensions [115, 116]. The strength of the confinement is quantified by the trap-aspect ratio ζ, the ratio between the trap frequencies in the transversal and longitudinal directions. The aspect ratio determines the geometry of the condensate and one can distinguish between cigar-shaped, spherical, and disk-shaped condensates. Again, we studied the contact interaction, the Newtonian interaction and the Yukawa-like interaction, now including a dependence on the aspect ratio. In case of a disk-shaped condensate with $\zeta = 7$, we achieved an improvement of the constraints for the effective range λ additionally by half an order of magnitude compared to the spherical case. Additionally,

by measuring at least two collective frequencies, we have shown that it is in principle possible to determine both Yukawa parameters α and λ independently.

In the last chapter we intended to test our model with more exotic gravitational potentials, where each represents a different class of divergence at the origin. As examples we chose a rational potential, followed by a logarithmic and an exponential modification to the Newtonian potential. The first one is inspired by Ref. [119], while the second and third examples are proposed by us. Nevertheless, we had to guarantee that the potentials all converge to the Newtonian potential for larger distances. In case of the rational potential, its Fourier transform is restricted in the common sense to $\epsilon < 1$, where $1 + \epsilon$ is the exponent of the modification. However, by generalizing the concept of the Fourier transformation to distributions, we found an expression also valid for $\epsilon > 2$ at the cost of poles for positive even integers of ϵ. With this, we derived for a spherically symmetric condensate an equation for the equilibrium cloud width as well as the elements of the Hessian matrix and verified the correct Newtonian limit by $\epsilon \to 0$. In the end, however, it turns out that the numerical calculations show very large values of the equilibrium cloud width, in particular for $\epsilon > 2$. Therefore, we interpret the results as unphysical. For the logarithmic and the exponential modification we could neither find a Fourier transform nor a series expansion in terms of the rational potential due to the poles at positive even integers as mentioned before. Consequently, we were not able to derive the differential equations.

6.2. Outlook

The purpose of any theory is its validation by experimental measurements. We explicitly stated all requirements for the particle number, the scattering length, the mass, and the trapping frequency as well as the measurement precision in physical units, for which we predict visible deviations. Although it may be difficult to meet the requirements, we hope that in the future there will be some experimental efforts in this direction in the future, since the basic idea of measuring the collective frequencies by time-of-flight measurements is common knowledge.

Furthermore, a full numerical calculation by solving the Gross-Pitaevskii-Newton system, consisting of the Gross-Pitaevskii equation and the Poisson equation, would further verify the results of this thesis. In case of the Yukawa potential, one has to replace the

Poisson equation by the screened Poisson equation, which takes into account the effective range.

From a theoretical point of view, it would be interesting to see a rigorous derivation of the studied system from first principles. In addition, one could also investigate the Bogoliubov spectrum, which leads to a dispersion relation between energy and momentum [38]. In this context, a gravitational interaction might also affect the sound wave velocity at which excitations are moving. Furthermore, one could include e.g. three-particle interactions [123, 124] due to the long-range nature of the gravitational potential. The Gaussian ansatz used throughout the thesis could also be expanded by an explicit phase dependency. With this, one could study the formation of vortices as phase singularities [125] and gravitational effects on them.

A very exciting topic is the investigation of other modes than the ones discussed here. In particular, the so-called scissors modes could be of interest. It was shown that these modes are purely two-dimensional density variations [38, 126] and that they can be induced by a sudden rotation of the trap potential [127]. As we have seen in this thesis, the effects of a gravitational self-interaction are largest for a disk-shaped condensate, which is a quasi two dimensional system. Thus, exciting a scissors mode could lead to some interesting results.

Besides a Yukawa-like modification, one could also consider other approaches to modified gravity, e.g. so-called screening mechanisms [128]. These models are designed to have a significant impact at shorter ranges, but not to cause deviations at larger scales. One example are the chameleon fields, which consist of a mass-density dependent scalar field coupled to gravity [129, 85]. Due to an antiproportional relation, the effects are increased for small densities. An experiment using a cesium matter-wave interferometer was already performed, see Ref. [130]. In context of a dilute condensate, the effects of a chameleon field may be greater than the Yukawa potential discussed in this thesis.

A. Lagrangian of the Newtonian interaction in position space for spherical symmetry

In this appendix we present a method to evaluate the Lagrangian of the Newtonian interaction given by (3.21) in the position space. As mentioned in Sec. 3.2 this was already done in a diploma thesis, see Ref. [111], so further details can be found there.

The first step is to rewrite the denominator in (3.21) as $|\mathbf{r}-\mathbf{r}'| = \sqrt{(\mathbf{r}-\mathbf{r}')^2}$. In this form we apply the Schwinger formula, see also Ref. [131]

$$\frac{1}{a^z} = \frac{1}{\Gamma(z)} \int_0^\infty \mathrm{d}y \; y^{z-1} \mathrm{e}^{-ay} \tag{A.1}$$

for $a > 0$, such that

$$\frac{1}{\sqrt{(\mathbf{r}-\mathbf{r}')^2}} = \frac{1}{\Gamma(1/2)} \int_0^\infty \mathrm{d}y \; \frac{1}{\sqrt{y}} \exp\left\{-(\mathbf{r}-\mathbf{r}')^2 y\right\}. \tag{A.2}$$

With $\Gamma(1/2) = \sqrt{\pi}$ we insert the equation above as well as the Gaussian ansatz (2.11) into the Lagrangian (3.21), which leads to

$$\begin{aligned} L_\mathrm{N} =& \frac{1}{2} \frac{u}{\sqrt{\pi}} \frac{N^2}{\pi^3 A_1^2 A_2^2 A_3^2} \cdot \\ & \cdot \int \mathrm{d}^3 r \int \mathrm{d}^3 r' \int_0^\infty \mathrm{d}y \; \frac{1}{\sqrt{y}} \exp\left\{-(\mathbf{r}-\mathbf{r}')^2 y\right\} \exp\left\{-\sum_{j=1}^3 \frac{1}{A_j^2}(r_j^2 + r_j'^2)\right\}. \end{aligned} \tag{A.3}$$

Rearranging the integrals gives

$$L_{\mathrm{N}} = \frac{1}{2}\frac{u}{\sqrt{\pi}}\frac{N^2}{\pi^3 A_1^2 A_2^2 A_3^2} \cdot \cdot \int_0^\infty \mathrm{d}y \, \frac{1}{\sqrt{y}} \prod_{j=1}^{3} \int \mathrm{d}x_j \int \mathrm{d}x_j' \exp\left\{-(x_j - x_j')^2 y - \frac{1}{A_j^2}(x_j^2 + x_j'^2)\right\}. \tag{A.4}$$

The integrals over the spatial coordinates x_j are Gaussian integrals and thus solvable

$$L_{\mathrm{N}} = \frac{1}{2}\frac{u}{\sqrt{\pi}}\frac{N^2}{\pi^3 A_1^2 A_2^2 A_3^2} \int_0^\infty \mathrm{d}y \, \frac{1}{\sqrt{y}} \prod_{j=1}^{3} \frac{\pi A_j^2}{\sqrt{1 + 2A_j^2 y}}. \tag{A.5}$$

This integral is more difficult. In fact we found that it is analytically solvable only if all three Gauss widths coincide, meaning we restrict ourselves to the special case of a spherically symmetric condensate in an analytic way. So if the Gauss widths are identical $A_1 = A_2 = A_3 = A$ we get

$$L_{\mathrm{N}} = \frac{uN^2}{\sqrt{2\pi}}\frac{1}{A}, \tag{A.6}$$

which coincides with the expression in Eq. (3.84). Keep in mind that with this expression we can only investigate radial oscillations as the breathing mode.

B. Detailed calculations for spherical condensates

B.1. Fourier transform of the interaction Lagrangian

In this appendix we briefly show the explicit derivation of the Fourier transformed Lagrangian used in Ch. 3. We start with the Lagrangian in position space, which is given by Eq. (3.22). As mentioned there, $n(\mathbf{r}) = |\Psi(\mathbf{r})|^2$ denotes the density. Inserting a Fourier transformation of the form in Eq. (3.23) for each component we obtain

$$L_{\mathrm{N}} = -\frac{1}{2}\int \mathrm{d}^3r \int \mathrm{d}^3r' \, \frac{1}{(2\pi)^3}\int \mathrm{d}^3k' \, \tilde{n}(\mathbf{k}')\mathrm{e}^{i\mathbf{k}'\cdot\mathbf{r}} \\ \times \frac{1}{(2\pi)^3}\int \mathrm{d}^3k \, \tilde{V}_{\mathrm{N}}(\mathbf{k})\mathrm{e}^{i\mathbf{k}\cdot(\mathbf{r}-\mathbf{r}')}\frac{1}{(2\pi)^3}\int \mathrm{d}^3k'' \, \tilde{n}(\mathbf{k}'')\mathrm{e}^{i\mathbf{k}''\cdot\mathbf{r}'}. \tag{B.1}$$

The integrals are rearranged, thus

$$L_{\mathrm{N}} = -\frac{1}{2}\frac{1}{(2\pi)^9}\int \mathrm{d}^3k \int \mathrm{d}^3k' \int \mathrm{d}^3k'' \, \tilde{n}(\mathbf{k}') \, \tilde{V}_{\mathrm{N}}(\mathbf{k}) \, \tilde{n}(\mathbf{k}'') \\ \times \int \mathrm{d}^3r \, \exp\{i(\mathbf{k}'+\mathbf{k})\cdot\mathbf{r}\}\int \mathrm{d}^3r' \, \exp\{i(\mathbf{k}''-\mathbf{k})\cdot\mathbf{r}'\}. \tag{B.2}$$

We evaluate the spatial integrals over r and r', which results in two δ-functions

$$L_{\mathrm{N}} = -\frac{1}{2}\frac{1}{(2\pi)^9}\int \mathrm{d}^3k \int \mathrm{d}^3k' \int \mathrm{d}^3k'' \, \tilde{n}(\mathbf{k}') \, \tilde{V}_{\mathrm{N}}(\mathbf{k}) \, \tilde{n}(\mathbf{k}'') \\ \times (2\pi)^3 \, \delta(\mathbf{k}'+\mathbf{k}) \cdot (2\pi)^3 \, \delta(\mathbf{k}''-\mathbf{k}). \tag{B.3}$$

This then simplifies to Eq. (3.24).

B.2. Newtonian interaction

Here we present the step-by-step calculations of the integrals appearing in in Sec. 3.2. We start with the calculations concerning the equilibrium cloud width, namely the function J_{N} defined in Eq. (3.40). There, we first present the solutions of the angular integrals, see (3.42) and show how to derive the following radial integral (3.43) resulting in (3.44). After that, we take a look into the calculations of the diagonal and off-diagonal elements of the Hessian matrix. Again, we give a step-by-step solution for both the angular and radial integrals in Eqs. (3.49) and (3.53). Since we assume throughout Sec. 3.2 spherical symmetry we apply the spherical coordinates given in Eq. (3.41).

Equilibrium cloud width

We have to evaluate the angular part of J_{N} given by

$$\int_0^{2\pi} \mathrm{d}\varphi \int_0^{\pi} \mathrm{d}\vartheta \, \sin\vartheta \, \kappa_j^2 \tag{B.4}$$

for each κ_j. By inserting them separately, we get for each component x, y and z a combination of trigonometric functions of varying order

$$\text{for } \kappa_x: \quad \kappa^2 \int_0^{2\pi} \mathrm{d}\varphi \, \cos^2\varphi \int_0^{\pi} \mathrm{d}\vartheta \, \sin^3\vartheta = \kappa^2 \, \pi \, \frac{4}{3}, \tag{B.5a}$$

$$\text{for } \kappa_y: \quad \kappa^2 \int_0^{2\pi} \mathrm{d}\varphi \, \sin^2\varphi \int_0^{\pi} \mathrm{d}\vartheta \, \sin^3\vartheta = \kappa^2 \, \pi \, \frac{4}{3}, \tag{B.5b}$$

$$\text{for } \kappa_z: \quad \kappa^2 \int_0^{2\pi} \mathrm{d}\varphi \int_0^{\pi} \mathrm{d}\vartheta \, \sin\vartheta \, \cos\vartheta = \kappa^2 \, 2\pi \, \frac{2}{3}. \tag{B.5c}$$

The corresponding solutions are also found in the literature, i.e. Ref. [108]. We see that all three integrals lead to the same result given in Eq. (3.42). This is expected as Newtonian gravity is a prominent example of a conservative force acting only in a radial direction.

With the angular part determined we now solve the remaining radial integral given in (3.43). Throughout the whole thesis we assume a Gaussian function as the wave function, so it is worth mentioning a special property of these functions. In particular,

the integrand can be rewritten in the following form

$$\kappa^2 \exp\left\{-\frac{1}{2}\gamma^2\kappa^2\right\} = -\frac{1}{\gamma}\partial_\gamma \exp\left\{-\frac{1}{2}\gamma^2\kappa^2\right\}, \tag{B.6}$$

as the derivative of an exponential function reproduces itself. Inserting this expression into the radial integral (3.43), allows us to switch the order of the integration over κ and the derivative with respect to γ, as they are independent variables. This leads us to

$$J_{\mathrm{N}} = \frac{4\pi}{3}\partial_\gamma \int_0^\infty \mathrm{d}\kappa \, \exp\left\{-\frac{1}{2}\gamma^2\kappa^2\right\}. \tag{B.7}$$

At this point, it is convenient to define a new function

$$K_{\mathrm{N}} = \int_0^\infty \mathrm{d}\kappa \, \exp\left\{-\frac{1}{2}\gamma^2\kappa^2\right\} \tag{B.8}$$

as the remaining radial integral. Although in this case it is a simple Gaussian integral, where the solution is well known as

$$K_{\mathrm{N}} = \sqrt{\frac{\pi}{2}}\frac{1}{\gamma}, \tag{B.9}$$

the structure of the definition of K_{N} becomes very useful in later calculations. As a preparation we then write Eq. (B.7) in a more compact form as

$$J_{\mathrm{N}} = \frac{4\pi}{3}\partial_\gamma K_{\mathrm{N}}, \tag{B.10}$$

which is easier to read. Inserting the solution of the Gaussian integral then immediately leads to the result given in Eq. (3.44).

Diagonal elements of the Hessian

Next, we solve the integrals in $J_{\mathrm{N}}^{(jj)}$ given in Eq. (3.49). This is necessary to determine the diagonal elements of the Hessian matrix. We start again with the angular integrals

$$\int_0^{2\pi} \mathrm{d}\varphi \int_0^\pi \mathrm{d}\vartheta \, \sin\vartheta \, \left(\gamma^2\kappa_j^4 - \kappa_j^2\right). \tag{B.11}$$

Using the linearity of the integral and inserting the spherical coordinates (3.41) we get

$$\begin{aligned}
\text{for } j = x: \quad & \gamma^2\kappa^4 \int_0^{2\pi} \mathrm{d}\varphi \, \cos^4\varphi \int_0^{\pi} \mathrm{d}\vartheta \, \sin^5\vartheta - \kappa^2 \int_0^{2\pi} \mathrm{d}\varphi \, \cos^2\varphi \int_0^{\pi} \mathrm{d}\vartheta \, \sin^3\vartheta \\
& = \gamma^2\kappa^4 \, \frac{3\pi}{4} \cdot \frac{16}{15} - \kappa^2 \, \pi \cdot \frac{4}{3}, \qquad \text{(B.12a)} \\
\text{for } j = y: \quad & \gamma^2\kappa^4 \int_0^{2\pi} \mathrm{d}\varphi \, \sin^4\varphi \int_0^{\pi} \mathrm{d}\vartheta \, \sin^5\vartheta - \kappa^2 \int_0^{2\pi} \mathrm{d}\varphi \, \sin^2\varphi \int_0^{\pi} \mathrm{d}\vartheta \, \sin^3\vartheta \\
& = \gamma^2\kappa^4 \, \frac{3\pi}{4} \cdot \frac{16}{15} - \kappa^2 \, \pi \cdot \frac{4}{3}, \qquad \text{(B.12b)} \\
\text{for } j = z: \quad & \gamma^2\kappa^4 \int_0^{2\pi} \mathrm{d}\varphi \int_0^{\pi} \mathrm{d}\vartheta \, \sin\vartheta \cos^4\vartheta - \kappa^2 \int_0^{2\pi} \mathrm{d}\varphi \int_0^{\pi} \mathrm{d}\vartheta \, \sin\vartheta \, \cos^2\vartheta \\
& = \gamma^2\kappa^4 \, 2\pi \cdot \frac{2}{5} - \kappa^2 \, 2\pi \cdot \frac{2}{3}. \qquad \text{(B.12c)}
\end{aligned}$$

Once more, all angular parts of the diagonal elements are equal as written in Eq. (3.50).

Analogue to the previous part we have to solve the radial integral

$$J_{\mathrm{N}}^{(jj)} = 4\pi \int_0^{\infty} \mathrm{d}\kappa \, \left(\frac{\gamma^2}{5}\kappa^4 - \frac{1}{3}\kappa^2 \right) \exp\left\{ -\frac{1}{2}\gamma^2\kappa^2 \right\}. \qquad \text{(B.13)}$$

We start by splitting the integrals into the sum of two parts. With the expression in (B.6) applied once for the first summand and twice for the second term we get

$$\begin{aligned}
J_{\mathrm{N}}^{(jj)} = 4\pi \Bigg\{ & -\frac{\gamma}{5}\partial_\gamma \left[-\frac{1}{\gamma}\partial_\gamma \left(\int_0^{\infty} \mathrm{d}\kappa \, \exp\left\{ -\frac{1}{2}\gamma^2\kappa^2 \right\} \right) \right] \\
& + \frac{1}{3\gamma}\partial_\gamma \left(\int_0^{\infty} \mathrm{d}\kappa \, \exp\left\{ -\frac{1}{2}\gamma^2\kappa^2 \right\} \right) \Bigg\}. \qquad \text{(B.14)}
\end{aligned}$$

For a more compact and clear expression, we use the function K_{N} introduced in Eq. (B.8) which results in

$$J_{\mathrm{N}}^{(jj)} = 4\pi \left[-\frac{\gamma}{5}\partial_\gamma \left(-\frac{1}{\gamma}\partial_\gamma K_{\mathrm{N}} \right) + \frac{1}{3\gamma}\partial_\gamma K_{\mathrm{N}} \right]. \qquad \text{(B.15)}$$

With the result of the Gaussian integral (B.9) we then get Eq. (3.51).

Off-diagonal elements of the Hessian

Lastly, we determine the integrals in $J_{\mathrm{N}}^{(jk)}$ for the off-diagonal elements of the Hessian matrix. The angular parts are

$$\int_0^{2\pi} \mathrm{d}\varphi \int_0^{\pi} \mathrm{d}\vartheta \ \sin\vartheta \, \kappa_j^2 \kappa_k^2 \tag{B.16}$$

for $j \neq k$. With the spherical coordinates (3.41) we get

$$\text{for } j = x, k = y: \quad \kappa^4 \int_0^{2\pi} \mathrm{d}\varphi \ \cos^2\varphi \ \sin^2\varphi \int_0^{\pi} \mathrm{d}\vartheta \ \sin^5\vartheta = \kappa^4 \ \frac{\pi}{4} \ \frac{16}{15}, \tag{B.17a}$$

$$\text{for } j = x, k = z: \quad \kappa^4 \int_0^{2\pi} \mathrm{d}\varphi \ \cos^2\varphi \int_0^{\pi} \mathrm{d}\vartheta \ \sin^3\vartheta \ \cos^2\vartheta = \kappa^4 \ \pi \ \frac{4}{15}, \tag{B.17b}$$

$$\text{for } j = y, k = z: \quad \kappa^4 \int_0^{2\pi} \mathrm{d}\varphi \ \sin^2\varphi \int_0^{\pi} \mathrm{d}\vartheta \ \sin^2\vartheta \ \cos^2\vartheta = \kappa^4 \ \pi \ \frac{4}{15}. \tag{B.17c}$$

The remaining elements give the same results, respectively, as the product in (B.16) commutes. With this Eq. (3.54) is proven. Furthermore, this then leads to the radial integral

$$J_{\mathrm{N}}^{(jk)} = \frac{4\pi}{15}\gamma^2 \int_0^{\infty} \mathrm{d}\kappa \ \kappa^4 \exp\left\{-\frac{1}{2}\gamma^2\kappa^2\right\} \tag{B.18}$$

and after applying (B.6) twice

$$J_{\mathrm{N}}^{(jk)} = -\frac{4\pi}{15}\gamma\partial_\gamma \left[-\frac{1}{\gamma}\partial_\gamma \left(\int_0^{\infty} \mathrm{d}\kappa \ \exp\left\{-\frac{1}{2}\gamma^2\kappa^2\right\}\right)\right], \tag{B.19}$$

respectively. For completeness, we show here the expression for $J_{\mathrm{N}}^{(jk)}$ depending on K_{N}

$$J_{\mathrm{N}}^{(jk)} = -\frac{4\pi}{15}\gamma\partial_\gamma \left(-\frac{1}{\gamma}\partial_\gamma K_{\mathrm{N}}\right). \tag{B.20}$$

Using the solution of the Gaussian integral (B.9) and performing both derivatives with respect to γ leads to the expression given in Eq. (3.55).

B.3. Yukawa-like interaction

In this part we solve the radial integrals for the Yukawa-like potential treated in Sec. 3.3. As mentioned there, the angular parts are identical to the results derived in the Appendix B.2 for the Newtonian case, since the gravitational potentials do not depend on the angles. Analogous to the previous section we calculate the integrals (3.72) for the equilibrium cloud width and (3.76) and (3.79) for the diagonal and off-diagonal elements of the Hessian matrix.

Starting with Eq. (3.72), we rewrite the integral using (B.6) twice as follows

$$J_{\mathrm{Yuk}} = \frac{4\pi}{3}\partial_\gamma \left[-\frac{1}{\gamma}\partial_\gamma \left(\int_0^\infty \mathrm{d}\kappa \, \frac{\alpha}{\kappa^2 + \bar{\lambda}^{-2}} \exp\left\{ -\frac{1}{2}\gamma^2\kappa^2 \right\} \right) \right]. \tag{B.21}$$

Again, we define the integral as a function K_{Yuk}, which reads this time

$$K_{\mathrm{Yuk}} = \int_0^\infty \mathrm{d}\kappa \, \frac{\alpha}{\kappa^2 + \bar{\lambda}^{-2}} \exp\left\{ -\frac{1}{2}\gamma^2\kappa^2 \right\}. \tag{B.22}$$

According to Ref. [108], Eq. (3.466) this integral is solved by

$$K_{\mathrm{Yuk}} = \alpha \frac{\pi}{2}\bar{\lambda} \, \exp\left\{ \frac{\gamma^2}{2\bar{\lambda}^2} \right\} \mathrm{erfc}\left[\sqrt{\frac{\gamma^2}{2\bar{\lambda}^2}} \right]. \tag{B.23}$$

The function $\mathrm{erfc}(x)$ is called the complementary error function. It is commonly defined by $\mathrm{erfc}(x) = 1 - \mathrm{erf}(x)$, where the error function itself is defined by a Gaussian integral as follows

$$\mathrm{erf}(x) = \frac{2}{\sqrt{\pi}} \int_0^x \mathrm{d}t \, \mathrm{e}^{-t^2}, \tag{B.24}$$

see for example Ref. [132]. As a consequence, it is possible to express the complementary error function as

$$\mathrm{erfc}(x) = \frac{2}{\sqrt{\pi}} \int_x^\infty \mathrm{d}t \, \mathrm{e}^{-t^2}. \tag{B.25}$$

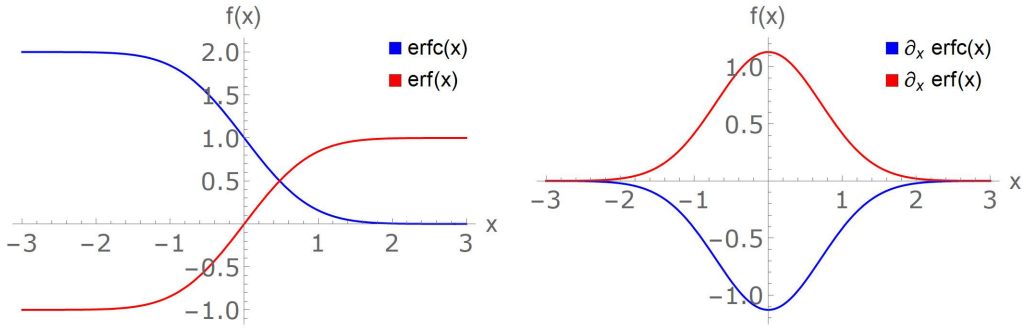

Figure B.1.: Error function and complementary error function (left) as well as their derivatives (right) depending on their argument.

Hence, the derivatives are simply given by Gaussian function

$$\partial_x \operatorname{erf}(x) = \frac{2}{\sqrt{\pi}} \mathrm{e}^{-x^2}, \tag{B.26a}$$

$$\partial_x \operatorname{erfc}(x) = -\frac{2}{\sqrt{\pi}} \mathrm{e}^{-x^2}. \tag{B.26b}$$

In Fig. B.1 we show both the error functions and their derivatives. Here, we are especially interested in the complementary error function $\operatorname{erfc}(x)$. As seen in the pictures, the image of the function is restricted between the values 0 and 2. The derivative shows a Gaussian with negative sign around the center in accordance to the analytic expression (B.26b).

Back to our calculations of the equilibrium cloud width we mention the expression for J_{Yuk} (B.21), which depends on the function K_{Yuk}

$$J_{\mathrm{Yuk}} = \frac{4\pi}{3} \partial_\gamma \left(-\frac{1}{\gamma} \partial_\gamma K_{\mathrm{Yuk}} \right), \tag{B.27}$$

although it is in principle not needed here as we know the analytic solution (B.23). Nevertheless, this formal structure will become very useful and easier to read in later calculations. Inserting (B.23) into the equation above and calculating the first derivative leads to an expression with both exponential and complementary error function as well as a constant $-\sqrt{\frac{2}{\pi}}\frac{1}{\lambda}$. We multiply the result by γ^{-1} and calculate the next derivative analogously. This finally results in Eq. (3.73).

The next integral is given in Eq. (3.76) for the diagonal elements of the Hessian matrix.

Here, we have to use (B.6) three times for the first part and twice for the second part to reduce the integral to that in Eq. (B.23). Thus with the function K_{Yuk} we have

$$J_{\mathrm{Yuk}}^{(jj)} = \alpha\, 4\pi \left[-\frac{\gamma}{5}\partial_\gamma \left[-\frac{1}{\gamma}\partial_\gamma \left(-\frac{1}{\gamma}\partial_\gamma K_{\mathrm{Yuk}} \right) \right] + \frac{1}{3\gamma}\partial_\gamma \left(-\frac{1}{\gamma}\partial_\gamma K_{\mathrm{Yuk}} \right) \right]. \tag{B.28}$$

Using Eq. (B.23), leads to the result in Eq. (3.77).

And finally we derive the radial integral in Eq. (3.79) for the off-diagonal elements of the Hessian matrix. Again we apply (B.6) three times and use the short-notation with the function K_{Yuk}

$$J_{\mathrm{Yuk}}^{(jk)} = -\alpha\, \frac{4\pi}{15}\gamma\partial_\gamma \left[-\frac{1}{\gamma}\partial_\gamma \left(-\frac{1}{\gamma}\partial_\gamma K_{\mathrm{Yuk}} \right) \right]. \tag{B.29}$$

With (B.23) the calculation is quite similar to the previous one and results in Eq. (3.80).

B.4. Analytic expression for the frequency of the breathing mode for Yukawa interaction

Since the analytic expressions for the eigenvalues of the Hessian matrix in Eq. (3.82) are too complicated and too long to write down, we show in this section a simplified calculation to derive a compact expression at least for the collective frequency of the breathing mode.

We start with the Lagrangian for the Yukawa-like interaction given in Eq. (3.66). The breathing mode of a spherical condensate describes a radial oscillation around the center of the condensate, which means that in all three spatial dimensions the variation of the respective Gauss width are identical and oscillate in phase to the others. In this special case we can safely assume the dimensionless Gauss widths themselves to be equal, thus $\gamma_x = \gamma_y = \gamma_z = \gamma$. The Lagrangian then reads in spherical coordinates as follows

$$\begin{aligned} L_{\mathrm{Yuk}} =& \frac{uN^2}{(2\pi)^2}\sqrt{\frac{m\omega}{\hbar}} \\ & \cdot \int_0^\infty \mathrm{d}\kappa \int_0^{2\pi} \mathrm{d}\varphi \int_0^\pi \mathrm{d}\vartheta\, \kappa^2 \sin\vartheta \left(\frac{1}{\kappa^2} + \frac{\alpha}{\kappa^2 + \bar{\lambda}^{-2}} \right) \exp\left\{ -\frac{1}{2}\gamma^2\kappa^2 \right\}. \end{aligned} \tag{B.30}$$

The angular part is trivial and the radial integration consists of a simple Gauss inte-

gral and a part, which is solved with (B.6) and (B.23). Consequently, we get for the Lagrangian

$$L_{\mathrm{Yuk}} = \frac{1}{\sqrt{2\pi}} u N^2 \sqrt{\frac{m\omega}{\hbar}} \left(\frac{1}{\gamma} + \alpha \frac{1}{\gamma} - \alpha \sqrt{\frac{\pi}{2}} \frac{1}{\bar{\lambda}} \exp\left\{ \frac{\gamma^2}{2\bar{\lambda}^2} \right\} \mathrm{erfc}\left[\sqrt{\frac{\gamma^2}{2\bar{\lambda}^2}} \right] \right). \tag{B.31}$$

With this expression we define an effective potential with Eq. (2.37), including the contact interaction, the Newtonian, and the Yukawa-like interaction

$$V_{\mathrm{eff}} = 3 \left(\frac{\nu^2}{2} \gamma^2 + \frac{1}{2\gamma^2} \right) + \frac{P}{\gamma^3} - \frac{3Q}{\gamma} - 3\alpha Q \left(\frac{1}{\gamma} - \sqrt{\frac{\pi}{2}} \frac{1}{\bar{\lambda}} \exp\left\{ \frac{\gamma^2}{2\bar{\lambda}^2} \right\} \mathrm{erfc}\left[\sqrt{\frac{\gamma^2}{2\bar{\lambda}^2}} \right] \right), \tag{B.32}$$

where $\nu_x = \nu_y = \nu_z = \nu$ due to spherical symmetry. As mentioned in Ch. 2 in the Taylor expansion of the effective potential the first derivative is set to zero and thus defines an equation for the equilibrium cloud width γ_0, which is identical to Eq. (3.75). The second derivative of the effective potential (B.32) leads to the collective frequency of the breathing mode

$$\begin{aligned} \left(\frac{\Omega_{\mathrm{br}}}{\omega} \right)^2 = \nu^2 &+ \frac{3}{\gamma_0^4} + \frac{4P}{\gamma_0^5} - \frac{2Q}{\gamma_0^3} \\ &- 2\alpha Q \left[\frac{1}{\gamma_0^3} + \frac{\gamma_0}{2\bar{\lambda}^4} - \sqrt{\frac{\pi}{2}} \left(\frac{1}{2\bar{\lambda}^3} + \frac{\gamma_0^2}{2\bar{\lambda}^5} \right) \exp\left\{ \frac{\gamma_0^2}{2\bar{\lambda}^2} \right\} \mathrm{erfc}\left[\frac{\gamma_0}{\sqrt{2}\bar{\lambda}} \right] \right]. \end{aligned} \tag{B.33}$$

In Fig. B.2 we show a comparison between the analytic formula given by Eq. (B.33) and the results presented in Sec. 3.3.3. We compare the difference to the Newtonian case from 1 Hz to 5 Hz of the collective frequency of the breathing mode. As expected the curves completely overlap, so (B.33) is indeed an analytic expression for the frequency of the breathing mode.

Note that the Lagrangian (B.31) treated in this section does not allow a variation of the three Gauss widths independently and thus cannot be used to derive for example quadrupole frequencies. This is why we chose a more general calculation in Ch. 3. However, with this simplified version we found an analytic expression for the collective frequency of the breathing mode and furthermore, we are able to roughly estimate the order of magnitude of the interaction energy of a Yukawa-like potential, which is used

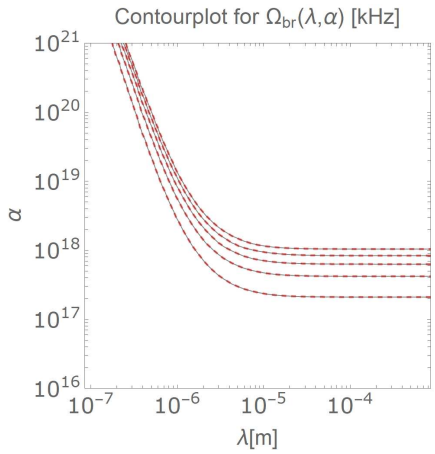

Figure B.2.: Contourplot for the collective frequency of the breathing mode: comparison between the results of Sec 3.3.3 (black) and the analytic expression in Eq. (B.33) (red dashed). The lines indicate a difference of 1 Hz to 5 Hz compared to the Newtonian case given in Eq. (3.63) analogue to Fig. 3.6.

in Sec. 3.3.3 to determine viable values for the interaction strength α.

C. Detailed calculations for axially symmetric condensates

In this part of the appendix we focus on solving the appearing integrals in Ch. 4 treating the axially symmetric condensates. In contrast to the previous part, App. B we apply cylindrical coordinates given in Eq. (4.10).

C.1. Newtonian interaction

In the first part we give a detailed calculation for the integrals including Newtonian interaction as described in Sec. 4.2. As usual we start with the function $J_{\mathrm{N}}^{(j)}$ now, however, in axial symmetry defined in Eq. (4.11) and explain all necessary steps to derive the ordinary differential equations for γ_t and γ_z, shown in Eqs. (4.16). After that, we solve the integrals in $J_{\mathrm{N}}^{(jj)}$ and $J_{\mathrm{N}}^{(jk)}$, see Eqs. (4.18) and (4.19), respectively, to get the expressions for the diagonal and off-diagonal elements of the Hessian matrix.

Equilibrium cloud width

The expression $J_{\mathrm{N}}^{(j)}$ in Eq. (4.11) includes the cylindrical coordinate κ_j given in Eq. (4.10). In order to explicitly solve the integrals we treat the different cases for j separately. Hence, let us start with $j = x$. The integral over the angular part φ is very easy and gives a factor π, as we have already seen in App. B.2. The integral over κ_ρ needs a bit more attention. First, we apply the identity (B.6)

$$\int_0^\infty \mathrm{d}\kappa_\rho \, \frac{\kappa_\rho^3}{\kappa_\rho^2 + \kappa_z^2} \exp\left\{-\frac{1}{2}\gamma_t^2\kappa_\rho^2\right\} = -\frac{1}{2}\partial_{\gamma_t} \int_0^\infty \mathrm{d}\kappa_\rho \, \frac{\kappa_\rho}{\kappa_\rho^2 + \kappa_z^2} \exp\left\{-\frac{1}{2}\gamma_t^2\kappa_\rho^2\right\}. \tag{C.1}$$

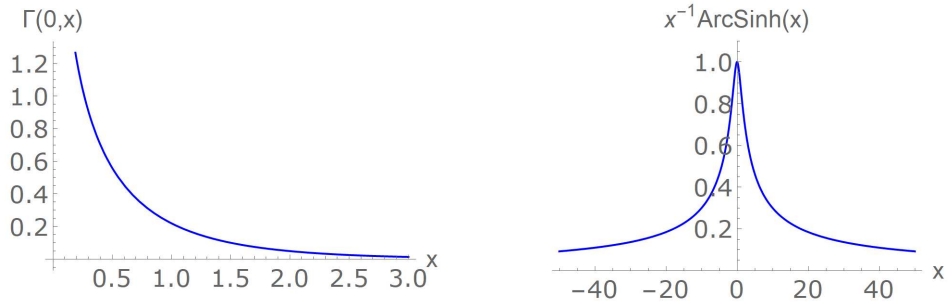

Figure C.1.: Incomplete gamma function $\Gamma(0, x)$ (left) and $x^{-1}\text{arcsinh}(x)$ (right) depending on its argument.

Here, we substitute

$$v = \frac{1}{2}\gamma_t^2\kappa_\rho^2 \quad \Rightarrow \quad \mathrm{d}v = \gamma_t^2\kappa_\rho \mathrm{d}\kappa_\rho, \tag{C.2}$$

which leads to

$$-\frac{1}{\gamma_t}\partial_{\gamma_t}\int_0^\infty \mathrm{d}v\ \frac{1}{\gamma_t^2}\frac{1}{\frac{2v}{\gamma_t^2}+\kappa_z^2}\mathrm{e}^{-v} = -\frac{1}{\gamma_t}\partial_{\gamma_t}\left(\frac{1}{2}\int_0^\infty \mathrm{d}v\ \frac{1}{v+\frac{1}{2}\gamma_t^2\kappa_z^2}\mathrm{e}^{-v}\right). \tag{C.3}$$

We label the second summand in the denominator as ξ^2 as defined in Eq. (4.13). Note that ξ^2 is always positive. Next, we use another substitution

$$w = v + \xi^2 \quad \Rightarrow \quad \mathrm{d}w = \mathrm{d}v \tag{C.4}$$

to get

$$-\frac{1}{\gamma_t}\partial_{\gamma_t}\left(\frac{1}{2}\int_{\xi^2}^\infty \mathrm{d}w\ \frac{1}{w}\mathrm{e}^{-w}\right)\mathrm{e}^{+\xi^2} = -\frac{1}{\gamma_t}\partial_{\gamma_t}\left[\frac{1}{2}\,\Gamma(0,\xi^2)\mathrm{e}^{\xi^2}\right]. \tag{C.5}$$

Here, we introduced the incomplete gamma function $\Gamma(0, x)$ with its definition given in the expression above inside the brackets. We present this function also in Fig. C.1 on the left side. It is a monotonically decreasing function with a singularity at $x = 0$ while approaching zero in the limit $x \to \infty$. Thus the function itself has no roots and is always positive.

So far, with Eq. (C.5) the function $J_{\mathrm{N}}^{(x)}$ reads

$$J_{\mathrm{N}}^{(x)} = \pi \int_{-\infty}^{\infty} \mathrm{d}\kappa_z \, \exp\left\{-\frac{1}{2}\gamma_z^2\kappa_z^2\right\} \partial_{\gamma_t}\left[\frac{1}{2}\Gamma(0,\xi^2)\mathrm{e}^{\xi^2}\right]. \tag{C.6}$$

Note that ξ^2 also depends on κ_z according to its definition (4.13). Now, we define the integral as a function K_{N} as given in Eq. (4.14). With that J_{N} gets a compact form

$$J_{\mathrm{N}}^{(x)} = \pi \, \partial_{\gamma_t} K_{\mathrm{N}}. \tag{C.7}$$

For better readability we use this expression, although the integral in K_{N} in Eq. (4.14) can be solved. The program Mathematica returns as a result

$$K_{\mathrm{N}} = \frac{\sqrt{2\pi}}{\sqrt{\gamma_z^2 - \gamma_t^2}} \operatorname{arcsinh}\sqrt{\frac{\gamma_z^2 - \gamma_t^2}{\gamma_t^2}}, \tag{C.8}$$

which can easily be formulated as Eq. (4.15). The function of the type $x^{-1}\mathrm{arcsinh}(x)$ occurring there is shown schematically in Fig. C.1 on the right side. As we can see, it is finite and positive everywhere. In particular, the center at $x = 0$ is of interest as it corresponds in our model to the spherical limit. There, the function takes the value 1 as discussed in Sec. 4.2. Otherwise, it is decreasing and slowly approaching zero for both limits $x \to \pm\infty$.

The calculation for $j = y$ is identical, since the angular integration gives again a factor π.

In case of $j = z$ the integrals slightly differ. The function $J_{\mathrm{N}}^{(z)}$ specifically reads

$$J_{\mathrm{N}}^{(z)} = -\gamma_z \int_{-\infty}^{\infty} \mathrm{d}\kappa_z \left(\int_0^{\infty} \mathrm{d}\kappa_\rho \int_0^{2\pi} \mathrm{d}\varphi \, \frac{\kappa_\rho \kappa_z^2}{\kappa_\rho^2 + \kappa_z^2} \exp\left\{-\frac{1}{2}\gamma_t^2\kappa_\rho^2\right\}\right) \exp\left\{-\frac{1}{2}\gamma_z^2\kappa_z^2\right\}. \tag{C.9}$$

The angular integral gives a factor 2π and the integral over κ_ρ is formulated in terms of the incomplete Gamma function analogue to (C.5) but without any derivatives. This leads to

$$J_{\mathrm{N}}^{(z)} = -2\pi\gamma_z \int_{-\infty}^{\infty} \mathrm{d}\kappa_z \, \kappa_z^2 \, \frac{1}{2}\Gamma\left(0,\xi^2\right) \mathrm{e}^{\xi^2} \exp\left\{-\frac{1}{2}\gamma_z^2\kappa_z^2\right\}. \tag{C.10}$$

In order to get rid of κ_z^2 in the integrand, we apply (B.6) and write J_N depending on the function K_N as

$$J_\mathrm{N}^{(z)} = 2\pi\, \partial_{\gamma_z} K_\mathrm{N}. \tag{C.11}$$

Note that Eq. (C.11) has an additional factor 2 in comparison with (C.7).

As all three components of $J_\mathrm{N}^{(j)}$ are determined, we now take a look at the additional term in the ODEs. With the prefactors in the general equations for the ODE (2.34) and the Lagrangian (3.36) we have

$$\frac{1}{N}\frac{2}{\hbar\omega}\, \partial_{\gamma_j} L_\mathrm{Yuk} = \frac{2}{(2\pi)^2}\frac{uN}{\hbar\omega}\sqrt{\frac{m\omega}{\hbar}}\, J_\mathrm{N}^{(j)}. \tag{C.12}$$

Inserting (C.7) and (C.11) and using the definition of the gravitational interaction strength Q in (3.46) we finally get the ODEs in Eqs. (4.16).

Hessian matrix

To derive the collective frequencies of the condensate, it is necessary to know the Hessian matrix M. By construction the matrix depends on the integral function $J_\mathrm{N}^{(jj)}$ and $J_\mathrm{N}^{(jk)}$ shown for axial symmetry in Eqs. (4.18) and (4.19). In the following we solve the integrals for all needed cases. With the knowledge of the previous part, the procedure itself is straightforward and all important steps like introducing the incomplete gamma function were already mentioned. It is also similar to the spherical case discussed in App. B.2.

The first contribution is $J_\mathrm{N}^{(xx)}$, for which we insert κ_x from Eq. (4.10) into (4.18). The angular integral over φ

$$\int_0^{2\pi} \mathrm{d}\varphi\, \left(\gamma_t^2\kappa_\rho^4\cos^4\varphi - \kappa_\rho^2\cos^2\varphi\right) = \frac{3}{4}\pi\gamma_t^2\kappa_\rho^4 - \pi\kappa_\rho^2 \tag{C.13}$$

can be looked up in the literature. For the following κ_ρ integral we have to apply (B.6) twice for the first summand due to the factor κ_ρ^4 and once for the second summand

because of κ_ρ^2. Including the third integral, we thus get

$$J_{\mathrm{N}}^{(xx)} = \frac{3}{4}\pi\gamma_t\ \partial_{\gamma_t}\left(\frac{1}{\gamma_t}\partial_{\gamma_t}K_{\mathrm{N}}\right) + \frac{\pi}{\gamma_t}\partial_{\gamma_t}\ K_{\mathrm{N}}. \tag{C.14}$$

As expected for cylindrical symmetry it turns out that $J_{\mathrm{N}}^{(yy)}$ leads to the same result.

The third diagonal element $J_{\mathrm{N}}^{(zz)}$ gives a factor 2π from the integration over φ and because of κ_z^4 and κ_z^2 in the integrand we have to use (B.6) up to two times now with respect to γ_z. The result is

$$J_{\mathrm{N}}^{(zz)} = 2\pi\gamma_z\ \partial_{\gamma_z}\left(\frac{1}{\gamma_z}\partial_{\gamma_z}K_{\mathrm{N}}\right) + \frac{2\pi}{\gamma_z}\partial_{\gamma_z}\ K_{\mathrm{N}}. \tag{C.15}$$

Now for the off diagonal elements we start with Eq. (4.19). Again the angular integral is fairly easy

$$\int_0^{2\pi} \mathrm{d}\varphi\ \kappa_\rho^4 \cos^2\varphi\ \sin^2\varphi = \frac{\pi}{4}\kappa_\rho^4, \tag{C.16}$$

such that we have to apply (B.6) twice with respect to γ_t. This immediately leads to

$$J_{\mathrm{N}}^{(xy)} = \frac{\pi}{4}\gamma_t\ \partial_{\gamma_t}\left(\frac{1}{\gamma_t}\partial_{\gamma_t}K_{\mathrm{N}}\right). \tag{C.17}$$

The last part is $J_{\mathrm{N}}^{(xz)}$. The integration over φ gives a factor π and the remaining integrals read

$$J_{\mathrm{N}}^{(xz)} = \pi\gamma_t\gamma_z \int_{-\infty}^{\infty}\mathrm{d}\kappa_z \int_0^{\infty}\mathrm{d}\kappa_\rho\ \frac{\kappa_\rho^3\kappa_z^2}{\kappa_\rho^2+\kappa_z^2}\exp\left\{-\frac{1}{2}\gamma_t^2\kappa_\rho^2\right\}\exp\left\{-\frac{1}{2}\gamma_z^2\kappa_z^2\right\}. \tag{C.18}$$

Here we use (B.6) once with respect to γ_t and once with respect to γ_z, which results in the mixed second derivative

$$J_{\mathrm{N}}^{(xz)} = \pi\ \partial_{\gamma_t}\partial_{\gamma_z}K_{\mathrm{N}}. \tag{C.19}$$

Again due to the symmetry $J_{\mathrm{N}}^{(yz)}$ yields the same result. With all contributions $J_{\mathrm{N}}^{(jj)}$ and $J_{\mathrm{N}}^{(jk)}$ given in Eqs. (C.14), (C.15), (C.17), and (C.18) we then determine the elements of the Hessian matrix M according to the general form of M in Eq. (2.42). This then

leads to Eqs. (4.20) and (4.21).

C.2. Yukawa-like interaction

Here, we will quickly go through the calculations dedicated to the Yukawa-like interaction in axially symmetric condensates described in Sec. 4.3. We explicitly show the difference in the formulas compared to the Newtonian results from the previous part.

Starting with the integral function $J^{(j)}_{\mathrm{Yuk}}$ given in Eq. (4.25), we immediately notice the change in the denominator caused the finite size of the effective range λ, see also the Fourier transform of the Yukawa potential (3.65). With the cylindrical coordinates κ_j of Eq. (4.10) the appearing integrals over φ is identical to the Newtonian case for each j. However, the κ_ρ integrals slightly differs, as shown here for $j = x$

$$J^{(x)}_{\mathrm{Yuk}} = -\pi\gamma_t \int_{-\infty}^{\infty} \mathrm{d}\kappa_z \left(\int_0^{\infty} \mathrm{d}\kappa_\rho \, \frac{\alpha\kappa_\rho^3}{\kappa_\rho^2 + \kappa_z^2 + \bar{\lambda}^{-2}} \exp\left\{ -\frac{1}{2}\gamma_t^2\kappa_\rho^2 \right\} \right) \exp\left\{ -\frac{1}{2}\gamma_z^2\kappa_z^2 \right\}. \tag{C.20}$$

With the identity (B.6) and the same substitution (C.2) for the argument of the exponential function the integral in the brackets is written as

$$\begin{aligned} \int_0^{\infty} \mathrm{d}\kappa_\rho \, \frac{\alpha\kappa_\rho^3}{\kappa_\rho^2 + \kappa_z^2 + \bar{\lambda}^{-2}} \exp\left\{ -\frac{1}{2}\gamma_t^2\kappa_\rho^2 \right\} = \\ - \alpha\frac{1}{\gamma_t}\partial_{\gamma_t} \left(\frac{1}{2} \int_0^{\infty} \mathrm{d}v \, \frac{1}{v + \frac{1}{2}\gamma_t^2 \left(\kappa_z^2 + \bar{\lambda}^{-2}\right)} \mathrm{e}^{-v} \right). \end{aligned} \tag{C.21}$$

The denominator still contains the effective range of the Yukawa interaction. We now define the second summand in the denominator as ξ'^2 shown in Eq. (4.26). The next substitution analogue to (C.4) then includes ξ' instead of ξ, such that

$$-\alpha\frac{1}{\gamma_t}\partial_{\gamma_t} \left(\frac{1}{2} \int_0^{\infty} \mathrm{d}v \, \frac{1}{v + \frac{1}{2}\gamma_t^2 \left(\kappa_z^2 + \bar{\lambda}^{-2}\right)} \mathrm{e}^{-v} \right) = -\alpha\frac{1}{\gamma_t}\partial_{\gamma_t} \left[\frac{1}{2} \, \Gamma(0, \xi'^2) \mathrm{e}^{\xi'^2} \right]. \tag{C.22}$$

Including the integral over κ_z of Eq. (C.20), we define the function K_{Yuk} as in Eq. (4.27),

such that we finally get the compact form

$$J^{(x)}_{\mathrm{Yuk}} = \pi\ \alpha\ \partial_{\gamma_t} K_{\mathrm{Yuk}}. \tag{C.23}$$

Unfortunately, as mentioned in Sec. 4.3, we cannot analytically solve K_{Yuk} in contrast to K_{N}.

From this point on, the calculations of the remaining integrals of $J^{(j)}_{\mathrm{Yuk}}$ as well as $J^{(jj)}_{\mathrm{Yuk}}$ and $J^{(jk)}_{\mathrm{Yuk}}$ are formally identical to App. C.1. In fact, as Eq. (C.23) already suggests, we simply need to replace K_{N} by the product αK_{Yuk} in all expressions. The ODE in Eqs. (4.28) and the elements of the Hessian matrix in Eqs. (4.32) and (4.33) in case of the Yukawa interaction thus immediately follows.

D. Detailed calculations for the rational potential

In this part of the appendix we show the detailed calculations of Ch. 5. In particular, we first prove that the expression (5.12) given in Ref. [120] for the Fourier transform of the distribution $r^{-1-\epsilon}$ can be simplified into Eq. (5.10). We then follow the procedure of App. B.3 and present the solutions of the integrals occurring in Eq. (5.16) to determine an expression for the equilibrium cloud width γ_0 and in Eqs. (5.20) and (5.21) for the Hessian matrix M. Furthermore, we explicitly break down the calculations to reach the results in Eqs. (5.18) and (5.24).

The first part treats the Fourier transform of $r^{-1-\epsilon}$, which as mentioned is given by (5.12) in general. We rewrite this result with the following identities of the gamma function:

$$\text{recurrence}: \ \Gamma(z+1) = z\Gamma(z), \tag{D.1a}$$

$$\text{reflection}: \ \Gamma(z)\Gamma(1-z) = \frac{\pi}{\sin(\pi z)}, \tag{D.1b}$$

$$\text{duplication}: \ \Gamma(2z) = \frac{1}{\sqrt{2\pi}}\, 2^{2z-\frac{1}{2}}\Gamma(z)\Gamma\left(z+\frac{1}{2}\right), \tag{D.1c}$$

see Ref. [133], p. 256. With the duplication formula (D.1c) we show that

$$\Gamma(1-\epsilon) = \frac{1}{\sqrt{2\pi}}\, 2^{\frac{1}{2}-\epsilon}\Gamma\left(\frac{1-\epsilon}{2}\right)\Gamma\left(\frac{2-\epsilon}{2}\right). \tag{D.2}$$

Solving this for $\Gamma((2-\epsilon)/2)$ and inserting into Eq. (5.12) leads to the Fourier transform

$$\mathcal{F}\left[r^{-1-\epsilon}\right] = 4\pi^2 \frac{1}{\Gamma\left(\frac{1+\epsilon}{2}\right)\Gamma\left(\frac{1-\epsilon}{2}\right)}\,\Gamma(1-\epsilon)\frac{1}{k^{2-\epsilon}}. \tag{D.3}$$

We rewrite the denominator as

$$\Gamma\left(\frac{1-\epsilon}{2}\right)\Gamma\left(\frac{1+\epsilon}{2}\right) = \Gamma\left(\frac{1-\epsilon}{2}\right)\Gamma\left(1-\frac{1-\epsilon}{2}\right) \tag{D.4}$$

and apply the reflection formula (D.1b) as well as replace the sine function by the cosine function. This then leads to Eq. (5.13) and the statement is proven.

Next, we solve the integral in (5.16). With Eq. (B.6) it follows

$$\int_0^\infty \mathrm{d}\kappa\, \kappa^{2+\epsilon} \exp\left\{-\frac{1}{2}\gamma^2\kappa^2\right\} = -\frac{1}{\gamma}\partial_\gamma \int_0^\infty \mathrm{d}\kappa\, \kappa^{\epsilon} \exp\left\{-\frac{1}{2}\gamma^2\kappa^2\right\}. \tag{D.5}$$

This integral is found in the literature, i.e. in Ref. [108], p. 347,

$$\int_0^\infty \mathrm{d}\kappa\, \kappa^{\epsilon} \exp\left\{-\frac{1}{2}\gamma^2\kappa^2\right\} = \frac{1}{2}\sqrt{2^{\epsilon-1}}\,\Gamma\left(\frac{\epsilon+1}{2}\right)\frac{1}{\gamma^{1+\epsilon}} \tag{D.6}$$

if $\mathrm{Re}(\epsilon) > -3$. Calculating the derivative with respect to γ is straightforward and we simplify the result with the recurrence formula (D.1a), such that Eq. (5.17) immediately follows, as well as the ODE (5.18) for the cloud width.

Finally, we calculate the integrals in (5.20) and (5.21) to determine the Hessian matrix. In both expressions the same integral occurs, where we apply (B.6) twice. This yields

$$\int_0^\infty \mathrm{d}\kappa\, \kappa^{4+\epsilon} \exp\left\{-\frac{1}{2}\gamma^2\kappa^2\right\} = \sqrt{2^{\epsilon+3}}\Gamma\left(\frac{\epsilon+5}{2}\right)\frac{1}{\gamma^{5+\epsilon}}. \tag{D.7}$$

Eq. (5.23) for the off-diagonal elements is thus already proven. For the expression of the diagonal elements (5.22) we get the intermediate result

$$\begin{aligned} J_{\mathrm{rat}}^{(jj)} =& \alpha\bar{\lambda}^\epsilon \cos\left(\frac{\pi}{2}\epsilon\right)\Gamma(1-\epsilon) \\ &\times 4\pi\left[\frac{\gamma^2}{5}\sqrt{2^{\epsilon+3}}\,\Gamma\left(\frac{\epsilon+5}{2}\right)\frac{1}{\gamma^{5+\epsilon}} - \frac{1}{3}\sqrt{2^{\epsilon+1}}\,\Gamma\left(\frac{\epsilon+3}{2}\right)\frac{1}{\gamma^{3+\epsilon}}\right]. \end{aligned} \tag{D.8}$$

Using the recurrence formula (D.1a) for the first summand backwards leads to Eq. (5.22). The matrix elements $M^{(jj)}$ and $M^{(jk)}$ in Eq. (5.24) follow analogue to the Yukawa case.

E. Effective potentials

In this appendix we investigate the effective potentials of the interactions discussed in this thesis. We have defined the effective potentials in Eq. (2.36) in Sec. 2.3, such that the acceleration terms of the differential equations are equal to the negative derivative with respect to the Gaussian width of said potential. It is often used to find bound states or to investigate the stability of a system. In particular, searching for the minimum of this potential is an alternative way to find the equilibrium cloud width.

The general form of the effective potential is mentioned in Eq. (2.37) depending on the Lagrangian of the two-particle interaction. In the following we explicitly derive the effective potential for each considered interaction in spherically symmetric condensates. We begin with the contact interaction followed by the Newtonian interaction and discuss the influence of both contact interaction strength and gravitational interaction strength. After that, we take a look into the Yukawa-like interaction with both parameters and finish this section with an interaction caused by a rational potential.

According to Eq. (2.37) we need an expression for the Lagrangian L_{int}. In case of the contact interaction we already know the general form, which is given in Eq. (3.4). When we assume spherical symmetry this simplifies to

$$L_{\text{con}}\left(\sqrt{\frac{\hbar}{m\omega}}\gamma\right) = -\frac{gN^2}{2\sqrt{(2\pi)^3}}\left(\sqrt{\frac{m\omega}{\hbar}}\right)^3 \frac{1}{\gamma^3}. \tag{E.1}$$

Inserting this into the general form of the effective potential (2.37) leads to

$$V_{\text{eff}}^{(\text{con})} = \frac{3}{2}\left(\gamma^2 + \frac{1}{\gamma^2}\right) + \frac{P}{\gamma^3} \tag{E.2}$$

for spherical condensates with $\nu = 1$. Here we used the contact interaction strength P defined in Eq. (3.6). The minimum of this function can be calculated numerically.

In Fig. E.1 on the left side we present the effective potential for the contact interaction

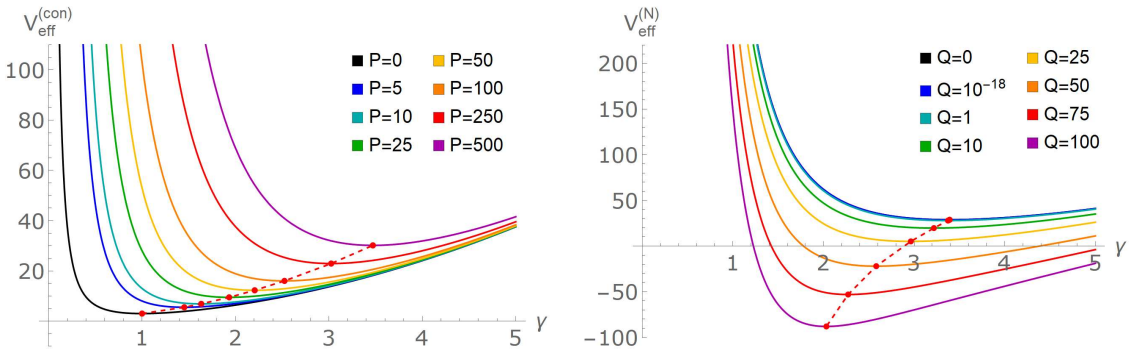

Figure E.1.: Effective potential for the contact interaction (left) and the Newtonian interaction (right) depending on the corresponding interaction strengths P and Q. For the Newtonian interaction we choose $P = 446$. The red dots indicate the minimum of each curve.

depending on the dimensionless Gauss width γ for different contact interaction strengths P. Additionally, we also include the minimum of each curve depicted by a red dot as well as an interpolation indicated by the red dashed line. We clearly see that the minimum shifts to larger values of γ, as we increase the interaction strength P. These results coincide with those given in Ref. [100] and lead to the identical values of γ_0 shown in Fig. 3.1. From here on, we again set $P = 446$ for all later calculations.

Now we include the interaction caused by Newtonian gravity. Again, we already calculated the Lagrangian in spherical symmetry, see Eq. (3.84). When we replace the Gauss width A with the dimensionless Gauss width γ via the transformation Eq. (2.33) we get for the effective potential

$$V_{\text{eff}}^{(\text{N})} = \frac{3}{2}\left(\gamma^2 + \frac{1}{\gamma^2}\right) + \frac{P}{\gamma^3} - \frac{3Q}{\gamma}, \tag{E.3}$$

which we also show in Fig. E.1 on the right side depending on the gravitational interaction strength Q defined in Eq. (3.46). Once more, this confirms the results of Sec. 3.2.3 as the minimal Gauss width γ_0 decreases with stronger attractive interaction. We also see that visible changes occur at around $Q \sim 10$ as mentioned in Sec. 3.2.3. Nevertheless, we stick with a realistic value of $Q = 4.1 \cdot 10^{-19}$ for the following calculations.

The next interaction is the Yukawa-like interaction discussed in Sec. 3.3. In spherical symmetry the Lagrangian was derived in Eq. (3.86). Replacing A by the dimensionless

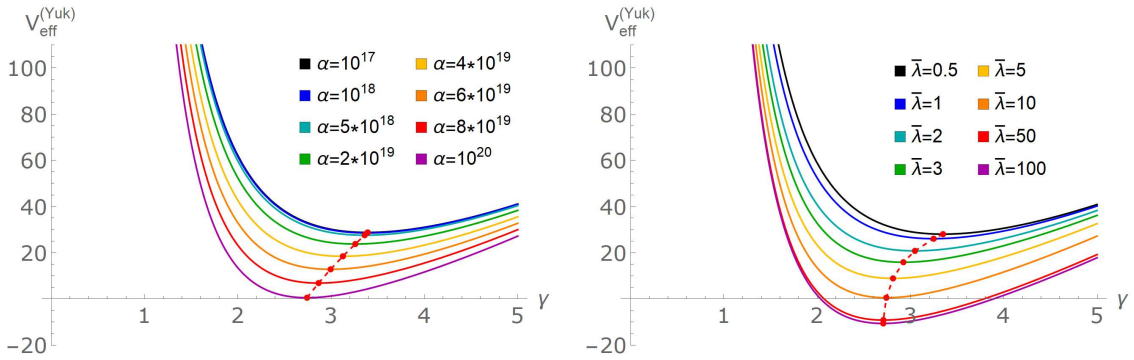

Figure E.2.: Effective potential for the Yukawa-like interaction depending on the strength α (left) and the dimensionless effective range $\bar{\lambda}$ (right). We set $P = 446$ and $Q = 4.1 \cdot 10^{-19}$. In the picture on the left side we choose $\bar{\lambda} = 10$ and on the right side $\alpha = 10^{20}$. The red dots indicate the minimum of each curve.

Gauss width γ yields the effective potential

$$V_{\text{eff}}^{(\text{Yuk})} = \frac{3}{2}\left(\gamma^2 + \frac{1}{\gamma^2}\right) + \frac{P}{\gamma^3} - 3Q\frac{1}{\gamma} - \alpha\, 3Q\left(\frac{1}{\gamma} - \sqrt{\frac{\pi}{2}}\frac{1}{\bar{\lambda}}\exp\left\{\frac{\gamma^2}{2\bar{\lambda}^2}\right\}\operatorname{erfc}\left[\sqrt{\frac{\gamma^2}{2\bar{\lambda}^2}}\right]\right). \tag{E.4}$$

We now have two parameters, namely the interaction strength α and the dimensionless effective range $\bar{\lambda}$. Therefore, we vary one, while setting the other fixed. For the fixed values we choose $\alpha = 10^{20}$ and $\bar{\lambda} = 10$, which corresponds for a ^{87}Rb condensate to a length $\lambda \approx 8.5\ \mu$m according to (2.33).

The results are shown in Fig. E.2. In the left picture we present the effective potential for different values of α. We see a similar behavior as in Fig. E.1 on the right side as both Q and α appear as a simple prefactor in the effective potential. If we increase α the attractive interaction is larger, thus the cloud width decreases as indicated by the colored curves. Furthermore, the minimum of each curve marked by the red dots moves to lower values of γ. On the right side of Fig. E.2 the dependency of $\bar{\lambda}$ is more interesting because the minimum of the potential seems to converge to a constant value for γ. This occurs at an effective range of roughly $\lambda \approx 10\ \mu$m, which coincides with the observation in the contour plot in Fig. 3.5. There the curves flatten for ranges larger than $\lambda \approx 10\ \mu$m.

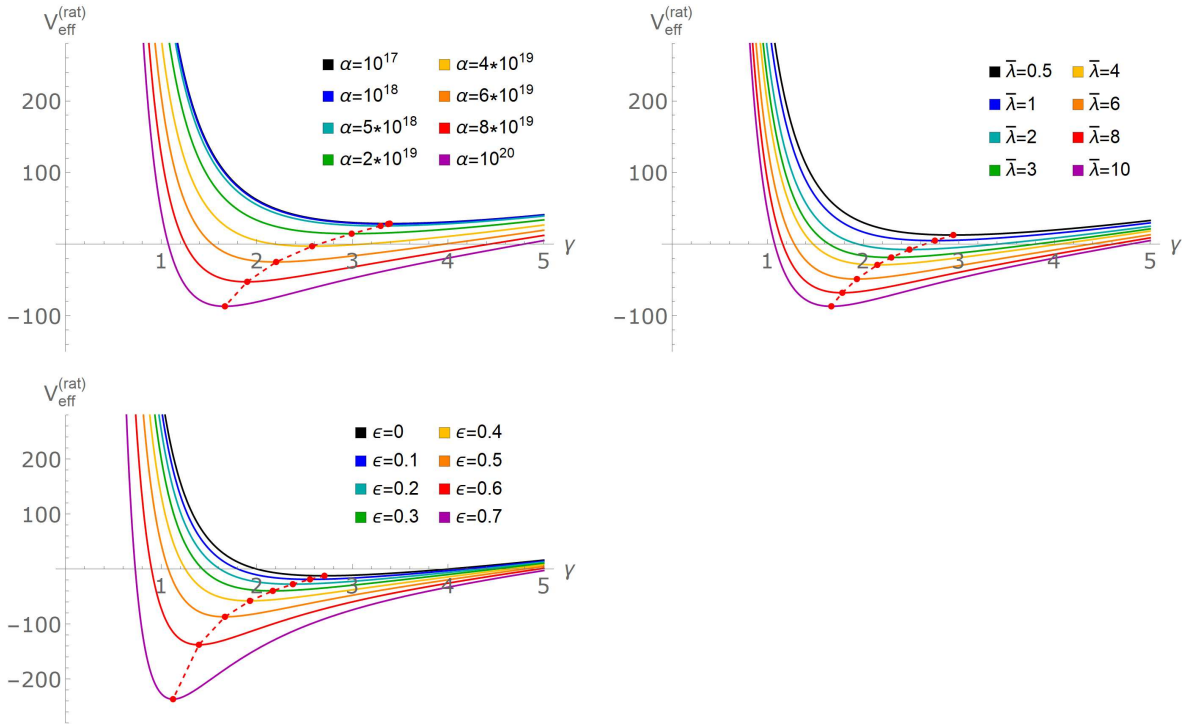

Figure E.3.: Effective potential for an interaction via the rational potential given in Eq. (5.3) depending on the interaction strength α (top left), the dimensionless parameter $\bar{\lambda}$ (top right) and the exponent ϵ (bottom). We set $P = 446$ and $Q = 4.1 \cdot 10^{-19}$ and if a parameter is not varied we set $\alpha = 10^{20}$, $\bar{\lambda} = 10$ and $\epsilon = 0.5$. The red dots indicate the minimum of each curve.

Finally, we discuss the effective potential for an interaction given by the rational potential. Up to now we have not calculated the Lagrangian in spherical symmetry, so we explain that here. The general form of the Lagrangian is given in Eq. (5.14). Furthermore, we defined the integral I_{rat} in Eq. (5.15). In spherical coordinates the integrals were already solved in Appendix D for $\epsilon > -1$. With the prefactors of I_{rat} and the Lagrangian in (5.14) we easily determine the effective potential

$$V_{\text{eff}}^{(\text{rat})} = \frac{3}{2}\left(\gamma^2 + \frac{1}{\gamma^2}\right) + \frac{P}{\gamma^3} - \frac{3Q}{\gamma} - \alpha\frac{3Q}{\sqrt{\pi}}\bar{\lambda}^{\epsilon}\sqrt{2^{\epsilon}}\cos\left(\frac{\pi}{2}\epsilon\right)\Gamma(1-\epsilon)\,\Gamma\left(\frac{1+\epsilon}{2}\right)\frac{1}{\gamma^{1+\epsilon}}. \tag{E.5}$$

The effective potential for an interaction described by a rational potential is shown in Fig. E.3 depending on the interaction strength α, the dimensionless parameter $\bar{\lambda}$ and

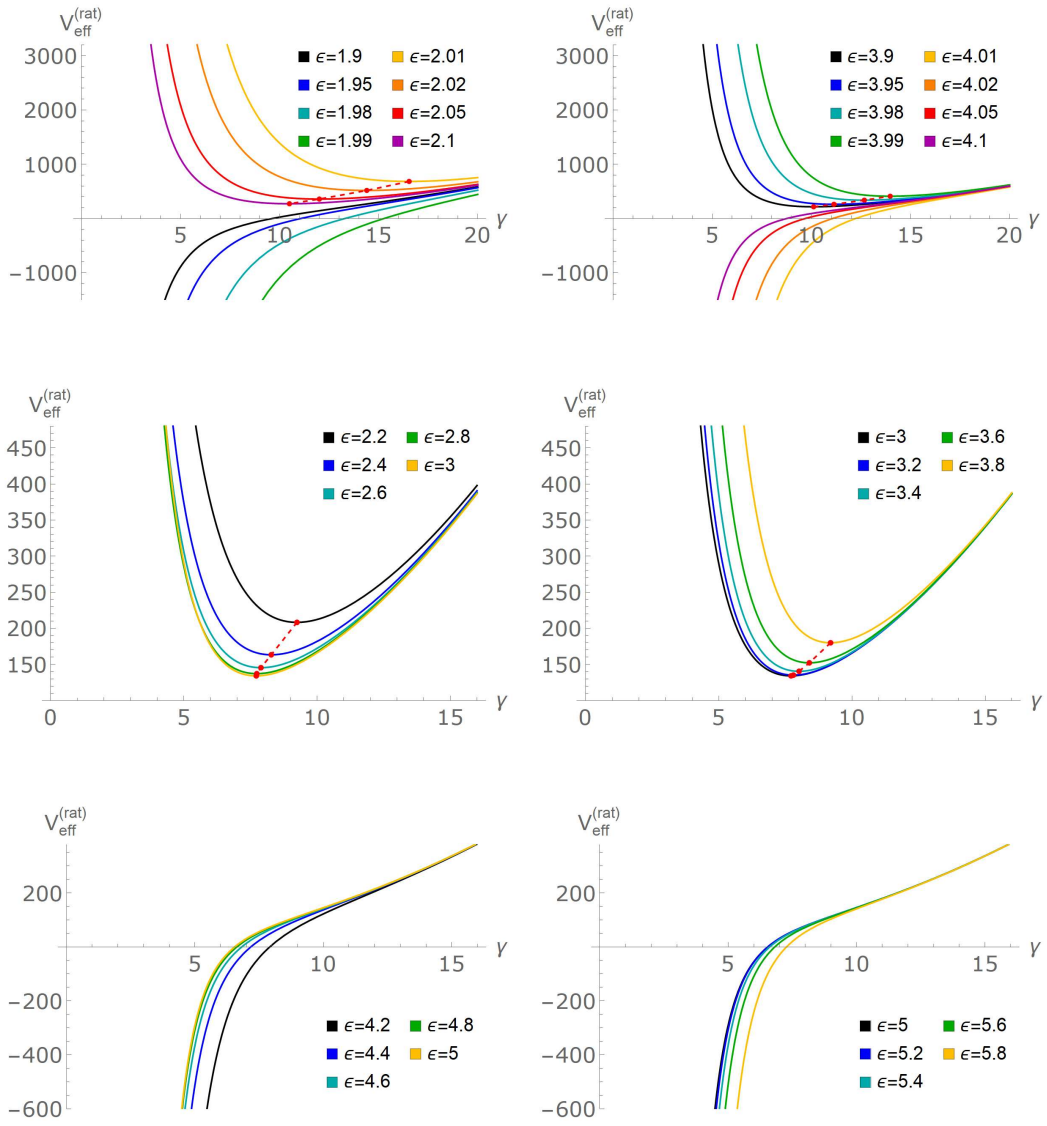

Figure E.4.: Effective potential for an interaction via the rational potential given in Eq. (5.3) depending on the exponent ϵ with $P = 446$, $Q = 4.1 \cdot 10^{-19}$, $\alpha = 10^{20}$ and $\bar{\lambda} = 10$. We show $V_{\text{eff}}^{(\text{rat})}$ near the divergences $\epsilon = 2$ (top left) and $\epsilon = 4$ (top right) as well as approaching the turning point $\epsilon = 3$ from below (bottom left) and from above (bottom right). The red dots indicate the minimum of each curve.

the parameter ϵ. The influence of α is exactly as expected as it fulfills the same role for the Yukawa-like interaction as seen in Fig. E.2. The dependency on $\bar{\lambda}$, however, differs. Here, the minimum of the curve does not converge for smaller values of $\bar{\lambda}$. Note that we mentioned in Sec. 5.1 that $\bar{\lambda}$ in case of the modified potential is not an effective range, so it does not correspond to the effective range in the Yukawa potential. If we look closer into the formulas, for example (E.5), $\bar{\lambda}^\epsilon$ is just a prefactor similar to α and Q. So it is not surprising that all three have basically the same effect.

The more interesting parameter is of course the exponent ϵ. For small values of ϵ the minimum of the effective potential moves to smaller values of γ as seen in Fig. E.3. But as we know from Fig. 5.3, there are singular points at even integers of ϵ. The vicinity of two of them are shown in Fig. E.4, namely $\epsilon = 2$ and $\epsilon = 4$. Approaching $\epsilon = 2$ from below the potential decreases. On the other side, approaching the same value of ϵ from above the potential increases as well as the minima. Consequently, both limits do not coincide. For $\epsilon = 4$ this effect is inverted. Both observations, however, look similar to the schematic plot of the Fourier transformed rational potential in Fig. 5.3 at the corresponding values of ϵ.

The other pictures in Fig. E.4 show the effective potential at the vicinity of $\epsilon = 3$ and $\epsilon = 5$. Based on the colors of each curve we see that the potential decreases while approaching $\epsilon = 3$ and increases for $\epsilon > 3$. In the other case the potential becomes narrower while approaching $\epsilon = 5$ and wider for $\epsilon > 5$. Furthermore, for both figures showing $\epsilon \approx 3$ we added the minima, which usually correspond to the equilibrium cloud width and therefore the rough size of the condensate. This implies that the size of a condensate is locally the smallest for $\epsilon = 3$, but larger for example in both cases $\epsilon = 2.6$ and $\epsilon = 3.4$. Additionally, the absolute values of the minima γ_0 in these cases are roughly one order of magnitude larger than in Fig E.3 for $\epsilon = 0$ to $\epsilon = 0.7$. This would suggest that a condensate in that case is ten times larger for $\epsilon \approx 3$ than for $\epsilon < 0.7$.

Although these observations are quite unusual from a physical point of view, it matches Fig. 5.3 and at least partially explain the results found in Fig. 5.7.

List of Acronyms

BEC	Bose-Einstein condensate
GPE	Gross-Pitaevskii equation
GR	General Relativity
GPN	Gross-Pitaevskii-Newton
ODE	ordinary differential equation

List of Figures

List of Tables

Bibliography

[1] S. Bose. Plancks Gesetz und Lichtquantenhypothese. *Zeitschrift für Physik*, **26**, 178, 1924.

[2] A. Einstein. Quantentheorie des einatomigen idealen Gases, 1925. Handwritten manuscript, Leiden University, Instituut-Lorentz.

[3] S. Chu. The manipulation of neutral particles. *Review of Modern Physics*, **70**, 685, 1998.

[4] C. N. Cohen-Tannoudji. Manipulating atoms with photons. *Review of Modern Physics*, **70**, 707, 1998.

[5] W. D. Phillips. Laser cooling and trapping of neutral atoms. *Review of Modern Physics*, **70**, 721, 1998.

[6] M. H. Anderson, J. R. Ensher, M. R. Matthews, C. E. Wieman, and E. A. Cornell. Observation of Bose-Einstein Condensation in a Dilute Atomic Vapor. *Science*, **269**, 5221, 1995.

[7] K. B. Davis, M.-O. Mewes, M. R. Andrews, N. J. van Druten, D. S. Durfee, D. M. Kurn, and W. Ketterle. Bose-Einstein Condensation in a Gas of Sodium Atoms. *Physical Review Letters*, **75**, 3969, 1995.

[8] C. C. Bradley, C. A. Sackett, J. J. Tollett, and R. G. Hulet. Evidence of Bose-Einstein Condensation in an Atomic Gas with Attractive Interactions. *Physical Review Letters*, **75**, 1687, 1995.

[9] C. C. Bradley, C. A. Sackett, J. J. Tollett, and R. G. Hulet. Errata - Evidence of Bose-Einstein Condensation in an Atomic Gas with Attractive Interactions. *Physical Review Letters*, **79**, 1170, 1997.

[10] D. G. Fried, T. C. Killian, L. Willmann, D. Landhuis, S. C. Moss, D. Kleppner, and T. J. Greytak. Bose-Einstein Condensation of Atomic Hydrogen. *Physical Review Letters*, **81**, 3811, 1998.

[11] F. P. Dos Santos, J. Léonard, J. Wang, C. J. Barrelet, F. Perales, E. Rasel, C. S. Unnikrishnan, M. Leduc, and C. Cohen-Tannoudji. Bose-Einstein Condensation of Metastable Helium. *Physical Review Letters*, **86**, 3459, 2001.

[12] S. Kraft, F. Vogt, O. Appel, F. Riehle, and U. Sterr. Bose-Einstein Condensation of Alkaline Earth Atoms: ^{40}Ca. *Physical Review Letters*, **103**, 130401, 2009.

[13] G. Modugno, G. Ferrari, G. Roati, R. J. Brecha, A. Simoni, and M. Inguscio. Bose-Einstein Condensation of Potassium Atoms by Sympathetic Cooling. *Science*, **294**, 5545, 2001.

[14] S. Stellmer, M. K. Tey, B. Huang, R. Grimm, and F. Schreck. Bose-Einstein Condensation fo Strontium. *Physical Review Letters*, **103**, 200401, 2009.

[15] Y. N. Martinez de Escobar, P. G. Mickelson, M. Yan, B. J. DeSalvo, S. B. Nagel, and T. C. Killian. Bose-Einstein Condensation of ^{84}Sr. *Physical Review Letters*, **103**, 2000402, 2009.

[16] T. Weber, J. Herbig, M. Mark, H. Nägerl, and R. Grimm. Bose-Einstein Condensation of Cesium. *Science*, **299**, 5604, 2002.

[17] Y. Takasu, K. Maki, K. Komori, T. Takanio, K. Honda, M. Kumakura, T. Yabuzaki, and Y. Takahashi. Spin-Singlet Bose-Einstein Condensation of Two-Electron Atoms. *Physical Review Letters*, **91**, 040404, 2003.

[18] A. Griesmaier, J. Werner, S. Hensler, J. Stuhler, and T. Pfau. Bose-Einstein Condensation of Chromium. *Physical Review Letters*, **94**, 160401, 2005.

[19] M. Lu, N. Q. Burdick, S. H. Youn, and B. Lev. Strongly Dipolar Bose-Einstein Condensate of Dysprosium. *Physical Review Letters*, **107**, 190401, 2011.

[20] K. Aikawa, A. Frisch, M. Mark, S. Baier, A. Rietzler, R. Grimm, and F. Ferlaino. Bose-Einstein Condensation of Erbium. *Physical Review Letters*, **108**, 210401, 2012.

[21] E. T. Davletov, V. V. Tsyganok, V. A. Khlebnikov, D. A. Pershin, D. V. Shaykin, and A. V. Akimov. Machine learning for achieving Bose-Einstein condensation of thulium atoms. *Physical Review A*, **102**, 011302, 2020.

[22] Y. Miyazawa, R. Inoue, H. Matsui, G, Nomura, and M. Kozuma. Bose-Einstein Condensation of Europium. *Physical Review Letters*, **129**, 223401, 2022.

[23] D. S. Petrov, C. Salomon, and G. V. Shlyapnikov. Weakly Bound Dimers of Fermionic Atoms. *Physical Review Letters*, **93**, 090404, 2004.

[24] M. W. Zwierlein, J. R. Abo-Shaeer, A. Schirotzek, C. H. Schunk, and W. Ketterle. Vortices and superfluidity in a strongly interacting Fermi gas. *Nature*, **435**, 1047-1051, 2005.

[25] G. Modugno, M. Modugno, F. Riboli, G. Roati, and M. Inguscio. Two Atomic Species Superfluid. *Physical Review Letters*, **89**, 190404, 2002.

[26] I. Ferrier-Barbut, M. Delehaye, S. Laurent, A.T. Grier, M. Pierce, B. S. Rem, F. Chevy, and C. Salomon. A mixture of Bose and Fermi superfluids. *Science*, **345**, 6200, 2014.

[27] J. Klaers, J. Schmitt, F. Vewinger, and M. Weitz. Bose-Einstein condensation of photons in an optical microcavity. *Nature*, **468**, 545-548, 2010.

[28] O. V. Misochko, M. Hase, K. Ishioka, and M. Kitajima. Transient Bose-Einstein condensation of phonons. *Physical Letters A*, **321**, 5-6, 2004.

[29] S. O. Demokritov, V. E. Demidov, O. Dzyapko, G. A. Melkov, A. A. Serga, B. Hillebrands, and A. N. Slavin. Bose-Einstein condensation of quasi-equilibrium magnons at room temperature under pumping. *Nature*, **443**, 430-433, 2006.

[30] H. Deng, H. Haug, and Y. Yamamoto. Exciton-polariton Bose-Einstein condensation. *Review of Modern Physics*, **82**, 1489, 2010.

[31] S. Giorgini, L. P. Pitaevskii, and S. Stringari. Theory of ultracold atomic Fermi gases. *Review of Modern Physics*, **80**, 1215, 2008.

[32] C. Chin, R. Grimm, P. Julienne, and E. Tiesinga. Feshbach resonances in ultracold gases. *Review of Modern Physics*, **82**, 1225, 2010.

[33] D. Becker, M. D. Lachmann, S. T. Seidel, H. Ahlers, A. N. Dinkelaker, J. Grosse, O. Hellmig, H. Müntinga, V. Schkolnik, T. Wendrich, A. Wenzlawski, B. Weps, R. Corgier, T. Franz, N. Gaaloul, W. Herr, D. Lüdtke, M. Popp, S. Amri, H. Duncker, M. Erbe, A. Kohfeldt, A. Kubelka-Lange, C. Braxmaier, E. Charron, W. Ertmer, M. Krutzik, C. Lämmerzahl, A. Peters, W. P. Schleich, K. Sengstock, R. Walser, A. Wicht, P. Windpassinger, and E. M. Rasel. Space-borne Bose-Einstein condensation for precision interferometry. *Nature*, **562**, 391-395, 2018.

[34] C. Deppner, W. Herr, M. Cornelius, P. Stromberger, T. Sternke, C. Grzeschik, A. Grote, J. Rudolph, S. Herrmann, M. Krutzik, A. Wenzlawski, R. Corgier, E. Charron, D. Guéry-Odelin, N. Gaaloul, C. Lämmerzahl, A. Peters, P. Windpassinger, and E. Rasel. Collective-Mode Enhanced Matter-Wave Optics. *Physical Review Letters*, **127**, 100401, 2021.

[35] D. C. Aveline, J. R. Williams, E. R. Elliott, C. Dutenhoffer, J. R. Kellogg, J. M. Kohel, N. E. Lay, K. Oudrhiri, R. F. Shotwell, N. Yu, and R. J. Thompson. Observation of Bose-Einstein condensates in an Earth-orbiting research lab. *Nature*, **582**, 193-197, 2020.

[36] D. Jaksch, C. Bruder, J. I. Cirac, C. W. Gardiner, and P. Zoller. Cold bosonic atoms in optical lattices. *Physical Review Letters*, **81**, 3108, 1998.

[37] M. Greiner, O. Mandel, T. Esslinger, T. W. Hänsch, and I. Bloch. Quantum phase transition from a superfluid to a Mott insulator in a gas of ultracold atoms. *Nature*, **415**, 39, 2002.

[38] C. J. Pethick and H. Smith. *Bose-Einstein Condensation in Dilute Gases*. Cambridge University Press, New York, 1. edition, 2002.

[39] O. Lahav, A. Itah, A. Blumkin, C. Gordon, S. Rinott, A. Zayats, and J. Steinhauer. Realization of a Sonic Black Hole Analog in a Bose-Einstein Condensate. *Physical Review Letters*, **105**, 240401, 2010.

[40] F. Dalfovo, S. Giorgini, L. P. Pitaevskii, and S. Stringari. Theory of Bose-Einstein condensation in trapped gases. *Review of Modern Physics*, **71**, 463, 1999.

[41] J. R. Abo-Shaeer, C. Raman, and W. Ketterle. Formation and Decay of Vortex Lattices in Bose-Einstein Condensates at Finite Temperatures. *Physical Review Letters*, **88**, 070409, 2002.

[42] D. O'Dell, S. Giovanazzi, G. Kurizki, and V. M. Akulin. Bose-Einstein Condensates with 1/r Interatomic Attraction: Electromagnetically Induced "Gravity". *Physical Review Letters*, **84**, 5687, 2000.

[43] J. Anglin. Theoretical physics: Why trapped atoms are attractive. *Nature*, **406**, 29, 2000.

[44] Collective Excitations (BEC@MIT). `https://www.rle.mit.edu/cua_pub/ketterle_group/Projects_1998/Coll_exc/Collective_excitations.htm`. Accessed: 2022-12-14.

[45] D. S. Jin, J. R. Ensher, M. R. Matthews, C. E. Wieman, and E. A. Cornell. Collective Excitations of a Bose-Einstein Condensate in a Dilute Gas. *Physical Review Letters*, **77**, 420, 1996.

[46] D. M. Stamper-Kurn, H.-J. Miesner, S. Inouye, M. R. Andrews, and W. Ketterle. Collisionless and Hydrodynamic Excitations of a Bose-Einstein Condensate. *Physical Review Letters*, **81**, 500, 1998.

[47] L. You, W. Hoston, and M. Lewenstein. Low-lying excitations of a trapped Bose condensate. *Physical Review A*, **55**, 3, 1997.

[48] S. Giovanazzi, L. Santor, and T. Pfau. Collective oscillations of dipolar Bose-Einstein condensates and accurate comparison between contact and dipolar interactions. *Physical Review A*, **75**, 015604, 2007.

[49] A. Altmeyer, S. Riedl, C.Kohstall, M. J. Wright, R. Geursen, M. Bartenstein, C. Chin, J. Hecker Denschlag, and R. Grimm. Precision Measurements of Collective Oscillations in the BEC-BCS Crossover. *Physical Review Letters*, **98**, 040401, 2007.

[50] S. E. Pollack, D. Dries, M. Junker, Y. P. Chen, T. A. Corcovilos, and R. G. Hulet. Extreme Tunability of Interactions in a ^{7}Li Bose-Einstein Condensate. *Physical Review Letters*, **102**, 090402, 2009.

[51] I. Newton. Newton's Principia. The mathematical principles of natural philosophy, 1642-1727. Accessed: 2023-03-30.

[52] CODATA Value: Newtonian constant of gravitation. `https://physics.nist.gov/cgi-bin/cuu/Value?bg`. Accessed: 2022-12-10.

[53] C. M. Will. General Relativity at 75: How Right Was Einstein? *Science*, **250**, 4982, 1990.

[54] B. P. Abbott *et al.* (LIGO Scientific Collaboration and Virgo Collaboration). Observation of Gravitational Waves from a Binary Black Hole Merger. *Physical Review Letters*, **116**, 061102, 2016.

[55] D. Castelvecchi. Black hole imaged for first time. *Nature*, **284**, 568, 2019.

[56] S. Carlip. Is quantum gravity necessary? *Classical and Quantum Gravity*, **25**, 154010, 2008.

[57] Y. Fujii. Dilaton and Possible Non-Newtonian Gravity. *Nature*, **234**, 5-7, 1971.

[58] D. R. Long. Experimental examination of the gravitational inverse square law. *Nature*, **260**, 417-418, 1976.

[59] E. Fischbach, D. Sudarsky, A. Szafar. C. Talmadge, and S. H. Aronson. Reanalysis of the Eötvös experiment. *Physical Review Letters*, **56**, 3, 1986.

[60] E. Fischbach, D. Sudarsky, A. Szafar. C. Talmadge, and S. H. Aronson. Reanalysis of the Eötvös experiment. *Physical Review Letters*, **56**, 1427, 1986.

[61] H. H. Thodberg. Comment on the Sign in the Reanalysis of the Eötvös Experiment. *Physical Review Letters*, **56**, 2423, 1986.

[62] E. Fischbach, D. Sudarsky, A. Szafar. C. Talmadge, and S. H. Aronson. Fischbach *et al.* Respond. *Physical Review Letters*, **56**, 2424, 1986.

[63] H. H. Thodberg. ERRATA: Comment on the Sign in the Reanalysis of the Eötvös Experiment. *Physical Review Letters*, **57**, 1192, 1986.

[64] N. Arkani-Hamed, S. Dimopoulos, and G. Dvali. The hierarchy problem and new dimensions at a millimeter. *Physics Letters B*, **429**, 263-272, 1998.

[65] N. Arkani-Hamed, S. Dimopoulos, and G. Dvali. Phenomenology, astrophyics, and cosmology of theories with submillimeter dimensions and TeV scale quantum gravity. *Physical Review D*, **59**, 086004, 1999.

[66] E. G. Adelberger, B. R. Heckel, and A. E. Nelson. Tests of the Gravitational Inverse-Square Law. *Annual Review of Nuclear and Particle Science*, **53**, 77-121, 2003.

[67] D. J. Kapner, T. S. Cook, E. G. Adelberger, J. H. Gundlach, B. R. Heckel, C. D. Hoyle, and H. E. Swanson. Tests of the Gravitational Inverse-Square Law below the Dark-Energy Length Scale. *Physical Review Letters*, **98**, 021101, 2007.

[68] S. J. Smullin, A. A. Geraci, D. M. Weld, J. Chiaverini, S. Holmes, and A. Kapitulnik. Constraints on Yukawa-type deviations from Newtonian gravity at 20 microns. *Physical Review D*, **72**, 122001, 2005.

[69] J. Murata and S. Tanaki. A review of short-range gravity experiments in the LHC era. *Classical and Quantum Gravity*, **32**, 033001, 2015.

[70] E. Fischbach and C. L. Talmadge. *The Search for Non-Newtonian Gravity.* Springer, 1. edition, 1999.

[71] K. Schmitz. Experimental Tests of the Gravity Sector, DESY Werkstattseminar "Physics of Extra Dimensions", 2011. Accessed: 2021-04-20.

[72] T. Aaltonen *et al.* (CDF Collaboration). Search for Large Extra Dimensions in Final States Containing One Photon or Jet and Large Missing Transverse Energy Produced in $p\bar{p}$ Collisions at $\sqrt{s} = 1.96$ TeV. *Physical Review Letters*, **101**, 181602, 2008.

[73] G. Aad *et al.* (ATLAS Collaboration). Search for new phenomena with the monojet and missing transverse momentum signature using the ATLAS detector in $\sqrt{s} =$ 7 TeV proton-proton collisions. *Physics Letters B*, **705**, 4, 2011.

[74] G. Aad *et al.* (ATLAS Collaboration). Search for Dark Matter Candidates and Large Extra Dimensions in Events with a Photon and Missing Transverse Momentum in $\sqrt{s} = 7$ TeV with the ATLAS Detector. *Physical Review Letters*, **110**, 011802, 2013.

[75] L. Iorio. Constraints on the range λ of Yukawa-like modifications to the Newtonian inverse-square law of gravitation from Solar System planetary motions. *Journal of High Energy Physics*, JHEP10(2007)041, 2007.

[76] E. G. Adelberger, J. H. Gundlach, B. R. Heckel, S. Hoedl, and S. Schlamminger. Torsion balance experiments: A low-energy frontier of particle physics. *Progress in Particle and Nuclear Physics*, **62**, 102-134, 2009.

[77] J. Chiaverini, S. J. Smullin, A. A. Geraci, D. M. Weld, and A. Kapitulnik. New Experimental Constraints on Non-Newtonian Forces below 100 μm. *Physical Review Letters*, **90**, 151101, 2003.

[78] S. K. Lamoreaux. Demonstration of the Casimir Force in the 0.6 to 6 μm Range. *Physical Review Letters*, **78**, 5, 1997.

[79] S. K. Lamoreaux. Erratum: Demonstration of the Casimir Force in the 0.6 to 6 μm Range [Phys. Rev. Lett. 78, 5 (1997)]. *Physical Review Letters*, **81**, 5475, 1998.

[80] B. W. Harris, F. Chen, and U. Mohideen. Precision measurement of the Casimir force using gold surfaces. *Physical Review A*, **62**, 052109, 2000.

[81] J. Bergé, P. Brax, M. Pernot-Borràs, and J.-P. Uzan. Interpretation of geodesy experiments in non-Newtonian theories of gravity. *Classical and Quantum Gravity*, **35**, 234001, 2018.

[82] S.-H. Yang, C.-M. Pi, X.-P. Zheng, and F. Weber. Non-Newtonian Gravity in Strange Quark Stars and Constraints from the Observations of PSR J0740+6620 and GW170817. *The Astrophysical Journal*, **902**, 32, 2020.

[83] C. C. Haddock, N. Oi, K. Hirota, T. Ino, M. Kitaguchi, S. Matsumoto, K. Mishima, T. Shima, H. M. Shimizu, W. M. Snow, and T. Yoshioka. Search for deviations from the inverse square law of gravity at nm range using a pulsed neutron beam. *Physical Review D*, **97**, 062002, 2018.

[84] J. M. Rocha and F. Dahia. Neutron interferometry and tests of short-range modifications of gravity. *Physical Review D*, **103**, 124014, 2021.

[85] S. Qvarfort, D. Rätzel, and S. Stopyra. Constraining modified gravity with quantum optomechanics. *New Journal of Physics*, **24**, 033009, 2022.

[86] J. Bergé, P. Brax, G. Métris, M. Pernot-Borràs, P. Touboul, and J.-P. Uzan. MICROSCOPE Mission: First Constraints on the Violation of the Weak Equivalence Principle by a Light Scalar Dilaton. *Physical Review Letters*, **120**, 141101, 2018.

[87] R. Ruffini and S. Bonazzola. Systems of Self-Gravitating Particles in General Relativity and the Concept of an Equation of State. *Physical Review Journals Archive*, **187**, 1767, 1969.

[88] M. Colpi, S. L. Stuart, and I. Wasserman. Boson Stars: Gravitational Equilibria of Self-Interacting Scalar Fields. *Physical Review Letters*, **57**, 2485, 1986.

[89] C. G. Böhmer and T. Harko. Can dark matter be a Bose-Einstein condensate? *Journal of Cosmology and Astroparticle Physics*, JCAP06(2007)025, 2007.

[90] R. Penrose. On Gravity's role in Quantum State Reduction. *General Relativity and Gravitation*, **28**, 581-600, 1996.

[91] D. Giulini and A. Großardt. The Schrödinger-Newton equation as a non-relativistic limit of self-gravitating Klein-Gordon and Dirac fields. *Classical and Quantum Gravity*, **29**, 215010, 2012.

[92] D. Giulini and A. Großardt. Centre-of-mass motion in multi-particle Schrödinger-Newton dynamics. *New Journal of Physics*, **16**, 075005, 2014.

[93] P.-H. Chavanis. Collapse of a self-gravitating Bose-Einstein condensate with attractive self-interaction. *Physical Review D*, **70**, 721, 2016.

[94] W. Bao, N. B. Abdallah, and Y. Cai. Gross-Pitaevskii-Poisson Equations for Dipolar Bose-Einstein Condensate with Anisotropic Confinement. *SIAM Journal on Mathematical Analysis*, **44**, 3, 2012.

[95] H. Sakaguchi and B. A. Malomed. Gross-Pitaevskii-Poisson model for an ultracold plasma: Density waves and solitons. *Physical Review Research*, **2**, 033188, 2020.

[96] K. Schroven, M. List, and C. Lämmerzahl. Stability of self-gravitating Bose-Einstein condensates. *Physical Review D*, **92**, 124008, 2015.

[97] V. T. Toth. Self-Gravitating Bose-Einstein Condensates and the Thomas-Fermi Approximation. *Galaxies*, **4**(3), 9, 2016.

[98] E. J. M. Madarassy and V. T. Toth. Numerical simulation code for self-gravitating Bose-Einstein condensates. *Computer Physics Communications*, **184**, 4, 1339-1343, 2013.

[99] V. M. Pérez-Garcia, H. Michinel, J. I. Cirac, M. Lewenstein, and P. Zoller. Low Energy Excitations of a Bose-Einstein Condensate: A Time-Dependent Variational Analysis. *Physical Review Letters*, **77**, 5320, 1996.

[100] V. M. Pérez-Garcia, H. Michinel, J. I. Cirac, M. Lewenstein, and P. Zoller. Dynamics of Bose-Einstein condensates: Variational solutions of the Gross-Pitaevskii equations. *Physical Review A*, **56**, 1424, 1997.

[101] A. Pelster. Bose-Einstein Kondensation (in German), lecture in summer term 2004, 2004. Accessed: 2020-10-16.

[102] H. J. H. Al-Jibbouri. Collective Excitations in Bose-Einstein Condensates. PhD Thesis, Freie Universität Berlin, 2013.

[103] W. Kohn. Cyclotron Resonance and de Haas-van Alphen Oscillations of an Interacting Electron Gas. *Physical Review Journals Archive*, **123**, 1242, 1961.

[104] J. F. Dobson. Harmonic-Potential Theorem: Implications for Approximate Many-Body Theories. *Physical Review Letters*, **73**, 2244, 1994.

[105] A. L. Fetter and D. Rokhsar. Excited states of a dilute Bose-Einstein condensate in a harmonic trap. *Physical Review A*, **57**, 1191, 1998.

[106] H. Al-Jibbouri and A. Pelster. Breakdown of the Kohn theorem near a Feshbach resonance in a magnetic trap. *Physical Review A*, **88**, 033621, 2013.

[107] E. Stein, F. Vewinger, and A. Pelster. Collective modes of a photon Bose-Einstein condensate with thermo-optic interaction. *New Journal of Physics*, **21**, 103044, 2019.

[108] I. M. Ryzhik and I. S. Gradsteyn. *Table of Integrals, Series, and Products*. Elsevier Inc., 7. edition, 2007.

[109] D. R. Curtiss. Recent Extentions of Descartes' Rule of Signs. *Annals of Mathematics*, **19**, 4, 1918.

[110] S. Stringari. Collective Excitations of a Trapped Bose-Condensed Gas. *Physical Review Letters*, **77**, 2360, 1996.

[111] M. Schütte. Bose-Einstein Condensates with Long-Range Interactions. Diploma thesis, Freie Universität Berlin, 2007.

[112] P. Muruganandam and S. K. Adhikari. Numerical and variational solutions of the dipolar Gross-Pitaevskii equation in reduced dimensions. *Laser Physics*, **22**, 813-820, 2012.

[113] M. Kitagawa, K. Enomoto, K. Kasa, Y. Takahashi, R. Ciuryło, P. Naidon, and P. S. Julienne. Two-color photoassociation spectroscopy of ytterbium atoms and the precise determinations of s-wave scattering lengths. *Physical Review A*, **77**, 012719, 2008.

[114] L. Salasnich, A. Parola, and L. Reatto. Effective wave equations for the dynamics of cigar-shaped and disk-shaped Bose condensates. *Physical Review A*, **65**, 043614, 2002.

[115] D. S. Petrov, D. M. Gangardt, and G. V. Shlyapnikov. Low-dimensional trapped gases. *Journal de Physique IV France*, **116**, 5-44, 2004.

[116] M. Olshanii. Atomic Scattering in the Presence of an External Confinement and a Gas of Impenetrable Bosons. *Physical Review Letters*, **81**, 938, 1998.

[117] J. K. Langley. Transcendental Singularities for a Meromorphic Function with Logarithmic Derivative of Finite Lower Order. *Computational Methods and Function Theory*, **19**, 117-133, 2019.

[118] A. Eremenko. Singularities of inverse functions. *arXiv*, arXiv:2110.06134, 2021.

[119] E. Fischbach, D. E. Krause, V. M. Mostepanenko, and M. Novello. New constraints on ultrashort-ranged Yukawa interactions from atomic force microscopy. *Physical Review D*, **64**, 075010, 2001.

[120] I. M. Gel'fand and G. E. Shilov. *Generalized Functions, Volume 1: Properties and Operations*. Academic Press, New York and London, 1964.

[121] L. Grafakos. *Classical Fourier Analysis*. Springer, New York, Heidelber, Dordrecht, London, 3. edition, 2010.

[122] Encyclopedia of Mathematics. `https://encyclopediaofmath.org/index.php?title=Riesz_potential`. Accessed: 2023-03-06.

[123] S. Sabari, R. V. J. Raja, K. Porsezian, and P. Muruganandam. Stability of trapless Bose-Einstein condensates with two- and three-body interactions. *Journal of Physics B: Atomic, Molecular and Optical Physics*, **43**, 125302, 2010.

[124] P. Ping and L. Guan-Qaing. Effects of three-body interaction on collective excitation and stability of Bose-Einstein condensate. *Chinese Physics B*, **18**, 3221, 2009.

[125] A. L. Fetter and A. A. Svidzinsky. Vortices in a trapped dilute Bose-Einstein condensate. *Journal of Physics: Condensed Matter*, **13**, R135-R194, 2001.

[126] D. Guéry-Odelin and S. Stringari. Scissors Mode and Superfluidity of a Trapped Bose-Einstein Condensed Gas. *Physical Review Letters*, **83**, 4452, 1999.

[127] O. M. Maragò, S. A. Hopkins, J. Arlt, E. Hodby, G. Hechenblaikner, and C. J. Foot. Observation of the Scissors Mode and Evidence for Superfluidity of a Trapped Bose-Einstein Condensed Gas. *Physical Review Letters*, **84**, 2056, 2000.

[128] A. Joyce, B. Jain, J. Khoury, and M. Trodden. Beyond the cosmological standard model. *Physics Reports*, **568**, 1, 2015.

[129] J. Khoury and A. Weltman. Chameleon Fields: Awaiting Surprises for Tests of Gravity in Space. *Physical Review Letters*, **93**, 171104, 2004.

[130] P. Hamilton, M. Jaffe, P. Haslinger, Q. Simmons, H. Müller, and J. Khoury. Atom-interferometry constraints on dark energy. *Science*, **349**, 6250, 2015.

[131] H. Kleinert and V. Schulte-Frohlinde. *Critical Properties of* Φ^4*-Theories*. World Scientific, 2001.

[132] L. C. Andrews. *Special Functions of Mathematics for Engineers*. SPIE Optical Engineering Press, Bellingham, Washington USA, 2. edition, 1998.

[133] M. Abramowitz and I. A. Stegun. *Handbook of Mathematical Functions With Formulas, Graphs, and Mathematical Tables.* National Bureau of Standards, Washington, D.C., 10. edition, 1972.

Acknowledgements

I would like to thank Prof. Dr. Claus Lämmerzahl for supervising my thesis over the last few years and for giving me the opportunity to work at the Drop Tower in Bremen. Despite his tight time schedule, we regularly exchanged information about my progress and future opportunities, and he always assisted me with minor and major problems during my research.

A special thanks goes to PD Dr. Axel Pelster for his continuous support and helpful discussions despite the spatial distance. His deep insights in the field of Ultracold Quantum Gases and his great advice as well as his experience were an important key in the development of this work. I also thank him for the numerous invitations to interesting conferences and finally for agreeing to be the second referee.

In addition, I would also like to give special thanks to Enrico Stein, Felix Willenborg, and Torben Frost. They have helped me with my research more times than I can possibly count, and I don't know how it all would have worked out without them. Thanks for all the long conversations about physics and even beyond.

Furthermore, I want to thank my current and former colleagues at ZARM and the Reasearch Training Group Models of Gravity, especially Roy Barzel, Dennis Stock, Dennis Philipp, Roberto Tanzi, Dennis Rätzel, Sven Hermann, Prof. Dr. Nico Giulini, and PD Dr. Volker Perlick for their support.

I also appreciate the financial support from the Collaborative Research Center DQ-mat and the Cluster of Excellence QuantumFrontiers.

Finally, my greatest thanks go to my family for the support they have given me throughout my life, and to all our pets for the very welcome distraction when work got too much.

Selbstständigkeitserklärung

Ich versichere, dass ich die Arbeit selbstständig verfasst und keine anderen als die angegebenen Hilfsmittel verwendet habe.

Sandro Gödtel